An Experimental Investigation of Richtmyer-Meshkov Instability

Thesis by

Sanjay Kumar

In Partial Fulfillment of the Requirements

for the Degree of

Doctor of Philosophy

California Institute of Technology

Pasadena, California

2003

(Submitted November 04, 2002)

Dedicated
to
the Memory of
my teacher

Prof. Bradford Sturtevant
1933-2000

Acknowledgements

With deepest gratitude I thank my advisors, the late Professor Bradford Sturtevant and Professor Hans G. Hornung, for advising and guiding me throughout the course of this study. They not only guided me through my quest for scientific knowledge, but also encouraged me to explore life itself. Prof. Sturtevant originally suggested this problem and gave me the opportunity to study at Caltech. I learned much from his enthusiasm toward science. I am forever indebted to him for all that he taught me. Prof. Hornung, always there to clear up any of my doubts, helped me through the difficulties at times when I was stuck. He is a very approachable professor having extraordinary enthusiasm for explaining things. This quality of his helped me clear up some of the conceptual problems of fluid mechanics in general. Special thanks also go to Prof. Joe Shepherd for giving new ideas and suggestions during the course of this study and thesis preparation.

On a more personal level, I would like to mention my parents, whose supportive role in my education and upbringing is beyond words. I would also like to thank all my friends here at Caltech who made life in the lab and on campus enjoyable.

This work was supported by the California Institute of Technology.

Abstract

In this study, the interaction of a shock wave with an interface between two gases is studied experimentally. The basic mechanism for the initial growth of perturbations on the interface is the baroclinic generation of vorticity which results from the misalignment of the pressure gradient in the shock and the density gradient at the interface. The growth of perturbations soon enters into a nonlinear regime with the appearance of bubbles of light fluid rising into heavy fluid and spikes of heavy fluid falling into light fluid. In the nonlinear regime, interaction between various scales and the appearance of other instabilities, such as Kelvin-Helmholtz instability, along the boundaries of the spikes occur, which results in the breakup of the interface. These processes lead to a turbulent mixing zone (TMZ) which grows with time. The main focus of this study is to understand the growth of TMZ with time in a cylindrical geometry with square cross section and for the the first time study the effect of area convergence in a conical geometry on its growth rate. The present set of experiments is done in the GALCIT 17 in. shock tube with air and SF_6 as light and heavy gases. The growth of the TMZ is studied in a straight test section for single-mode initial perturbation consisting of two different wavelength and amplitude combinations at incident shock Mach number of $M_S = 1.55$. The multimode initial perturbation growth at late times is studied in a conical geometry to study the effect of area convergence at incident Mach numbers of $M_S = 1.55$ and 1.39. The results are compared with the experiments of Vetter [74] which were done in the same shock tube with a straight test section with no area convergence and at the same Mach number.

In the study of the Richtmyer-Meshkov (RM) instability of single-scale perturbations on air/SF_6 interface in a straight test section, the initially sinusoidal interface is formed by a polymeric membrane of thickness 1.5 μm and the flow visualization is done using schlieren imaging technique. The interface thickness is measured visually

from the photographs. It is found that the growth rate decreases rapidly with time with a small dependence on the initial wavelength persisting until late times.

In the case of the RM instability, growth of multimode initial perturbations in a conical geometry, it is found from the schlieren flow visualization images that the interface thickness grows about 40-50% more rapidly than in Vetter's [74] experiments. Experimental results for laser-induced scattering at late times are presented for air/He gas combinations at the interface. In situations when the rear of the interface is not clearly demarcated, the thickness is determined by an image processing technique. This technique is also used to determine the possible dominant eddy/blob size in the TMZ from the schlieren images. Some inviscid computational studies, with a planar or spherical shock interacting with a planar or spherical initial interface in light-heavy (air/SF_6) and heavy-light (air/He) configurations, are also presented. In the conical geometry there is a reflected shock originating from the triple point. This reflection is a consequence of the transition from the cylindrical shock tube to the converging cone. Due to the vorticity created by the interaction of reflected shock from the cone wall with the interface in initial stage, it is found that the interface curves toward or away from the apex of the cone, depending on the sign of density gradient. This curving of the interface could have a role to play in the diffuse rear boundary of the interface in schlieren flow visualization images but the laser-induced scattering image shows that the mixing zone indeed does not have a well-defined rear boundary. Rather, small blobs of fluids on the right are scattered in the mixing zone. An inviscid computational study is also done on cylindrical and conical test section geometries to study the effect of transverse reflected waves on the growth of small sinusoidal initial perturbations. It is found by comparison with cylindrical geometry (where reflected waves do not exist) that the transverse reflected waves do not affect the growth of perturbations on the interface.

Contents

List of Figures

List of Tables

Chapter 1 Introduction

When two fluids of different densities are in contact with each other and their interface is accelerated in some way, a wide variety of fluid motions may result. For example, when a heavy fluid is resting on top of a light fluid in a gravitational field, the interface separating the two fluids is unstable with perturbations initially growing exponentially in time. A wide variety of fluid motions result in order to lower the potential energy of thesystem. The same configuration with light fluid on top of heavy fluid is stable with perturbations on the interface remaining bounded. This instability is commonly referred to as Rayleigh-Taylor (RT) instability after its discoverers. In contrast, if the interface separating the two fluids is impulsively accelerated (say by a shock wave), the interface again goes unstable and the resulting instability is referred to as Richtmyer-Meshkov (RM) instability. It differs from the RT instability in the sense that the initial perturbations on the interface grow linearly in time in the beginning. Also, the RM instability does not depend on the direction of acceleration.

The basic mechanism for the growth of initial small-scale perturbations in both RT and RM instabilities is the baroclinic generation of vorticity at the interface with pressure and density gradients not aligned, *i.e.*, $\nabla\rho \times \nabla p \neq 0$. This misalignment creates vorticity of varying strength on the interface which is responsible for the initial growth of the perturbation amplitude on the interface. Figure 1.1 illustrates this for RM instability. As the interface starts to distort, nonlinearities come into play and secondary instabilities, like Kelvin-Helmholtz instability, develop, which help in generating a wide range of scales of fluid motion. The physical mechanism of Kelvin-Helmholtz instability has been described by Batchelor [9] in terms of the vorticity dynamics. This development of nonlinearities and secondary instabilities eventually lead to the development of a turbulent mixing zone at the interface, which continues to grow. In RT instability, the energy is constantly being supplied by

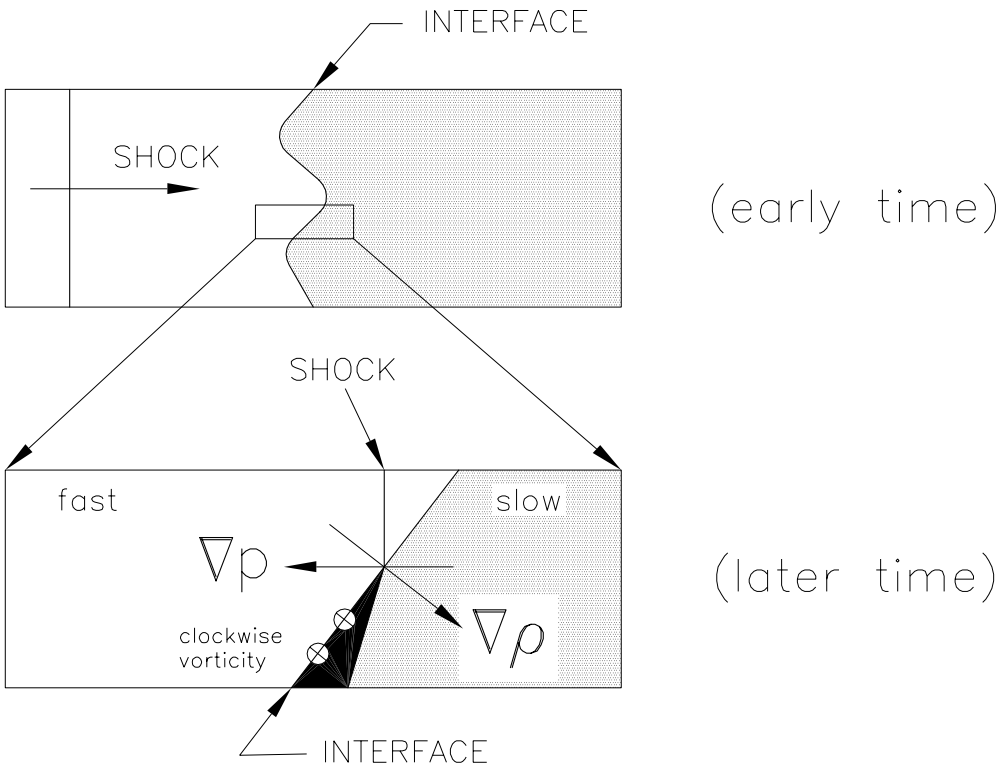

Figure 1.1: Richtmyer-Meshkov instability is generated when the density gradient is not parallel to the pressure gradient (After Sunhara *et al.* [71]).

gravity, while in RM instability the energy for turbulent motions is only supplied at the time of impulsive accelerations, for example, by shock waves. Landau-Darrieus instability [38], driven by mass transfer across the interface, is another instability which grows by the same mechanism of baroclinic vorticity generation.

The RM instability, which arises due to the impulsive acceleration of an interface, finds applications in inertial confinement fusion (ICF) experiments on deuterium tritium targets [43, 2, 44, 42]. ICF is an approach to nuclear fusion that relies on the inertia of the fuel mass to provide confinement. The emergence in the 1970s of inertial fusion as a potential power source has been a major impetus for the study of accelerated and shock-processed interfaces. In such experiments, the target is a small hollow spherical pallet bombarded with very powerful lasers from all around, which heat up the outer ablative shell. As the ablator expands, the rest of the shell is forced inward resulting in an imploding shock. The capsule thus behaves as a spherical, ablation-driven rocket [42]. This process is illustrated schematically in Figure 1.2.

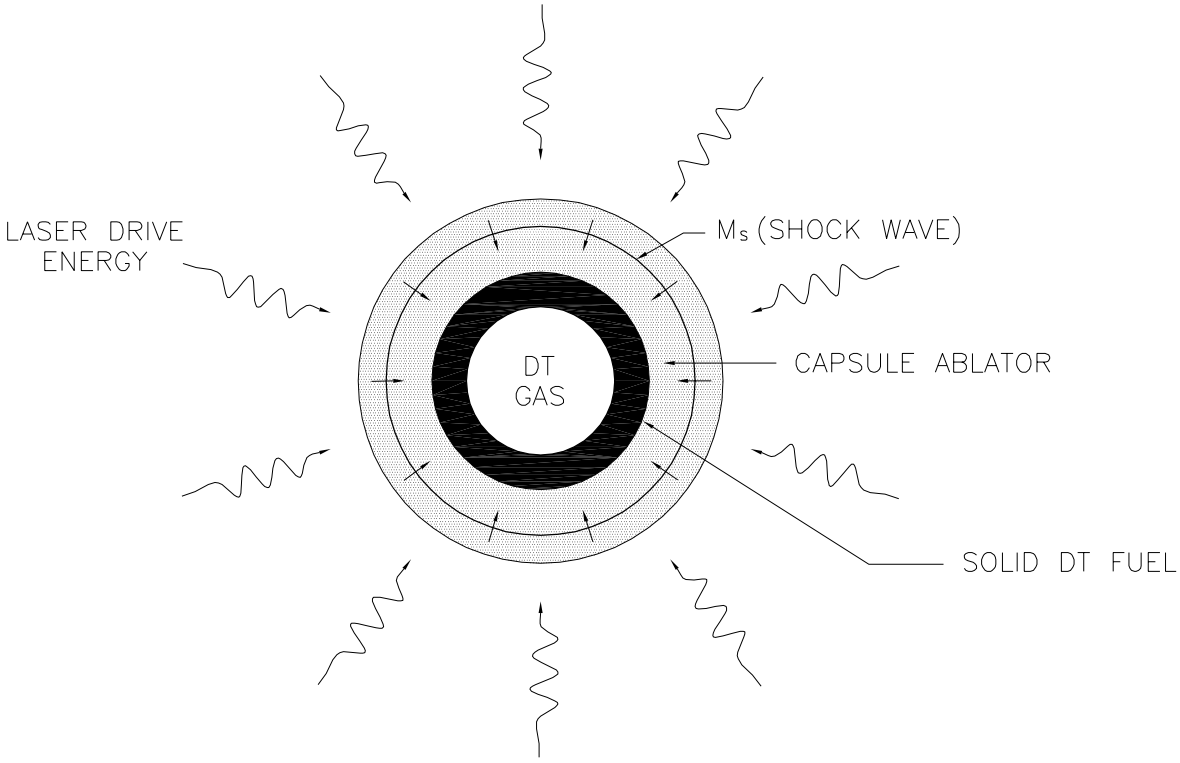

Figure 1.2: Schematic of the inertial confinement of a spherical fuel pellet (After Lindl [42]).

The nuclear fuel inside is thus confined by inertial means. The pressures and temperatures reached in the center of the pallet are favorable for nuclear reaction to start. The imploding shock, on its way to the center, interacts with various density gradients of the pallet shell material. The small unavoidable perturbations on the interfaces of the shell material are the seeds for RM instability. The RM instability induces mixing of the shell ablative material with the nuclear fuel, thus polluting the fuel, which results in low neutron yield or, it might even prevent nuclear reaction from starting. The combination of compressible phenomena, such as shock interaction and refraction with interface instability, including nonlinear growth and subsequent transition to turbulence across a wide range of Mach numbers, has been a challenge to theorists, experimentalists, and computer modelers alike. The RM instability also finds applications in natural phenomena like supernova collapse [68], pressure wave interaction with flame fronts [46], supersonic and hypersonic combustion [45, 75]. The RM instability is now an important element in the numerical models for stellar evolution

and has been used to explain the lack of stratification of the products of supernovae 1987A [7]. The interaction of shock waves with flames which results in RM instability has a important role to play in deflagration to detonation transition [36]. The RM instability can also be useful when mixing is desired between fuel and oxidizers, for example, as in hypersonic and supersonic air breathing engines [77].

To understand the basic physics of RM instability, the present study is undertaken where simplified laboratory experiments are performed in a shock tube. The shock interaction with a perturbed interface between two fluids involves transmission of a shock wave and reflected expansion, or shock wave, depending upon the fluids. The transmitted and reflected waves are corrugated immediately after they are formed because of the perturbations on the interface. If the incident shock wave is sufficiently weak ($M_S \leq 1.5$) and after it has travelled a distance of the order of the wavelength of perturbation, the wave effects on the interface are negligible and the mixing process can be safely considered incompressible. But, if the incident shock wave is very strong, then it influences the motion of the interface (even when the wave is several wavelengths downstream from the interface) through radiation of acoustic energy and hence, the effects of compressibility become more pronounced. This is just one of the many ways in which the compressibility manifests itself. When the incident shock wave is very strong, it also induces motions of high intensity on the interface, resulting in high kinetic energy deposition. This high kinetic energy is finally used up in *compressible* turbulent motions at later times. The RM instability like RT instability goes through various stages of development. When the amplitude of the perturbations on the interface is small (less than 10-40% of the wavelength [67]), the early stages in the growth of the instability can be analyzed using the linearized form of the dynamical equations for the fluid. This is referred to here as early time history of the instability. During the next stage, the amplitude of the perturbations becomes comparable to the wavelength. Nonlinear effects start taking over at this stage. This is referred to as intermediate time stage. Finally, the bubbles and spikes are formed resulting in mushroom-shaped topologies, which eventually break up, leading to turbulent fluid motions. This is referred to here as late time development of the

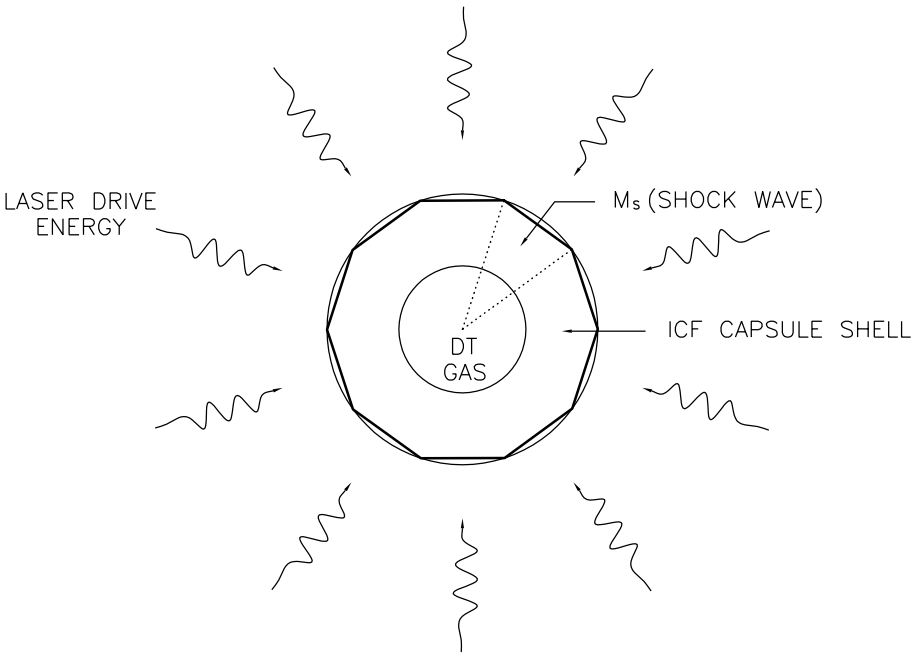

Figure 1.3: Schematic of the piece-wise planar shock imploding in a sphere.

instability (see Figure 1.6 for an illustration in the case of RT instability). The fluid motions in the late time stage are obviously dominated by nonlinearities and multiple scales.

The main focus of this study is to understand the turbulent mixing which results from the shock interaction with well-defined sinusoidal or small-scale random perturbations on the gaseous interfaces. The well-defined sinusoidal interfaces are studied in a straight test section with square cross section, while the small-scale random perturbations are studied in a conical test section. The choice of conical geometry was dictated by the fact that in the case of ICF experiments it is impossible to generate a perfectly spherically symmetric imploding shock. This allows the imploding shock to be approximated by a piecewise planar shock imploding in the sphere. One segment of the imploding shock thus approximates a shock imploding in cone. Actually, the 3-D nature of the piece-wise planar configuration cannot be simulated by the cone. Figure 1.3 illustrates schematically this idea with just ten planar shocks.

Study of RM instability for small-scale random perturbations is important in

ICF applications where there are always uncontrolled perturbations on the interfaces between the ablative shell material.

1.1 Goals of present investigation

This study is primarily aimed at investigating the turbulent mixing that occurs due to RM instability. The present work is a continuation of previous experimental work carried out in the GALCIT 17 in. shock tube by Prasad *et al.* [59]. In this study the impulsive acceleration to the interface is provided by shock waves. The interface starts to grow by RM instability, but very soon, secondary instabilities like Kelvin-Helmholtz instability come into play, resulting in a turbulent mixing zone (TMZ).

The first series of experiments investigates the growth of initial single-mode perturbation on the interface. The interface is examined at very late times using a schlieren system. Visual growth rates (i.e. growth rates measured from the visual measurement of TMZ from the photographs) for various wavelength and amplitude combinations are studied. The second series of experiments was motivated by the convergence effects in ICF target experiments. As explained above, this situation may be approximated by studying RM instability in a conical geometry. The experiments were successful in capturing, for the first time in a conical geometry, the instability growth at late times . The results are then compared with the data of Vetter [74] at the same Mach number of around 1.5 in a straight tube.

1.2 Literature survey

This section gives a review of past and present research in Rayleigh-Taylor and Richtmyer-Meshkov instability.

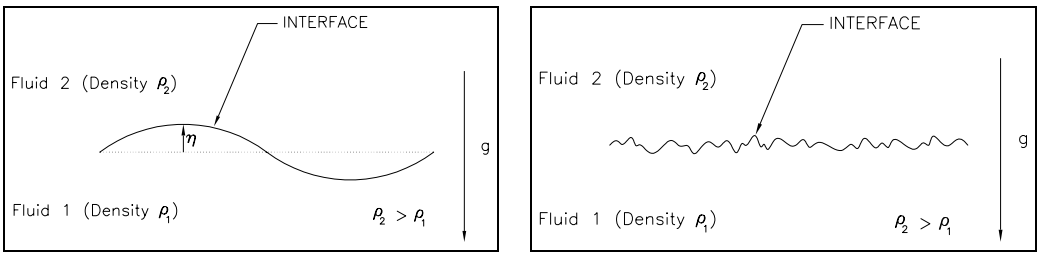

Figure 1.4: Rayleigh-Taylor unstable configurations. a) Single-mode case. b) Multi-mode case.

1.2.1 Rayleigh-Taylor instability

The instability between two immiscible incompressible liquids of different densities under gravitational field was first studied theoretically by Lord Rayleigh [69] and later by Taylor [72]. It was shown that when two immiscible fluids of different densities are accelerated in a direction perpendicular to their interface, this interface is stable or unstable according to whether the acceleration is directed from the heavier to the lighter fluid or vice versa. The case of gravity, g, pointing downwards is equivalent to the two fluids being accelerated upwards with acceleration, g. The RT unstable configuration is called single-mode or multimode according to the initial interface perturbation being well defined by a sinusoidal wave or being random, as shown in Figure 1.4. The linear theory for single-mode configuration developed by Rayleigh and Taylor predicts that the initial amplitude perturbations grow exponentially in time. The linear theory has been modified since then to include surface tension and viscosity [11], molecular diffusion [27], and weak nonlinearity [37]. A detailed account of this instability can also be found in the book by Chandrasekhar [25]. According to the linear theory of Taylor, the interface amplitude grows as

$$\frac{d^2\eta}{dt^2} - kgA\eta = 0, \tag{1.1}$$

where η is the amplitude of the sinusoidal perturbation of the discontinuous interface between two incompressible fluids under gravitational acceleration g; k is the wave

number defined as $2\pi/\lambda$, λ being the wavelength of perturbation; A is the Atwood number across the interface defined as $(\rho_2 - \rho_1) / (\rho_2 + \rho_1)$. Here g is directed from ρ_2 to ρ_1 ($\rho_2 > \rho_1$). Clearly from Equation 1.1, η grows exponentially with time if $A > 0$, showing that the interface is unstable, or oscillates if $A < 0$, showing stability. The growth rate for this classical instability, $n_{\text{classical}}$, is clearly (from Equation 1.1)

$$n_{\text{classical}} = \sqrt{gkA}. \tag{1.2}$$

The first experiments to check the validity of Taylor's theory were performed by Lewis [40] with air-liquid interfaces.

The RT instability in fluid flows with spherical geometry has been studied by several authors [10, 17, 57, 58, 18]. Plesset [57] deduced the conditions for the stability or instability of the interface between two immiscible incompressible fluids in radial motion. He found that the stability conditions derived by Taylor [72] for the interface of two fluids in plane motion do not apply to flows with spherical symmetry without significant modifications. An important fact in curved geometries is that a convergent geometry can itself be destabilizing as explained by Plesset [57] .

In reality, the interface between two fluids will have finite initial thickness. Since the baroclinic torque, being proportional to density gradient, is initially responsible for the RT growth, it is to be expected that the initial growth of finite thickness interfaces will be slower than that of discontinuous interfaces for the same density jump because the density gradient is smaller in the former. RT instability of interfaces having initial finite thickness δ was first studied by Lelevier *et al.* [39] and Duff *et al.* [27]. The basic geometry of the interface they studied is shown in Figure 1.5. The interface is sinusoidally perturbed with wave number k and has a density variation over finite distance resulting in a density profile $\rho(y)$. Chandrasekhar [25] (P. 433) has shown that when the fluid is inviscid and density stratification is continuous, the eigenvalue problem for the growth rate is

$$\frac{d}{dy}\left(\rho\frac{dv}{dy}\right) - \rho k^2 v = -\frac{k^2}{n^2} g \left(\frac{d\rho}{dy} v\right), \tag{1.3}$$

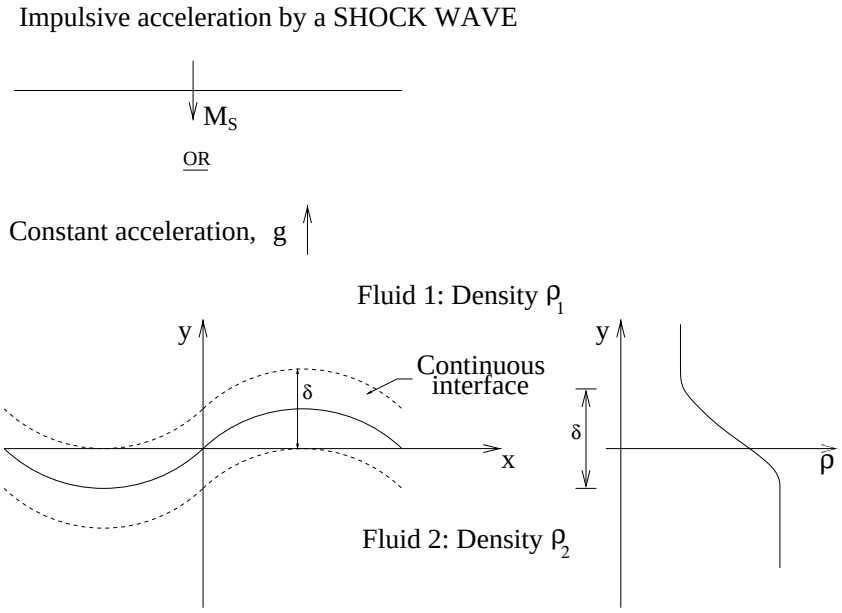

Figure 1.5: Schematic of the initial configuration of the continuous interface.

where v is the y-component of the perturbation velocity and n is the growth rate.

Since the density gradient is now not infinite but finite, the growth rate is smaller than in the discontinuous interface. This led Duff [27] to propose the growth rate for thick interfaces to be

$$n = \sqrt{\frac{gkA}{\psi}}, \tag{1.4}$$

where ψ is the growth reduction factor ($\psi > 1$) and it is a function of interface thickness and Atwood ratio. For discontinuous interfaces $\psi \to 1$, $n \to \sqrt{gkA}$ and for continuous diffuse interfaces

$$\psi = \psi\left(A, \frac{\delta}{\lambda}\right). \tag{1.5}$$

Substituting this proposed value of n in Equation 1.3 one gets an eigenvalue Equation for ψ as

$$\frac{d}{dy}\left(\rho\frac{dv}{dy}\right) - \rho k^2 v = -\frac{k\psi}{A}\left(\frac{d\rho}{dy}v\right) \ . \tag{1.6}$$

Duff *et al.* [27] solved this numerically for a density profile following a complementary error function law. This can be integrated analytically for an exponential density profile as shown by Mikaelian [52] and numerically [27] in other arbitrarily complicated

cases.

Mikaelian [54] also studied the stability of interfaces with arbitrary density profiles by discretizing the profile into N layers, each with uniform density. He showed that there are $2(N-1)$ exponential growth rates which can be found by calculating the eigenvalues of an $(N-1) \times (N-1)$ band matrix. He also found that, in general, the growth rate of one interface is influenced by the presence of the others, but if the wavelength of the perturbations is much smaller than the thickness of the two adjacent layers ($i.e \quad \lambda \ll \delta_i, \delta_{i+1}$) at the i^{th} interface then the interface decouples from the other interfaces and its growth rate reduces to the classical case (Equation 1.2). But if $\lambda \gg \delta_i$ for all i, an interface of N layers behaves very closely to a discontinuous interface with an equivalent Atwood number given by

$$A_{eq} = \frac{\rho_N - \rho_1}{\rho_N + \rho_1 + 2\sum_{i=2}^{N-1} \rho_i \tanh\left(\frac{\pi\delta_i}{\lambda}\right)} \ . \tag{1.7}$$

Since matrix computations become very intensive for large N($\approx$ 200), Mikaelian [51] also proposed an approximate method based on a moment Equation to derive explicit analytical formulas for growth rate of RT instabilities in fluids with density gradients.

Many researchers have studied RT instability in the nonlinear regime both experimentally and computationally. Some of them are Andronov *et al.* [6], Barenblatt [8], Read [61], Youngs [78], Mikaelian [53], Brouillette and Sturtevant [21, 22, 19]. The linear regime is over by the time the amplitude of the perturbations grows to about 0.1λ to 0.4λ. After that, substantial deviations from the linear theory are observed. When the perturbation amplitude grows to the order of λ, the development of the instability is strongly influenced by three-dimensional effects. In a still later stage, the instability is characterized by spikes of heavy fluid falling into lighter fluid and the bubbles of lighter fluid rising into heavy fluid. On the sides of the spikes, which are like jets, Kelvin-Helmholtz instability occurs which causes the mushroom type of roll up to occur. This also causes the spikes to break up and eventually form droplets. This instability development is clearly visible in Young's [78] simulations in Figure 1.6. The Figure shows the calculation at density ratio of 20 at three instants of

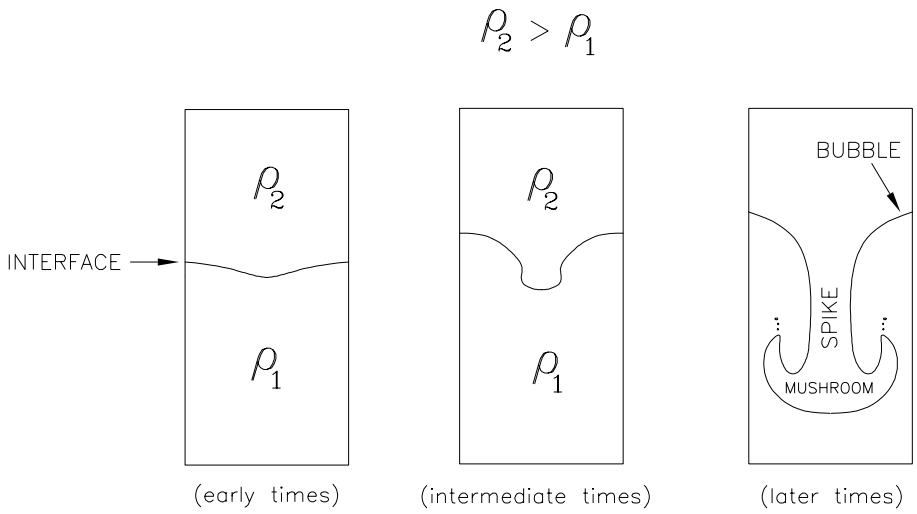

Figure 1.6: Rayleigh-Taylor instability, single wavelength initial perturbation (After Young [78]).

non-dimensional time. At the later times, the mushroom formation at the end of the spike is clearly evident. Also, it is clear that the edges of the mushroom are breaking up into droplets which is characteristic of late times.

There have been a number of attempts to model the spike-and-bubble growth at late times. All of the models have very drastic assumptions built in with the hope of achieving simplicity and capturing the physics to the lowest order. An interesting and simple model in this category is presented by Fermi [29]. He approximates the half-wave of the interface, between two incompressible fluids in the limit of infinite density ratio, by a square wave profile. He then calculates the kinetic and potential energy of the system and uses Lagrange's Equations of motion to obtain a set of coupled ordinary differential Equations. His model correctly captures the late-time growth of spikes, but does not accurately capture the bubble motion. Sharp [67] gives a comprehensive review of both experimental and computational aspects of non-linear development and subsequent turbulent mixing of RT instability.

1.2.2 Richtmyer-Meshkov instability

RM instability is a special case of RT instability when the interface is impulsively accelerated by a shock wave, for example. For this reason it can also be called shock-

induced RT instability. The first analytical study on impulsive acceleration of an interface by shock wave was done by Markstein [46] who investigated the interaction of a shock wave with a density interface (flame front). His analytical result was the same as Taylor's [72] result for constant acceleration. The first rigorous treatment of the impulsive acceleration of the interface by a shock wave was given by Richtmyer [62]. He studied the problem of a shock wave impinging on a sinusoidally perturbed interface between two fluids in the linear regime, *i.e.*, $k\eta \ll 1$. In developing his impulsive model, he assumed that the shock wave is not strong enough to cause perturbation velocities comparable to the speed of sound. Hence the subsequent motion can be assumed to be incompressible. Richtmyer used the result of Taylor (Equation 1.1) replacing the constant acceleration g by an impulsive one, $g = [u]\delta_D(t)$, where $[u]$ is the change in the velocity of the interface imparted by the shock wave and $\delta_D(t)$ is the Dirac Delta function. Substituting this value of g in Equation 1.1 yields

$$\frac{d^2\eta}{dt^2} = k[u]\delta_D\left(t\right) A\eta \ . \tag{1.8}$$

Integrating once, the following expression for growth rate is obtained

$$\frac{d\eta}{dt} = k[u]A\eta_\circ \ , \tag{1.9}$$

where $\eta_\circ$ is the initial amplitude. This expression is valid as long as $\eta k \ll 1$ or $t \ll \lambda^2/\eta_\circ[u]$. From Equation 1.9 it is also clear that the initial amplitude growth is linear in time as opposed to the exponential growth in the RT case. Also, both light-heavy ($A > 0$) and heavy-light ($A < 0$) cases are unstable in contrast to the RT case which has only one situation being unstable. For $A > 0$, the initial amplitude continues growing from the start, while for $A < 0$, the amplitude first becomes zero, reverses sign and then grows according to Equation 1.9.

Richtmyer [62] also did linearized compressible computations using finite difference techniques and found that if the initial compression of the interface and of the fluids is taken into account (*i.e.*, using post-shock values $A^{'}$ and $\eta_\circ^{'}$ in Equation 1.9), the

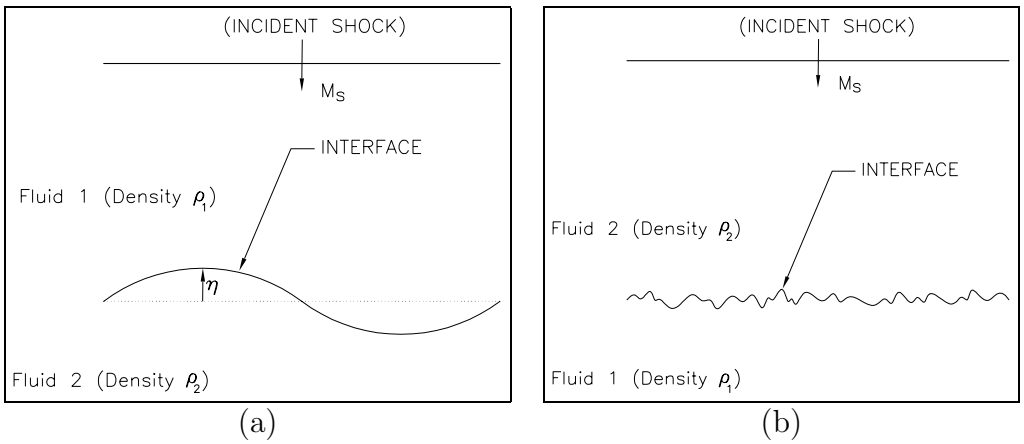

Figure 1.7: Richtmyer-Meshkov configurations. a) Single-mode case. b) Multi-mode case.

ultimate growth of the perturbation as given by the Equation 1.9 agrees, to within 5-10% with his compressible finite difference computations. The corrected impulsive model thus proposed by Richtmyer [62] was

$$\frac{d\eta}{dt} = k[u]A'\eta_o', \tag{1.10}$$

where the primed quantities are post-shock values. This model neglects viscosity, surface tension, and other stabilizing mechanisms.

Laboratory experiments on RM instability have usually been done on two- or three-dimensional, well-defined sinusoidal perturbations, also referred to as the single-mode case, and on small-scale random initial perturbations referred to as the multi-mode case (see Figure 1.7). The multi-mode case is one that is usually encountered in the real life applications such as in ICF target experiments. Meshkov [47] did experiments in a shock tube with a rectangular test section of 120 mm $\times$ 40 mm to study the stability of the single-mode interface of two gases traversed by a shock wave. He found that the interface is unstable both in heavy-light and light-heavy configurations and grows linearly with time in the first approximation. He qualitatively confirmed the predictions of Richtmyer [62]. This class of instability has become known as the Richtmyer-Meshkov instability.

Ever since then, experimental, theoretical, and computational research has been conducted to better understand this instability. Sturtevant [70] pointed out that by using correct post-shock parameters, the growth rate measured by Meshkov [47] can be made to agree more closely with the theory of Richtmyer [62]. Sturtevant [70] also surveyed the status of the experimental work performed in various other configurations. The formula proposed by Richtmyer [62] has also been tested numerically by Meyer [48], who performed two-dimensional numerical simulations of RM instability, and experimentally by Benjamin *et al.* [16, 14]. Meyer found good agreement with Richtmyer's formula only in the case of light-heavy configurations, while in the experiments of Benjamin there was the affect of expansion wave on the growth rate because they used explosives to generate shock waves.

Mikaelian [50] studied the RM instability at an interface of finite thickness by approximating it with an arbitrary number of N layers of fluid, each with uniform density, subjected to a shock. He used the same approach as for the constant acceleration case [54]. Brouillette [23, 19] used the approach of combining Duff's [27] and Richtmyer's [62] suggestions by using the growth reduction factor ψ and replacing constant acceleration g by the impulsive one $[u]\delta_D(t)$. The differential Equation for perturbation amplitude becomes

$$\frac{d^2\eta}{dt^2} = \frac{k[u]A}{\psi}\delta_D\left(t\right)\eta \ . \tag{1.11}$$

One integration of Equation 1.11 gives

$$\frac{d\eta}{dt} = \frac{k[u]A^{'}}{\psi}\eta_{\circ}^{'} \ . \tag{1.12}$$

Brouillette [23, 19] proposed that

$$\psi = \psi\left(A^{'}, \frac{\delta+\delta^{'}}{2}\frac{k}{2\pi}\right) \ , \tag{1.13}$$

where prime denotes the post-shock value. ψ can be evaluated as an eigenvalue problem of Equation 1.6. He numerically evaluated the dependence of ψ on δ/λ for

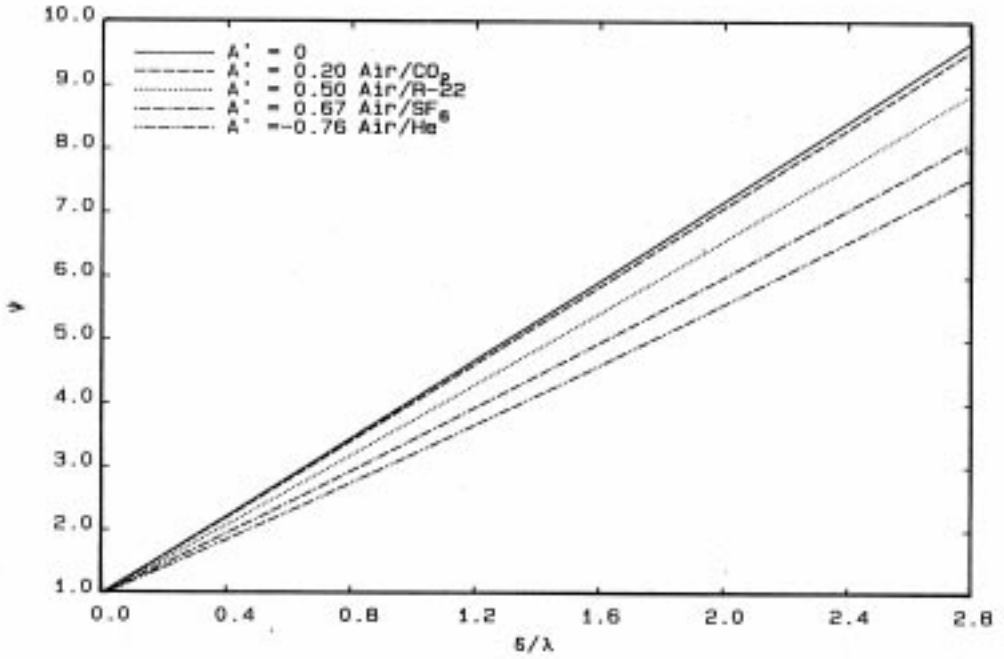

Figure 1.8: Growth reduction factor ψ versus δ/λ. Note here δ represents the mean of pre and post shock thickness (Reproduced with permission from Brouillette's thesis [19]).

various values of A which is shown in Figure 1.8. He used the same density profile as Duff *et al.* [27] and found that ψ increases with δ/λ and decreases with Atwood ratio. This trend was also observed by Duff *et al.* [27] in their computations for RT instability of a diffuse interface. In the case of multiple impulsive accelerations caused by the arrival of many waves at the interface, Brouillette [19] proposed to linearly superpose the affect of each wave as long as the perturbation remains in the linear regime $k\eta \ll 1$. After $(N+1)$ wave interactions, the equation governing the amplitude growth is given by

$$\left(\frac{d\eta}{dt}\right)_N = k\sum_0^N \frac{[u]_i A_i^{'}\eta_i^{'}}{\psi_i} \ , \tag{1.14}$$

where $[u_i]$ is the velocity jump imparted to the interface by the i^{th} wave ($i = 0$ is the main incident wave); $A_i^{'}$ and $\eta_i^{'}$ are Atwood ratio and amplitudes respectively, after the passing of i^{th} wave. ψ_i is evaluated at $A_i^{'}$ and $\delta_i^{'}$.

The impulsive model (Equation 1.10) for RM instability is very attractive for practical use because of its simplicity. It does not give details about the interface development during the very early stages when the shock wave is passing through the interface because that is essentially a compressible phenomenon. Recently, there have been some new impulsive models proposed by Vandeboomgaerde [73], who uses a weighted average of an amplitude-Atwood number combination in the Equation; and by Wouchuck [76], who presents a more complex version of the impulsive model. The relative merits of these impulsive models can be judged by comparing them with exact solutions for the compressible linearized RM instability problem for single-scale interfaces between perfect gases as is done in Brouillette [20]. He shows that in the weak shock limit, both impulsive formulations lead to the same result, which agrees with the exact weak shock solution of Fraley [30]. The discrepancy between impulsive formulations and the exact solutions becomes very large as the shock strength is increased. The impulsive models are based on linear theory so that they are only valid as long as the amplitude remains much smaller than the wavelength.

Experimental research in RM instability is mostly centered around measuring the growth rate of the interface. The overall interface thickness gives an idea of integral scales involved in the mixing process. As the instability grows, a large range of scales develops due to the development of Kelvin-Helmholtz type of secondary instabilities and the flow becomes turbulent near the interface. This turbulence leads to further growth of the interface by entrainment. In this instability, the turbulence generated by the shock wave is highly anisotropic in the initial stages as the vorticity deposited by the interaction of the shock wave lies primarily in the plane of the shock wave. As more and more scales develop, the flow becomes independent of initial conditions and the behavior of the interface growth is then thought to become self-similar governed by local length and time scales [31]. The turbulence near the interface then tends to become isotropic at late times (*i.e.*, when a large range of scales has developed) because of the disappearance of the dependence on initial conditions. The thickness of the interface (or TMZ), δ, defined here as the full width of the interface from the

front to the back then grows as a power law of time,

$$\delta \propto t^m \ . \tag{1.15}$$

Aleshin *et al.* [3] studied the growth of single-mode perturbations excited by incident shocks of Mach number, $M_S = 3.5$ in a shock tube of test section 72 mm $\times$ 72 mm. They were perhaps the first to observe the transition from the linear to the nonlinear regime in laboratory experiments. They found that the transition to the nonlinear stage is accompanied by a slowing of the growth of the perturbation amplitude. Brouillette and Sturtevant [22] conducted experiments in a 114 mm square shock tube on nominally plane multimode interfaces initially established by thin plastic membranes. They made observations up to times corresponding to $x/\delta \sim 20$, where $x = [u]t$. The observed growth rate induced by single incident shock waves decreased rapidly with time. The quantity of data was not sufficient to determine m quantitatively, but they showed that $0 < m < 1$. Recently, Sadot *et al.* [63] conducted experiments in a shock tube at $M_S = 1.3$ to observe the initial stages of nonlinearly saturated growth of single mode perturbations to $x/\delta \sim 5$. They found an interpolation formula which captures linear, early nonlinear and asymptotic behavior of the bubble and spike evolution.

Haan [31] discussed the late-stage growth in the RT case and suggested that, for large enough time, the amplitudes of initially single-mode and multi-mode perturbations should be comparable. He also shows that in the presence of full spectrum of modes, the nonlinear behavior begins whenever the sum of modes over a specified small region of wave-number space becomes comparable to the wavelength. His model provides a description of weak dependence on initial amplitude. Barenblatt [8] considered the problem of a turbulent plane layer forming instantaneously in an infinite incompressible and homogeneous fluid. He used the Kolmogorov similarity hypothesis together with an assumption that the turbulence integral length scale is equal to a certain fixed part of actual turbulent layer depth to obtain an upper limit of growth rate power for a dissipation-less fluid as $m = 2/3$. Mikaelian [49] analyzed the RT

experiments of Read [61] who obtained the mixing height δ as

$$\delta = 0.14 \left(\frac{\rho_2 - \rho_1}{\rho_2 + \rho_1} g t^2 \right). \tag{1.16}$$

at late times. From this, one gets

$$\frac{d^2\delta}{dt^2} = 0.28Ag. \tag{1.17}$$

Mikaelian [49] substituted the acceleration due to gravity g by $[u]\delta_D(t)$ in Equation 1.17 to obtain by integration,

$$\delta = 0.28A^{'}[u]t, \tag{1.18}$$

where $[u]$ as previously is the velocity to which the interface is accelerated by the incident shock wave. This result was applied to estimate the turbulent kinetic energy in the large scale structures of the flow where the Barenblatt constraint $m \leq 2/3$ need not apply. Mikaelian [49]applied the Canuto-Goldman [24] analytical model to turbulence generated by a class of instabilities which have a power law growth rate. When applied to RT instability at least an order of magnitude difference between largest and smallest eddies is found which Mikaelian called as chunck mix. When applied to RM instability the predictions are that largest and smallest eddies do not differ in size by more than 60% and Mikaelian calls it atomic mixing. Mikaelian [49] also finds, independently of Canuto-Goldman model, that the ratio of turbulent to directed kinetic energy is about 2% and 9% for RT and RM cases, respectively, and varies as the square of the Atwood number in both cases. Saffman and Meiron [65] also calculated the kinetic energy generated by impulsive acceleration of an incompressible, continuously-stratified fluid. They obtained solutions for small-density perturbations and a hyperbolic tangent density profile for various Atwood numbers and length scales. They found that the kinetic energy (in the reference frame of directed fluid motion) deposited by the incident shock is reduced when the undisturbed density profile is more diffuse. Similar calculations of kinetic energy were also performed by

Mikaelian [55] who calculated the ratio of directed kinetic energy, E_{dir}, and turbulent kinetic energy, E_{turb}, for accelerating (RT case) or shocked interfaces (RM case) by assuming a linear density profile across the mix region and found that $E_{turb}/E_{dir} = 0.023\ A^2$ for a constant acceleration, and $0.093\ A^2$ for a shock. E_{turb} is the potential energy lost during the mixing process and directed kinetic energy is the energy due to the velocity gained as a result of constant or impulsive acceleration. These are calculated (per unit area) by Mikaelian [49, 55] for linear density profile as follows,

$$\begin{aligned} E_{turb}(RT) &= \frac{g}{6}\left(\rho_2 - \rho_1\right)\left(\frac{\delta}{2}\right)^2 \\ E_{dir}\left(RT\right) &= \frac{1}{2}\left(gt\right)^2\left(\rho_2 + \rho_1\right)\left(\frac{\delta}{2}\right) \\ E_{turb}\left(RM\right) &= \left(\frac{0.14[u]^2\left(\rho_2 - \rho_1\right)^2}{3\left(\rho_2 + \rho_1\right)}\right)\left(\frac{\delta}{2}\right) \\ E_{dir}\left(RM\right) &= \frac{1}{2}\left([u]^2\right)\left(\rho_2 + \rho_1\right)\left(\frac{\delta}{2}\right) \end{aligned} \tag{1.19}$$

These results qualitatively agreed with Mikaelian's [49] earlier investigation. Mikaelian could also predict eddy sizes for RT and RM mixed interfaces by assuming a density profile based on self-similar solutions to nonlinear diffusion Equations [55].

Recently, Alon *et al.* [4, 5] analyzed the late time growth of multimode fronts using a two-dimensional bubble merging and competition statistical model proposed by Sharp and Wheeler [67]. In this model, a series of bubbles is distributed according to an initial distribution function whose evolution is governed by a conservation Equation (see Equation 1 in ref. [4]). The bubbles are allowed to rise and merge according to a simple potential flow model of bubble evolution at an interface between an incompressible fluid an a much lighter fluid (see discussion by Alon *et al.* [4] for more details). In this model, smaller bubbles get continually absorbed into larger ones, and

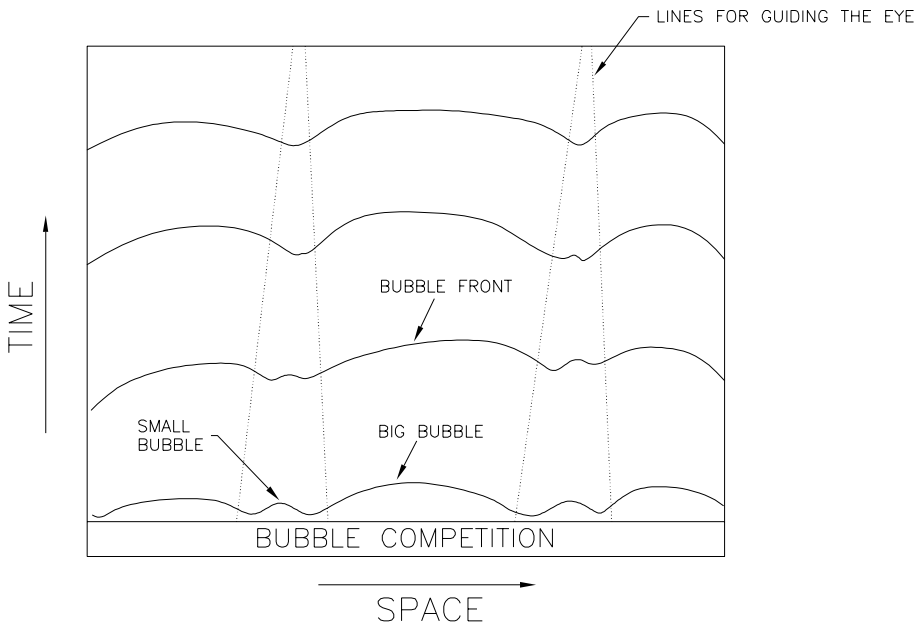

Figure 1.9: Schematic of bubble merging and competition at late times of RM instability.

the opposite process of break-up of large bubbles into small ones does not occur, the average size of the bubbles, and hence the average velocity of the bubble rise, increases with time. Figure 1.9 shows schematically how the smaller bubbles are merged into larger bubbles with time.

Alon *et al.* [5] find that for A=1 and RT mixed interface, the bubbles and spikes evolve as $h_B = \alpha_B g t^2$ and $h_S = \frac{1}{2} g t^2$ with $\alpha_B = 0.05$, where h_S, h_B are spike and bubble heights and α_B is a constant. For $A = 1$ and RM mixed interface the bubbles evolve as $t^{0.4}$ and spikes with constant velocity, *i.e.*, $\sim t$. Therefore in RM mixed interfaces at $A = 1$ the bubble and spike fronts follow different power laws in time. For all other Atwood numbers, multimode RT bubble (spike) fronts are found by Alon *et al.* [5] to grow as $h_B = \alpha_B A g t^2$ ($h_S = \alpha_B(A) g t^2$) with $\alpha_B = 0.05$, while RM bubble (spike) fronts are found to grow as $h_B = a_B t^{\theta_B}$ $\left(h_S = a_S t^{\theta_s(A)}\right)$ with $\theta_B = 0.4$ for all Atwood numbers. h_B and h_s are bubble and spike heights and $\alpha_B, \alpha_S, a_S, a_B$ are coefficients which might depend on A in some cases and on initial conditions. Their [5] power laws and exponent variation with Atwood number is shown in Figure 1.10.

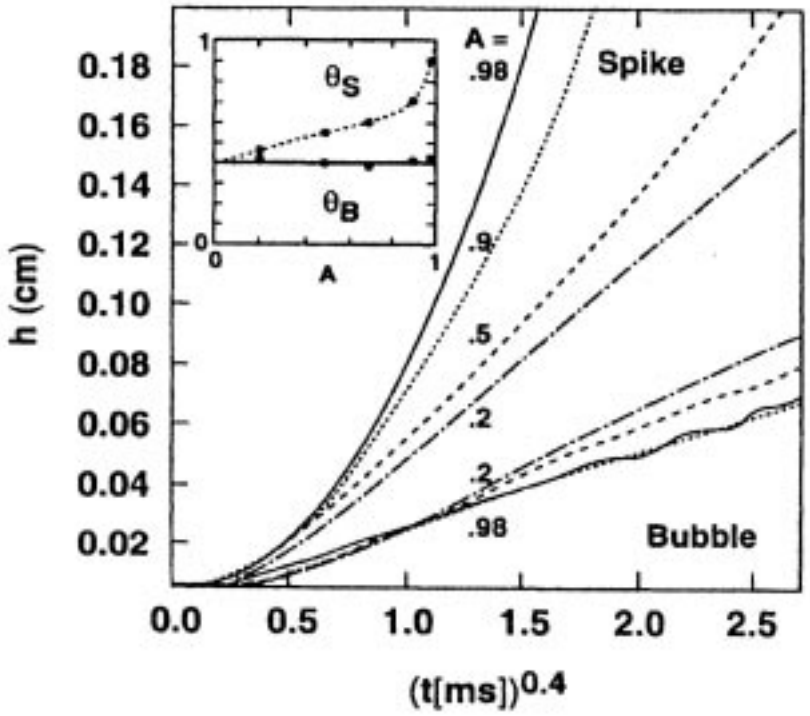

Figure 1.10: RM random bubble and spike-front penetration (defined at 90% of the heavy and light fluid volume fractions, respectively) versus $t^{0.4}$. Inset: power-law exponent θ_B and θ_s (Reproduced with permission from Alon *et al.* [5]).

Zhang and Sohn [80] developed a quantitative nonlinear theory of compressible RM instability in two dimensions from early to later times. They [80] adopted the physical picture that dominant effects of compressibility occur near the shocks. It is assumed in this theory that the initial disturbance at the interface is small. Thus at early times the compressibility is important and the nonlinearity is less important implying that the linear compressible Euler Equations are applicable. At late times the magnitude of the disturbance at the material interface increases significantly and the transmitted shock and the reflected wave move away from the interface. The effects of compressibility are then reduced and the nonlinearity starts to play a dominant role in interfacial dynamics. The dynamics are then mainly governed by the nonlinear incompressible Equations of motion. The RM unstable interface goes through a transition from a linear and compressible one at early times to a nonlinear and incompressible one at later times. Zhang and Sohn [80] developed a perturbation series

solution to the incompressible nonlinear flow Equations in amplitude and extended its range of validity by Padé approximations [12]. Using the methods of matched asymptotic expansions [12], the perturbation solution at late times was matched with the linear compressible early time solution to obtain a uniformly valid solution for the growth rate for spikes and bubbles. Their [80] nonlinear theory agrees with the shock tube experiments of Benjamin, Besnard and Haas [15], suggesting that these experiments were in the nonlinear regime. This is also consistent with Benjamin [13] who observed that the interface was nonlinearly deformed despite the fact that its thickness was growing linearly in time. For relatively large A, their [80] overall growth rate varies as t^{-1} implying that $\delta \propto \ln t$. For relatively small Atwood numbers, their [80] growth rate varies as t^{-2}. Pham and Meiron [56] simulated the late time behavior of both single mode and multimode initial perturbations in continuously stratified fluids. They [56] do not find any long time self similar behavior in growth for single mode case. For the multimode case, a weak scaling behavior in the growth of the interface thickness is observed [56]. The interface thickness δ scales with $t^{1/4}$ in contrast to Barenblatt's $t^{2/3}$ scaling which is attributed to inhomogeneity and anisotropy.

At very late times in the development of RM instability, the turbulent motions are slow, the flow becomes viscous and the local Reynolds number,

$$Re = \frac{u^{'}\delta}{\nu} \sim \frac{\delta^2}{\nu t} \tag{1.20}$$

may be constant or even decrease with time. Here $u^{'}$ is the late time turbulent *rms* velocity scale which is assumed to be of the order $u^{'} \sim d\delta/dt \sim \delta/t$. The behavior at these times has recently been studied by Huang and Leonard [34] by numerically simulating incompressible homogeneous turbulence. They observe a late time similarity that yields a power law decay for the turbulent energy with exponents approximately equal to 1.5 to 1.25 depending on the Reynolds number (based on Taylor microscale). Using the hypothesis of Saffman [64] that the integral moments of the vorticity distribution in the large scales of turbulence are bounded, an invariant of motion is determined that fixes the energy decay rule to be $t^{-3/2}$. For the problem

of the RM mixed interface with no area convergence, this suggests that

$$u^{'} \sim \frac{d\delta}{dt} \sim t^{-3/4} \ . \tag{1.21}$$

$$\delta \sim t^{1/4} \ . \tag{1.22}$$

To summarize, theoretical considerations suggest that when $A \neq 1$ the late time RM asymptotic amplitude growth may be between logarithmic and linear in time.

There have been many experimental results reported for growth of the interface after excitation by more than one shock wave, called *reshock*. For example, in several experiments all carried out in the same shock tube [21, 22, 23, 19], Brouillette and Sturtevant reported growth linear in time after reshock by one or more reverberations between the shock tube end wall and the interface. The interface growth rate in most cases was somewhat smaller than that predicted by Equation 1.18. Experiments in a larger shock tube (GALCIT 17 in. shock tube) by Vetter [74] yielded a linear growth after reshock, with growth in better agreement with Equation 1.18 which is valid when the mixing zone is in nonlinearly saturated regime (see Figure 1.11). This agreement suggests that the growth after reshock is in the nonlinearly saturated regime. From Figure 1.11 it is clear that the growth rate decreases just before the arrival of the reflected shock. The linear growth after reshock was observed at about the same time when the growth due to the incident shock was decaying, which suggests that the turbulence in the TMZ is re-energized by successive shocks. Vetter carried out experiments with an impulsively accelerated air/SF_6 multimode interface. The relatively larger test section size of this 17 in. shock tube helped to reduce the wall boundary layer effects. Vetter [74] gives an account of the sizes of the test sections which were used for such a study. He found that the thin membrane which separates the gases has significant influence on the initial growth rate of the TMZ. However, the measured growth rates after reshocks or at very late times were independent of the membrane configuration and agreed well with the theory (Equation 1.18). A very comprehensive review of RM instability, including experimental, theoretical and computational aspects of it, is given in a very recent review article by Brouillette [20].

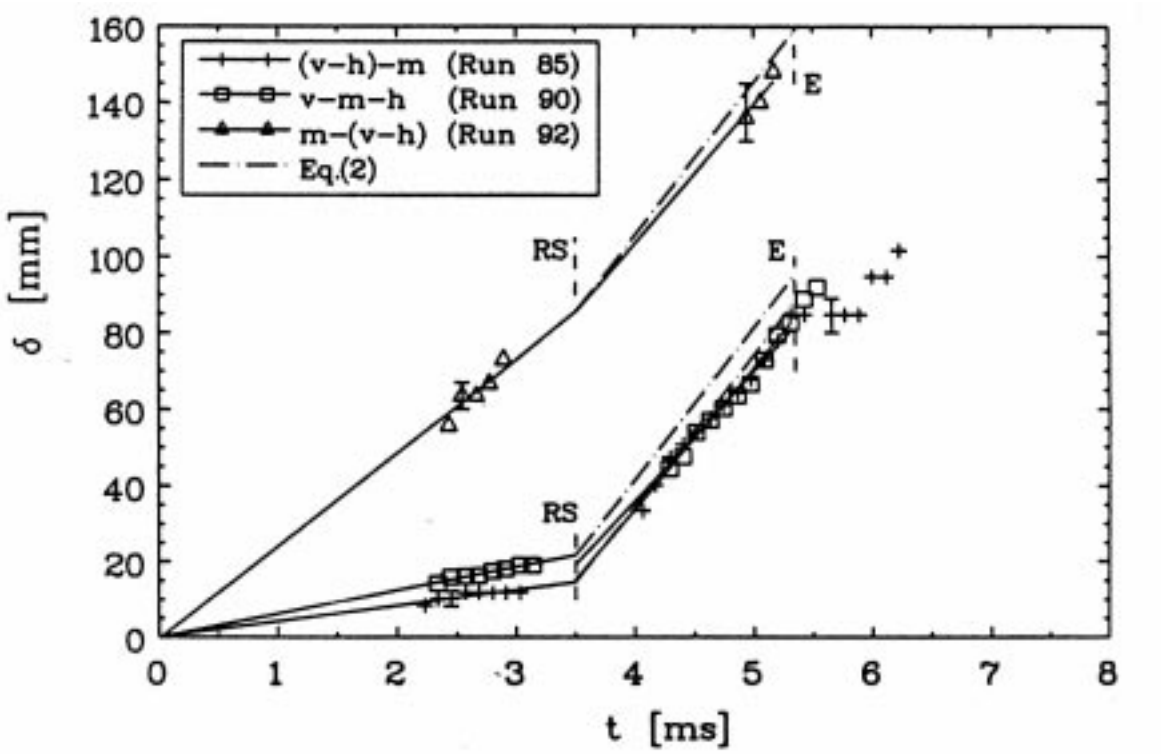

Figure 1.11: Time evolution of the thickness of the TMZ for a plane discontinuous interface between air and SF_6; results from high-speed motion pictures; $M_S = 1.5$; the legend shows the wire mesh-membrane arrangement between air and SF_6: v-vertical wire mesh, h-horizontal wire mesh, m-membrane (RS: reflected shock; E: expansion) (Reproduced with permission from Vetter [74]).

To summarize, the experimental, theoretical and computational research effort in RM instability has been directed mainly towards determining the interface growth rate at early and late times. The early time picture, though being complicated by compressibility effects, is understood reasonably clearly but there is discrepancy between various researchers on late time RM growth rate. The issue of the growth at late times being self-similar and the extent of the influence of initial conditions remains unresolved. These questions are important in the ICF applications [42]. In ICF experiments area-convergence is another factor which effects the RM interface flow physics and needs to be understood. The present study is an effort to understand these unresolved issues.

The main purpose of this study is to experimentally investigate the growth of single-mode perturbations in a 254 mm $\times$ 254 mm square test section at late times

and also investigate the growth rate of multimode initial perturbation of the interface in the conical geometry to simulate the area convergence effect. Comparison of the results in conical geometry with Vetter's [74] results at the same Mach number of 1.5 should give insight into the effect of area convergence on the TMZ growth rate. When a shock wave propagates into a cone, it is reflected from the wall and a Mach stem might form at the boundary with the triple point moving towards the centerline and reflecting from there. It is not the objective of the present investigation to study these nice changes in the shock waves. This has been studied in adequate detail by Setchell [66], and the Mach reflection phenomenon has been well documented by Hornung [32] among others. In the present investigation, the emphasis is on the study of fluid mechanics at the interface.

Chapter 2 Experimental Apparatus

2.1 Introduction

The main focus of this study is to understand the growth of the interface at late times as a result of the RM instability. This exercise was undertaken to study the TMZ growth resulting from the RM instability in a straight test section and in a conical test section in order to understand the area convergence effect. The experiments for this study on RM instability were performed in a horizontal shock tube with circular cross section having an internal diameter of 17.125 in. The size of the shock tube helped to minimize affects due to boundary layers on the main fluid dynamical phenomenon under investigation. It was designed and built by Liepmann *et al.* [41] at GALCIT and is known as the GALCIT 17 in. shock tube. At the end of the shock tube two different types of test sections are used. One is a straight test section with square cross section (10.5×10.5 in.) which had been used for the study of single-mode RM instability and the other is a conical test section. In the former, the transition from circular to square cross section is achieved through a cookie cutter. Machining and installing windows into the plane side walls of the straight test section provided flow visualization. In the case of conical test section, the entrance diameter to the cone (half angle = 10 degrees) is 17.125 in. matching the internal diameter of the shock tube. Installing of windows on the sides of the conical test section was not straightforward. The two parts of the straight test section can be rotated to provide four locations downstream of the initial interface for diagnostics of the TMZ. The presence of windows in the test sections limit the maximum internal pressures which in turn limit the Mach numbers at which the experiments can be performed. In the present experiments, a shock wave is launched by bursting the diaphragm due to over-pressure. The shock wave interacts with the interface of two gases at the junction of the shock tube and test section. This results in RM instability and subsequent turbulent mixing. The

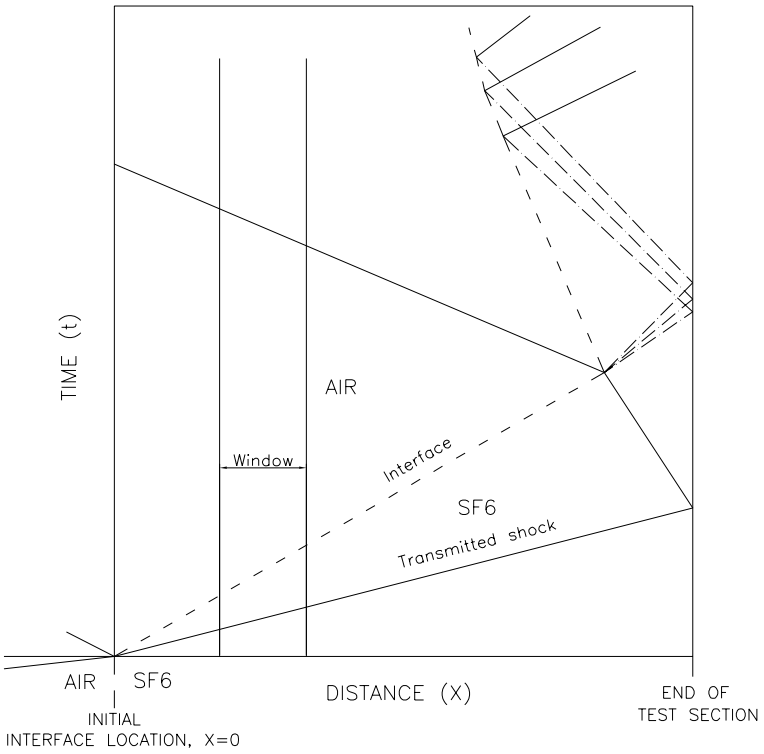

Figure 2.1: Schematic of the x-t wave diagram for straight test section experiments (not to scale).

diagnostic is schlieren imaging techniques for single-mode interface in a straight test section. For the conical test section the diagnostics are schlieren and laser-light sheet scattering using an Nd-Yag laser. The incident shock Mach number in the straight test section study is 1.55 and in the conical test section is about 1.55 and 1.39.

2.2 Overview of the experiment

Single-mode initial interface growth is studied in a straight test section geometry. Figures 2.10 (a) and 2.1 show schematically the straight test section and the corresponding x-t wave diagram. This study on the straight test section is a part of the study done by Prasad *et al.* [59]. Window location marked 1 in Figure 2.10 (a) is used in the present study to obtain additional data. The interface is visualized after interaction with the incident shock, but before the interaction of reflected shock from the end of the test section. Two different interface disturbance wavelengths and

amplitudes are studied at one axial location using the schlieren visualization system.

The experiments on RM instability growth in a conical test section involve observing the interface geometry with the schlieren system at three axial locations along the cone axis. The centers of the observation windows along the cone axis are located at $x/L = 0.103$, 0.268 and 0.232, L being the length of the cone assuming it ends in a point vertex. These are referred to as first circular window, second rectangular window, and third rectangular window, respectively. A light-heavy configuration using air/SF_6 and a heavy-light configuration using air/He are studied. The interface thickness is measured visually from the schlieren pictures. Planar laser-induced scattering using olive oil mist as seeding in the test gas is also tried in the heavy-light configuration. The interface in this case is captured by a CCD camera using a frame grabber software installed on a computer. The basic schematic of the setup with conical test section attached to the shock tube and the corresponding x-t wave diagram at the cone centerline is shown in Figure 2.2. The test section shows the rectangular window at $x = 13$ in. The initial interface in the experiments is formed by a thin polymeric membrane which is held between wire-mesh frames.

The rest of this chapter deals, in detail, with various aspects of the experimental setup including the facility, test sections, interface formation and flow visualization.

2.3 Shock tube

A schematic of the tube is shown in Figure 2.3 (a). It is the same sketch as in Liepmann *et al.* [41] except that the length of the driven section is changed. The shock tube design is described in detail by Liepmann *et al.* [41]. For convenience, a very brief description is included here.

2.3.1 Driver section

The driver section is 12.5 ft long made from 17 in. internal diameter 304 stainless steel pipe with a wall thickness of 0.5 in. The inside surface is not honed and the

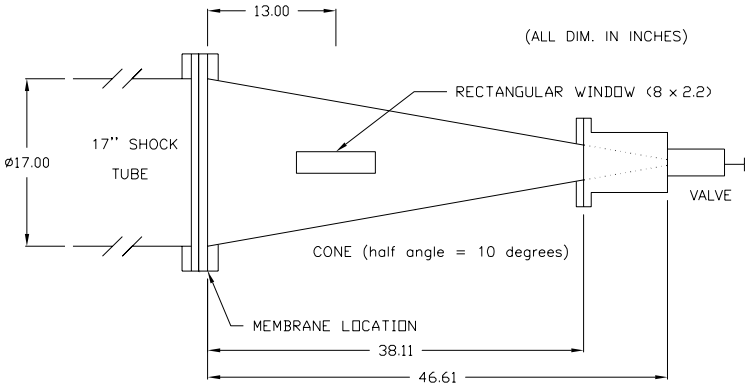

SCHEMATIC OF CONICAL TEST SECTION
(showing the second rectangular window)

(a)

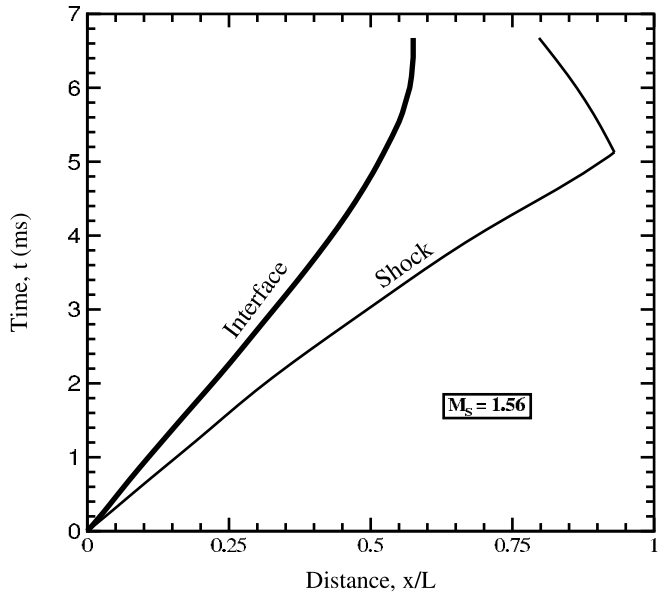

(b)

Figure 2.2: Conical test section. a) Schematic drawing showing second rectangular window placement. b) $x - t$ wave diagram in the conical geometry showing the interface and shock trajectory in light-heavy configuration at Mach number of 1.56. Here L is the length of the cone and x coordinate is measured from the initial interface location into the cone. The $x - t$ diagram was drawn from the numerical simulation performed on AMRITA [60]. The trajectories refer to the location of interface/shock on the cone axis.

flanges are attached by circumferential structural welds. The maximum pressure for this section is 15 atm although a test up to 33 atm has been carried out to check the integrity. At the end, it is closed by a 1.5 in. thick plate with provisions for gas filling and vacuum pump attachments. The whole shock tube is mounted on a rail hanging from the ceiling. The driver section can be translated away from the diaphragm section in order to change the diaphragms. The photograph in Figure 2.3 (b) shows the view along the shock tube's driver section.

2.3.2 Diaphragm section

The diaphragm section of the shock tube connects the driver and the driven section and holds the diaphragm and the cutting device. A quick opening clamp secures the two mating flanges uniformly around their circumference. The clamp can be opened by the motion of a cam-locking device which is controlled by a solenoid-driven locking pin. A diaphragm assembly consists of the diaphragm bolted at its circumference between two heavy rings. This in turn rests between the two mating flanges. A cruciform blade cutting device is used for bursting the diaphragms. The blades are on the low pressure side of the diaphragm and cut it as it bulges against the blades due to higher pressure on the driver side. Pictures in Figure 2.4 (a,b) show the diaphragm section of the shock tube and the diaphragm before and after the shock tube is fired.

2.3.3 Driven section

The basic driven section is 66.8 ft long and consists of the same pipe as the driver section. The inside of the pipes in this section is honed to a surface finish of approximately 40 μin. The anchor side of the driven section incorporates the downstream half of the diaphragm joint and is also fitted with the two 6 in. ports leading to the vacuum pumping system. The driven side is also equipped with pressure ports at various locations where pressure transducers can be mounted to measure the speed of the shock. In the current setup there are two high-resolution pressure transducers

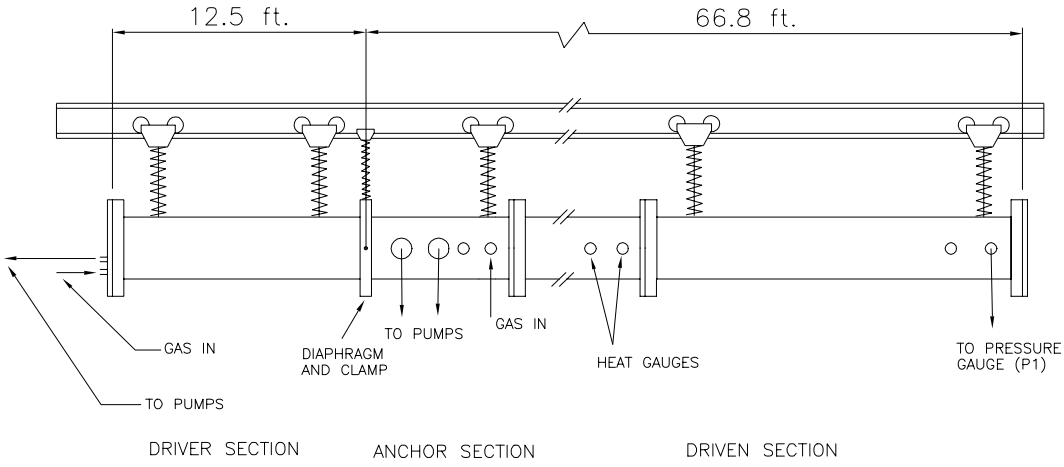

(a)

(b)

Figure 2.3: GALCIT 17 in. shock tube. a) Schematic (After Liepmann *et al.* [41]). b) Photograph showing the driver section.

(a)

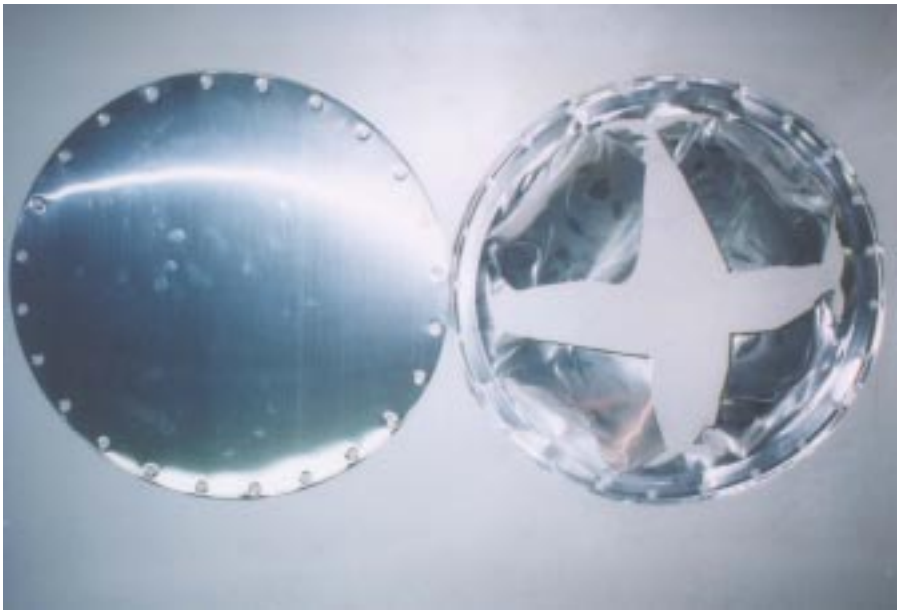

(b)

Figure 2.4: a) Diaphragm bursting section of GALCIT 17 in. shock tube showing the cruciform blade cutting device. b) diaphragm before and after the shot.

(Model No.112A21 from PCB Piezotronics) mounted at distances of 1.823 m and 5.131 m from the open end (the end where the test section is mounted) of the tube. The distance between the gauges is thus 3.308 m which is used to measure the Mach number from the pressure traces.

2.4 Interface mounting system

To study single-mode perturbation on the interface, the experiments are done in a straight test section with a square cross section of 10.5 × 10.5 in. In order to cut the circular shock wave to a square of this size, a cookie cutter is inserted 60 in. into the shock tube from the open end. No cookie cutter was needed for the conical test section whose entrance diameter matches the internal diameter of the shock tube (17.125 in.). In order to seperate the gases, a 1.5 μm thick nitrocellulose membrane is used. Different mounting systems are used for this membrane to provide well-defined sinusoidal or random perturbation.

2.4.1 Interface mounting system for single-mode case

To study RM instability with well-defined sinusoidal perturbations between two gases, two frames of different wavelength and amplitude were used. Since this study was a part of the study carried out by Prasad *et al.* [59] on four single-scale configurations, the frames considered here were frames 2 and 3 from that work and are also referred here by the same names. The run conditions and the wavelengths and initial amplitudes studied here are given in Table 2.1.

Frame	$\lambda_\circ$ (mm)	$k_\circ$ (mm^{-1})	$\eta_\circ$ (mm)	$k_\circ\eta_\circ$	Symbol used
2	59.3	0.106	5.91	0.62	□
3	106.7	0.059	5.33	0.31	◊

Table 2.1: Experimental conditions. Air/SF_6, M_s=1.55, U_i=174 m/s, A=0.67, A$'$=0.74

Of the four configurations studied by Prasad *et al.* [59], Frame 2 had the largest amplitude and Frame 3 the largest wavelength. Both frames are made of brass with

inner dimensions of 10.5 × 10.5 in. and outer dimensions of 11.3 × 11.3 in. Each frame has a mating part and together sandwich the nitrocellulose membrane between them to give it an almost sinusoidal shape. An array of thin wires running across the frames was necessary to support the interface across the width of the tube. The array consisted of twenty-six, equally spaced 0.18 mm diameter wires running from one face of the frame to the opposite. The wires are soldered in small slots at the ends. The photographs in Figure 2.5 (a,b) show the frames and the wires. To place the sandwiched membrane in between the shock tube and the test section, a square aluminum support is used to hold the unit consisting of the two frames and the membrane (Figure 2.5 (c)). This combined unit is then bolted between the shock tube and the straight test section. When the membrane was placed on top of the frames, the wires were approximately 1 mm on either side of it because of the way the wires were soldered to the frames. Figure 2.6 indicates the interface configuration as formed near the origin (x, $z = 0$) by the pair forming Frame 2. The membrane is cut into ribbons by the wires after the shock wave interacts with the interface. The nominal shape of the interface is described by

$$\eta(z) = -\eta_0 \cos k_0 z; \quad -10.5 \leq z \leq 10.5 \text{ in.}, \tag{2.1}$$

where the coordinates are defined in Figures 2.6 and 2.10 (a), η increases in the direction of increasing x, $k_\circ$ and $\eta_\circ$ are given in Table 2.1. The sign on $\eta_\circ$ indicates that on the centerline of the tube all membranes initially formed a crest pointed upstream relative to the mean position of the interface, $x = 0$. The sinusoidal shape is maintained accurately at the perimeter of the shock tube by the machined frame. However, near the center of the shock tube the membrane was stretched against the upstream supporting wires as the pressure in the test section was always kept slightly higher than in the driven section. This introduced higher harmonics in the nominally sinusoidal shape. The amplitude of the second harmonic, expressed as a percentage of the first harmonic was 3.7% for Frame 2 and 1.2% for the Frame 3. This was determined by doing the Fourier transform of the profile made up of straight

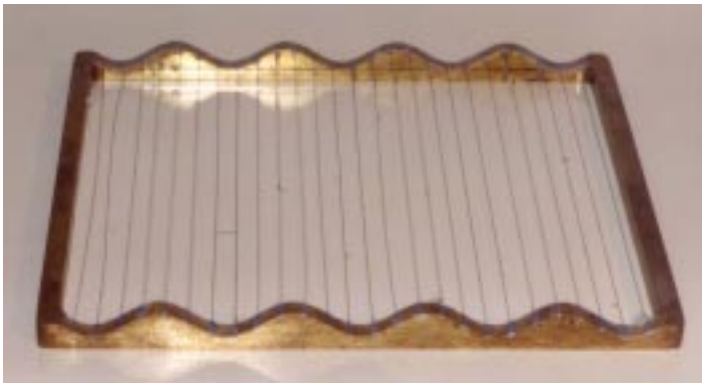

(a)

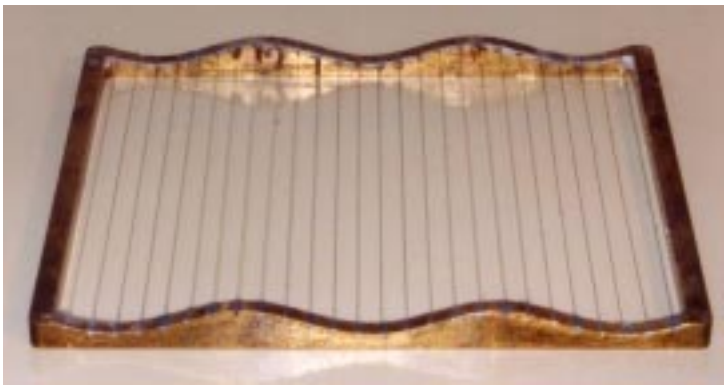

(b)

(c)

Figure 2.5: Sinusoidal frames to hold the nitrocellulose membrane. a) Frame 2, $\lambda_0 =$ 59.3 mm, $\eta_0 = 5.91$ mm. b) Frame 3, $\lambda_0 = 106.7$ mm, $\eta_0 = 5.33$ mm. c) Aluminum support holding Frame 2.

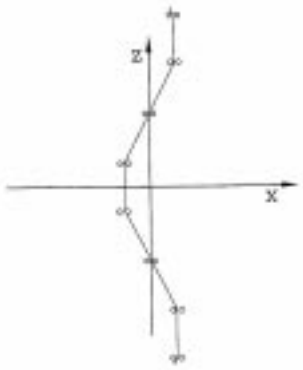

Figure 2.6: Schematic diagram of one wavelength of the membrane near $x = 0$, $z = 0$, showing the arrangement of the wire-mesh for Frame 2. (Reproduced from Prasad *et al.* [59])

line segments. Furthermore, imperfections in the nitrocellulose membrane introduced additional undefined very-small-scale perturbations.

2.4.2 Interface mounting system for multimode experiments in conical test section

To study the RM instability in a conical test section, the cookie cutter was removed and three sets of circular frames were made. All of the circular frames had internal diameter matching that of the shock tube. One of these was bolted on to the shock tube permanently with eight half inch studs protruding on its periphery at the bolt circle of 20.26 in. On these studs was attached the assembly consisting of two wire-mesh frames sandwiching the nitrocellulose membrane and another aluminum support holding them. This concept was similar to the one used in single-mode experiments.

The circular wire-mesh frame was made from aluminum with internal and external diameters of 17.125 in. and 18.040 in., respectively. The thickness of the frame is 0.2 in. On the periphery of the frame, along the side, a groove 0.085 in. deep is machined. One side of the groove is 0.05 in. from the face of the frame. Along the groove, 144 radial holes 1 mm in diameter were drilled to support the wires. Thirty-five stainless steel wires of diameter 0.18 mm were attached both in vertical and horizontal directions passing through the holes. Each wire was held at its ends with

tiny studs made from solid core aluminum electrical wires. This method of attaching the wires was different from that used in the sinusoidal frames where the wires were soldered at each end. In the sinusoidal frames, to replace a particular wire the whole frame had to be heated uniformly which required much effort, while in this circular wire-mesh frame, each wire was independent and can be replaced easily by removing the studs at two ends. The wires were passed through the radial holes and then bent to form orthogonal mesh. The wires in the two perpendicular directions were not interwoven rather the horizontal set of wires passed smoothly over the vertical ones. The spacing between the wires is about 0.35 in., near the center of the frame, which is close to that used by Vetter [74]. The detailed drawing and photograph of the frame is shown in Figure 2.7 (a,b).

Two such frames were needed to sandwich the membrane forming the interface. These frames were in turn placed in an aluminum support. This aluminum support had internal diameter matching that of the shock tube and had a groove on its face for the wire-mesh frames. There were O-rings at the bottom of the groove and on the two faces of the aluminum support. On its periphery, there were holes to mount it on the studs protruding from the shock tube. Figure 2.8 (a) shows the aluminum support used for holding the wire-mesh frames and Figure 2.8 (b) shows the support holding the two wire-mesh frames (it does not show the sandwiched membrane). The circular aluminum support and the wire-mesh frames were marked to make sure that the frames were always loaded in the same way.

2.5 Interface formation

Interface formation between two gases has always been a major challenge to experimentalists studying RM instability. A common method is to use a very thin polymeric film. The thickness of the film is of the order of microns. In the multimode experiments on nominally flat interfaces the initial random perturbations are produced by the rupturing of the membrane. The different compounds used to make the film, film-curing time, film thickness and thickness distribution all have an affect on the

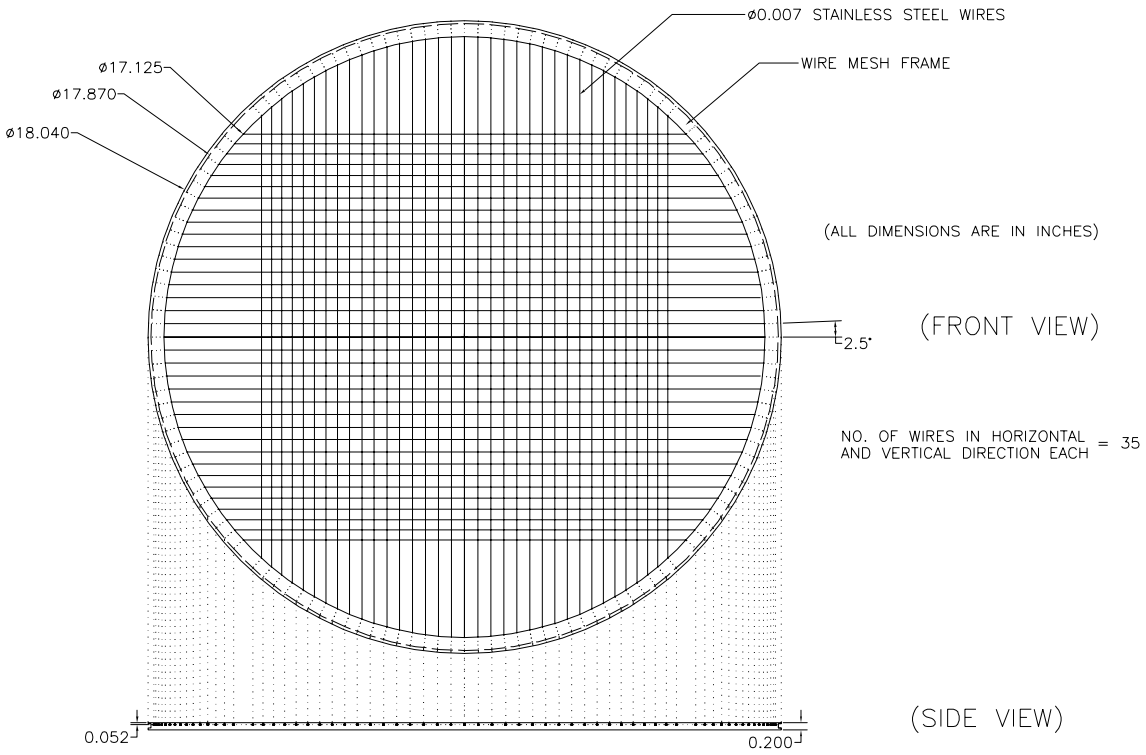

(a)

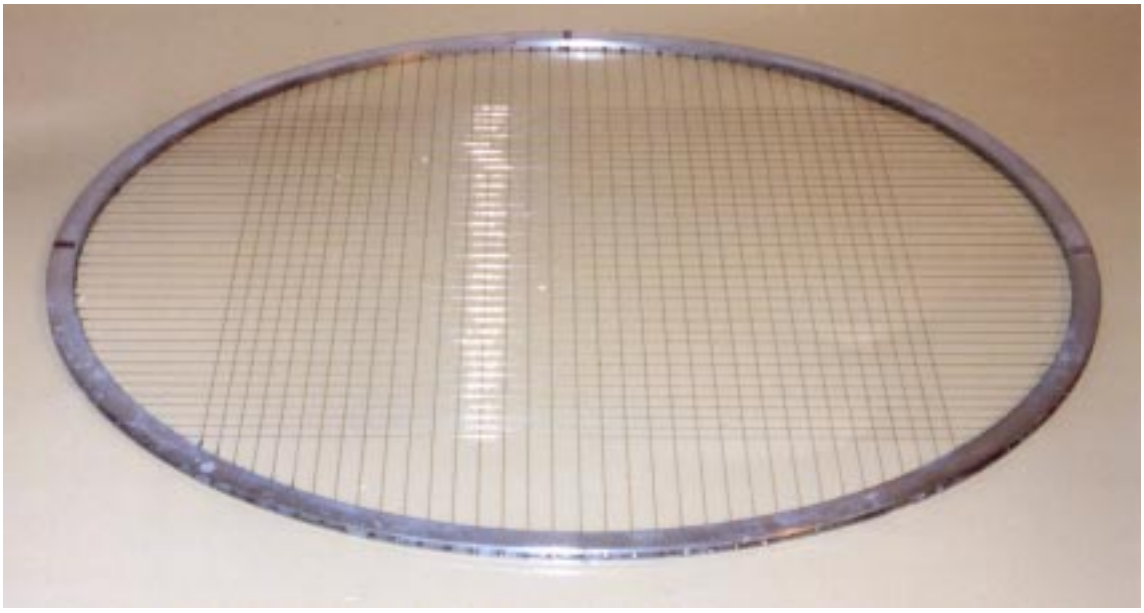

(b)

Figure 2.7: Wire-mesh frame. a) Detailed drawing. b) Photograph showing the frame and its edges.

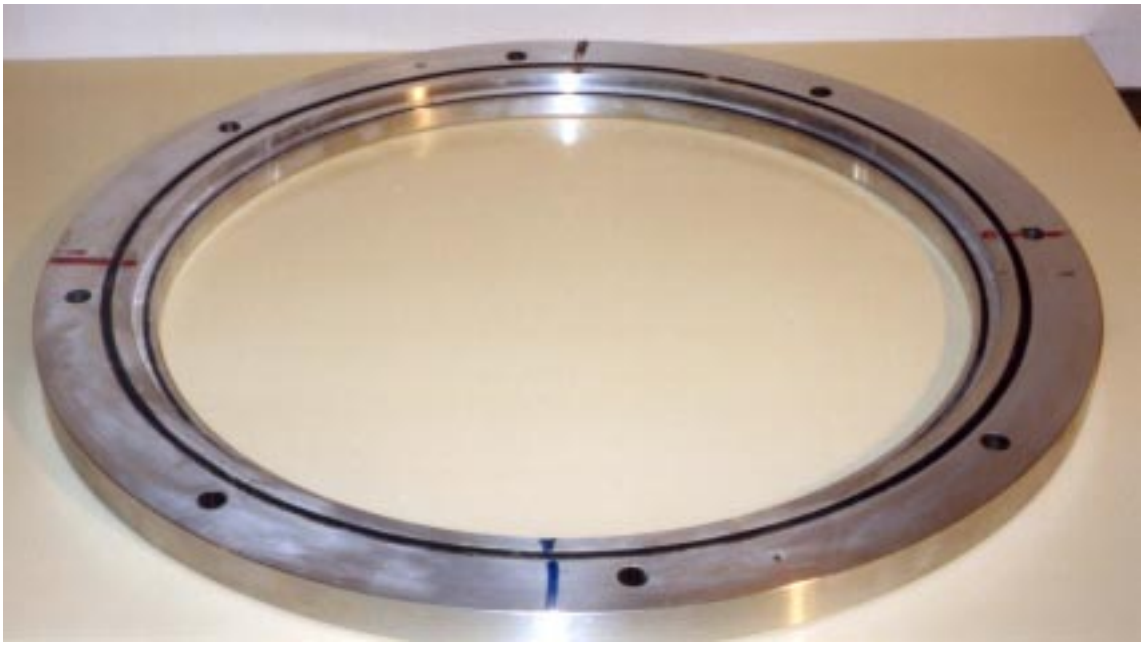

(a)

(b)

Figure 2.8: Circular support to hold the wire-mesh frame. a) Aluminum circular frame. b) Circular frame holding the wire-mesh frame.

mechanical properties of the film and thus its rupture characteristics [1, 33]. Zaytsev *et al.* [79] showed that the membrane could be pyrolized by strong shocks and the resulting gaseous compounds form a continuous interface between the two gases.

Recently, Erez *et al.* [28] did two different sets of experiments at a Mach number of 1.25 to study the affect of the membrane on the time evolution of the RM instability. The experiments were performed in an 8×8 cm cross section shock tube. Their first set of experiments consisted of a single-mode large-amplitude initial perturbation between two gas combinations (air/SF_6 and air/air) and two membrane thicknesses. The main conclusion of these experiments was that the membranes had a negligible effect on the evolution of the mixing zone, which evolves as predicted theoretically. In their second set of experiments, in which similar gas combinations and membrane thicknesses were used, the interface consisted of a nominally flat membrane between wire-mesh. The initial perturbations were random and were produced by the rupturing of the membrane. The main conclusions from this set of experiments were that the membrane has a significant affect on the initial growth, but when the amplitude becomes large and TMZ becomes fully nonlinear, then it has negligible affect. The results agree with full numerical simulations.

Experiments without membranes have also been performed. Brouillette [21] used a sliding plate that initially separates the two gases. The plate is retracted just before the shock wave is launched. The pulling action of the plate creates the initial perturbation. Another membrane-free technique was devised by Jones and Jacobs [35], who used a vertical shock tube and injected light gas from the top and heavy gas from the bottom. The two gases meet at the desired interface location. The initial perturbation is formed by oscillating the shock tube, forming gravity waves at the interface which serve as the perturbation. Both techniques, the sliding plate and gravity waves to form the interface, require a vertical shock tube.

The present experiments are performed in the GALCIT 17 in. shock tube. The shock tube is horizontal and the best method to form the interface is to use a polymeric membrane, also sometimes referred to as nitrocellulose membrane. The following

subsection describes the procedure of making this membrane.

2.5.1 Procedure of making the polymeric membrane

In order to make this polymeric membrane, first a special solution consisting of various chemicals is made. Table 2.2 describes the set of chemicals along with their quantity (given both by mass and volume) which were used to make the master solution.

Chemical	Quantity (gm)	Quantity (ml)
n-Butyl Acetate	60	69
iso-Butyl Alcohol	60	75
Ethyl Acetate	30	36
Methyl Ethyl Ketone	60	78
Toluene	15	18
Castor oil	18	
Nitrocellulose	90	

Table 2.2: Chemicals (and their quantity) used for making polymeric membrane

Nitrocellulose can be purchased from the Green Tree Chemical Company (the rest of the chemicals are readily available). The address of the company and the specifications of the nitrocellulose container obtained from them are as follows:

Green Tree Chemical Technologies, Inc.
50, South Minisinki Avenue, Suite 2.
Parlin, NJ 08859-1089
Ph. No.: (732)254-2938

LOT NUMBER:	NCOG8560
TYPE:	SS 1/4 SEC ISOPROPYL
STD. VISCOSITY:	5.4
Percent N_2:	11.3
Moisture, % :	4.1

In order to make the solution, the chemicals were poured into a large jar in the order they are listed in the table. The solution was allowed to mix for five minutes with a magnetic stirrer before each new ingredient was added. Nitrocellulose, being a powder, should be added in small quantities (5-10 grams) at a time. If added in

large amounts, it tends to form lumps which make the mixing process difficult. Once all the chemicals have been dissolved, the solution should be stirred continuously for at least 48 hours. When the master solution is ready, about 63 ml is mixed with approximately 3 gm of castor oil[1]. It is stirred for one day. This final mixture of castor oil and the master solution is used for making membranes and is called the membrane solution.

To make membranes, a water tank of size 60×36 in. and 4 in. deep was built. It was filled with water to about half of its depth. Wooden frames of sizes 13×13 in. and 19.25×19.25 in. were used to temporarily hold the membranes for the single-mode and multimode experiments, respectively. The membrane solution was poured slowly at one end of the water tank. The solution tends to spread on its own but should be helped by pulling it along the edges with your fingers. Once a large enough membrane is produced, it was allowed to dry, and the appropriate wooden frame with adhesive on its faces was gently placed on it. The extra portion of the membrane located outside the wooden frame was cut off. The frame was then gently lifted from the tank and the membrane was allowed to dry. A typical membrane on a 19.25×19.25 in. wooden frame is shown in Figure 2.9. The membrane is transparent and it is not immediately obvious from the figure if there is a membrane stretched on the frame. A small reflection from a patch at the bottom is the only evidence in this photograph. The membrane has a nonuniform thickness because the membrane solution does not spread uniformly on water. Various patches were taken from a sample membrane and thickness of each patch was measured by an Atomic Force Microscope [26]. The thickness of the membrane used in our experiments varied from 1.1 μm to 1.9 μm on a single frame. The average thickness of the membrane was 1.5 μm, which was the same as used by Vetter [74]. The average areal density of this membrane is about 5 gm/m^2.

[1]The castor oil acts as plasticizer and provides flexibility to the membranes. The amount described here worked for this set of experiments. If the membranes tend to break while drying or taking them out of the water tank, more castor oil should be added.

2.6 Test sections

For the present study, two types of test sections were used. Single-mode experiments were performed in a straight test section with square cross section and multimode experiments were performed in a conical test section. This section describes the basic geometry of these test sections.

2.6.1 Straight test section

The straight test section is made of two parts. Each part is 0.61 m long and is made with four aluminum plates 0.75 in. thick welded together. There are square flanges on both ends with O-rings on their faces. The two parts can be bolted together and to the shock tube (actually the flange of the cookie cutter) to form a sealed test section 1.22 m long. This configuration was used in the present experiments. The inside dimension of the test section cross section was 10.5×10.5 in. Each part of the test section had a pair of 6 in. diameter glass windows for schlieren flow visualization. The two windows of the pair were on the opposite side walls. The two parts of the test section can be rotated by 180 degrees to get four possible locations of windows for visualization. These four possible locations were at distances of 226, 429, 836 and 1039 mm downstream of the initial location of the interface. The two parts of the test section had pressure transducers, for triggering purposes, flush with the floor at the location of the windows.

The whole test section hangs from the rails fixed to the ceiling of the lab and can be moved on it. At the far end of the test section, perpendicular to the tunnel axis, there was another 6 in. diameter glass window similar to the ones on the side walls. It was used for last minute checks of the polymeric membrane before launching the shock wave. The valve for filling the test gas (SF_6 in this case) was attached to the floor of the test section. Since this study on straight test section was a part of the study conducted by Prasad *et al.* [59], only the window at 226 mm from the interface was utilized to add new data for Frames 2 and 3. Figure 2.10 shows the schematic and photograph of the straight test section.

2.6.2 Conical test section

The conical test section was used to study the affect of area convergence on RM instability. The initial interface in this case was nominally flat with random perturbations introduced by the rupture of the polymeric membrane. The cone used for making the test section was made of aluminum with wall thickness of about 0.27 in. The larger diameter end of the cone matches the internal diameter of the shock tube and the smaller diameter end had a diameter of 3.56 in. The half-angle of the cone was 10 degrees. The length of the cone was 38.11 in. In order to reduce the diameter of the small end, an extension was attached to the end of the cone. On the outside it looked cylindrical but inside it had a conical bore. The diameter at the end of the extension was 0.75 in. Figure 2.11 shows this extension.

The extension had an O-ring on the face of its flange to prevent any leaks when it was bolted on to the flange at the smaller diameter end of the cone. It also had a hole on its side for monitoring pressure in the conical test section. At the end of the extension, a valve could be attached to fill the test section. The valve used was the same valve as the one used in straight test section.

The total length of the conical test section with the end piece was 46.61 in. In order to do the flow visualization, some windows had to be machined on the conical surface of the cone. Due to the curvature of the surface and its continuous variation (due to conical shape), the design of the windows was not straightforward. The location of the windows along the axis of the conical test section was decided from the fact that, at the incident Mach number of present experiments ($M_s = 1.55$), the interface comes to a stop at a distance of 22 in. from the initial interface location. This result was arrived at by preliminary numerical simulations.

For the initial experiments, three pairs of circular windows were installed on the surface of the cone. The centers of these three pairs of windows are at distances of 5 in., 13 in., and 21 in. along the cone axis from the entrance of the cone. The two windows in a pair are 180 degrees apart along the circumference so that the light beam can pass through for schlieren flow visualization. Figure 2.12 shows a photograph of

the cone with three pairs of circular windows and the extension with the gas filling valve.

The windows on the conical surface were placed normal to the surface with a clear aperture of 2.2 in. This diameter was optimum with regard to the wall thickness of the cone. A small step was necessary to hold the optical glass (BK-7) window in place. For this, a circular hole of 2.4 in. diameter was drilled on top of the clear aperture hole of 2.2 in. diameter. This was not a through hole and hence left a step for a 0.5 in. thick glass piece to sit on. This step was crescent-shaped due to the fact that the principal radius was continuously changing because of conical geometry. As a result, the thickness of this crescent-shaped step is maximum at the centers and goes to zero at its ends. O-rings and rubber gaskets were installed at appropriate places to seal the window to the cone. When the glass sits on the step, it covers up some area of the cone and some area is exposed. The step height is designed to make these areas the same, at least in the principal plane at the center of the window, to maintain continuity. Figure 2.13 (a) shows this area equalization concept and the details of the window section at 13 in. from the interface location. Figure 2.13 (b) shows the view of the window normal to the surface, the two crescent-shaped steps at opposite ends for holding the glass piece are visible. There were four studs on the sides for the flange to hold the glass. The holes for the studs on the cone wall were blind to prevent any leaks through them. A similar design was used at the other two locations.

In preliminary attempts to capture the interface in the three axial locations of the cone, it turned out that the turbulent mixing zone at the interface grew larger than the window size in the second and third locations. First location refers to the window that is closest to the initial interface location at a distance of 5 in. from it, the second and third locations refer to the window centers at 13 in. and 21 in. In order to overcome this difficulty, two pairs of rectangular windows were machined on the surface at the second and third locations. The machining was done normal to the cone surface. Each pair of the rectangular windows were at 45 degrees on either side of the circular windows. The clear aperture of the rectangular windows was an

8×2.2 in. rectangle. The cross section at the center of the window in the principal plane was the same as for circular windows at the same location. The length of these rectangular windows is such that along the axial direction the third rectangular window begins where the second one ends. They are not on the same generator of the cone, hence the cone has to be rotated by 45 degrees in order to switch from second to the third window for flow visualization. Figures 2.14 (a,b) show the cone with the rectangular window at $x = 13$ in. and the normal view showing the step that supports the glass. The flange holding the glass was attached to the cone in way similar to the circular window case. A schematic of the conical test section with circular or rectangular windows attached to the shock tube is shown in Figures 2.15 (a,b).

2.7 Pressure measurements

During each shot of the shock tube, the Mach number is determined by the intervals between the pressure signals from two high-pressure transducers (Model 112A21 from PCB Piezotronics) in the driven section. The transducers are mounted 1.823 m and 5.131 m from the open end of the tube and have sensitivity of 50 mV/psi. The passage of the shock waves is registered by these gauges. Their output is recorded using Computerscope hardware and software from RC Electronics installed on a computer, sampling at a frequency of 125 kHz. In the case of straight test section, two additional pressure transducers were mounted flush with the floor wall at the window locations. The transducer at the location of the window used for visualization is used to trigger the spark gap. In the case of the conical test section, there is no transducer on the cone wall and hence the transducer used for triggering the spark gap is the one that is closest to the initial interface location, i.e., at a distance of 1.823 m from the end of the shock tube. The data aquisition system was triggered in both cases by the transducer located at the extreme upstream location, i.e., at a distance of 5.131 m from the end of the shock tube.

The output of the transducer also goes to a delay generator which sends an appropriately delayed signal to the power supply of the spark gap which is used for

illumination. The timing was determined correctly by a few trial runs.

2.8 Description of gases

The gases used in the driver and the driven side of the shock tube are helium and air, respectively, in all the experiments. The test section was filled with SF_6 for most of the experiments, while a few shots, in the conical test section, were done with helium. The choice of the test gases was governed by both safety and convenience. The relevant properties of these gases is given in Table 2.3.

Property	Air	SF_6	Helium
Molecular mass (kg/kmol)	29.04	146.07	4.00
Density, ρ (kg/m^3)	1.18	5.97	0.16
Atwood ratio with air, A	0	0.67	- 0.76
Specific heat ratio, γ	1.40	1.09	1.667
Kinematic viscosity, ν (10^{-6} m^2/s)	15.7	2.47	117.3
Prandtl number, Pr	0.71	0.90	0.70
Diffusion coefficient in air, D (cm^2/s)	0.204	0.097	0.711
Index of refraction (sodium D line)	1.000264	1.000717	1.000033

Table 2.3: Gas Properties at 25^o C, 1 atm.

2.9 Flow visualization technique

Flow visualization to study the growth of RM instability was done both by schlieren and laser-induced scattering (LIS) from a laser sheet. In the single-mode experiments in the straight test section, only schlieren technique was used, while in the conical test section both schlieren and laser sheet techniques were used. The schlieren system

used a spark gap light source for illumination. Figure 2.16 (a,b) shows the schematic of the schlieren setup for both the straight and conical test sections.

The light source was a spark gap with a 10 kV, 0.1 μF capacitor, which discharges between two pointed electrodes. A spherical mirror with 9 in. clear aperture and focal length of about 52 in. collimates the light from the spark gap which is placed at its focus. To produce the schlieren effect, another spherical mirror focuses the light onto the knife edge mounted on a two-dimensional positioner. Two plane mirrors are used to fold the optical path. The image is recorded by a 35 mm Nikon FM 2 camera with a 50 mm Nikkor lens using Kodak TMax 400 ASA black and white film. During the experiment the camera is operated with the shutter open in a darkened room. A pressure transducer provides a signal to a delay generator which in turn sends a trigger signal to the power supply of the spark gap to make it discharge and illuminate the test section for about a micro-second.

For the LIS experiment, an Nd-Yag pulsed laser (Model: Tempest-Gemini PIV from New Wave Research, Inc.) was used to produce a very thin (1 mm) laser sheet. The main difficulty in this experiment was seeding the test section. Olive oil mist produced from a fog generator designed by DLR was used for this purpose. Since the mist can only be produced by passing high-pressure gas in the fog generator, it was not possible to directly pass the test gas through it because of the presence of the membrane. The very fragile nature of the polymeric membrane requires filling the test section very slowly at low pressures. To overcome this difficulty, a buffer tank was built, the test gas with mist was stored in it, and then slowly bled into the test section. Unfortunately, the ball valve which fills the test section could only be opened a small amount and the filling time was very long. As a result, the mist did not pass through the valve and there was virtually no mist in the test section. This problem was overcome by mounting an exhaust fan inside the buffer tank. The buffer tank was now filled with mist and test gas to the same pressure as the test section and the valve was fully opened. Since the flow circuit was closed, the gas and the mist in the buffer tank and the gas in the test section were eventually fully mixed by the exhaust fan. To close the circuit, one of the circular windows at $x = 5$ in. was converted into

a port for the tubing. This technique was satisfactory in seeding the test section. Figure 2.17 (a,b) shows the schematic of this visualization technique.

Note that the laser sheet was shining at an angle into the last rectangular window and visualization was done via the rectangular window at the second location. This arrangement was chosen due to the location of the windows and from the desire to view perpendicular to the laser sheet. Figure 2.17 (b) shows that the CCD camera was looking at right angles to the sheet. The timing in the delay generator was adjusted so as to synchronize the laser firing and the interface presence in the second window location. The data from the CCD camera was collected by Video Savant frame grabber installed on a computer.

2.10 Run operation

To prepare the shock tube and test section for a shot, the first step was to load the aluminum (Al-1100) diaphragm of 0.01 in. thickness into the diaphragm section of the shock tube. The polymeric membrane was then transferred from the wooden frame onto the circular or sinusoidal wire-mesh frames by cutting it with a razor blade. It was sometimes useful to apply talcum powder to the frames to prevent the membrane from getting stuck and tearing in the process of loading. The frame and membrane assembly is loaded on the end of the shock tube and then the test section is bolted onto it. The whole shock tube, including the test section, is now pumped down to vacuum. The static pressure difference between the test section and driven section is continuously monitored using a differential pressure gauge to make sure the membrane is not broken or torn in the process. At the end of the pumping down process, the valve connecting the test section and shock tube is closed. The test gas in the test section and air in the driven section, are very slowly introduced, making sure the pressure difference on both sides is within 10 mm Hg. This process is the most difficult part of the experiment due to the fragile nature of the membrane. The pressure at the end of filling was 23 kPa. The driver side was then filled with Helium until the diaphragm burst. The shock Mach number was 1.55 with a 0.01 in. thick

aluminum diaphragm between the driven and the driver section of the shock tube. A diaphragm thickness of 0.006 in. gave a Mach number of 1.39. The uncertainty in the Mach number measurements was ± 0.01 determined from transducer size and response. Few experiments in the conical test section were done at this lower Mach number. The delay settings in the delay generator were appropriately adjusted for flow visualization.

Figures 2.18, 2.19, and 2.20 show photographs of the conical test section setup on the shock tube along with the laser and computer system.

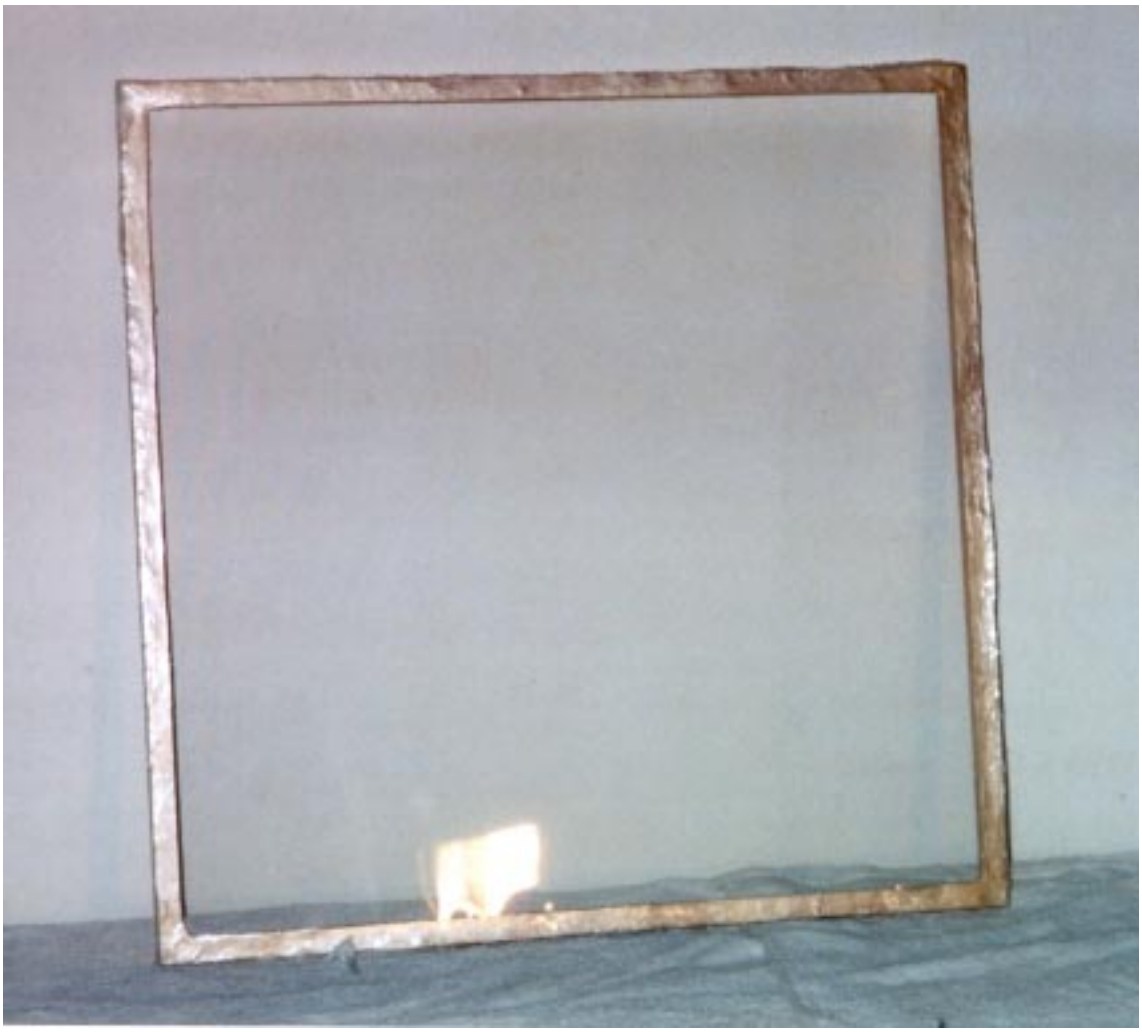

Figure 2.9: Photograph showing the nitrocellulose membrane stretched on a wooden frame.

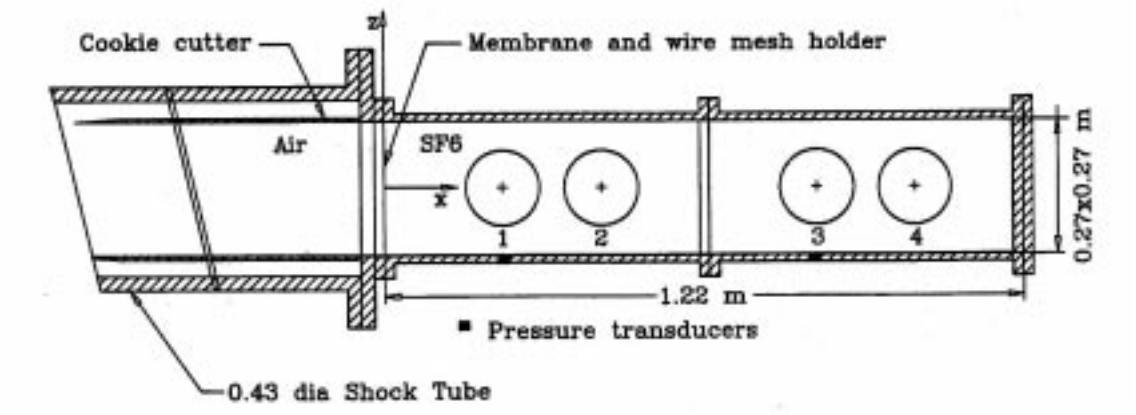

(a)

(b)

Figure 2.10: Straight test section. a) Schematic drawing showing observation window placement (Reproduced from Prasad *et al.* [59]). b) Photograph showing the test section attached to the shock tube.

Figure 2.11: Photograph showing the extension of the cone.

Figure 2.12: Photograph showing the cone with circular window apertures and extension installed.

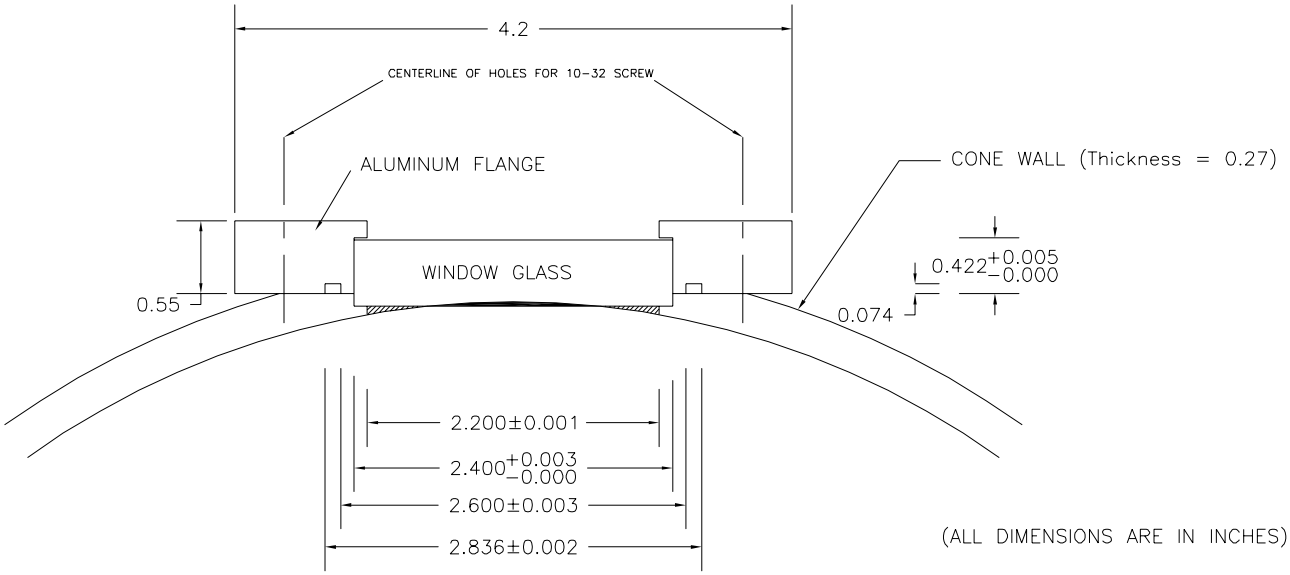

(a)

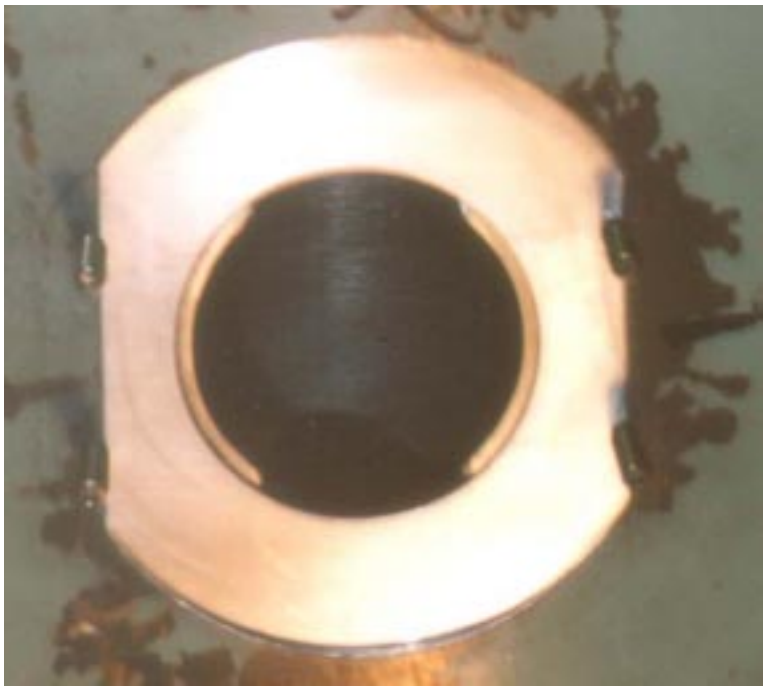

(b)

Figure 2.13: Details of the window design at $x = 13$ in. a) Detailed drawing of the window in the principal plane, the two hatched areas in solid and slanted lines are equal. b) Photograph of the normal view of the window shown in (a), crescent-shaped supports for the glass are visible.

(a)

(b)

Figure 2.14: Rectangular window placement at $x = 13$ in. a) Photograph showing the opening for the rectangular window on the cone. b) View normal to the cone surface of the rectangular window opening.

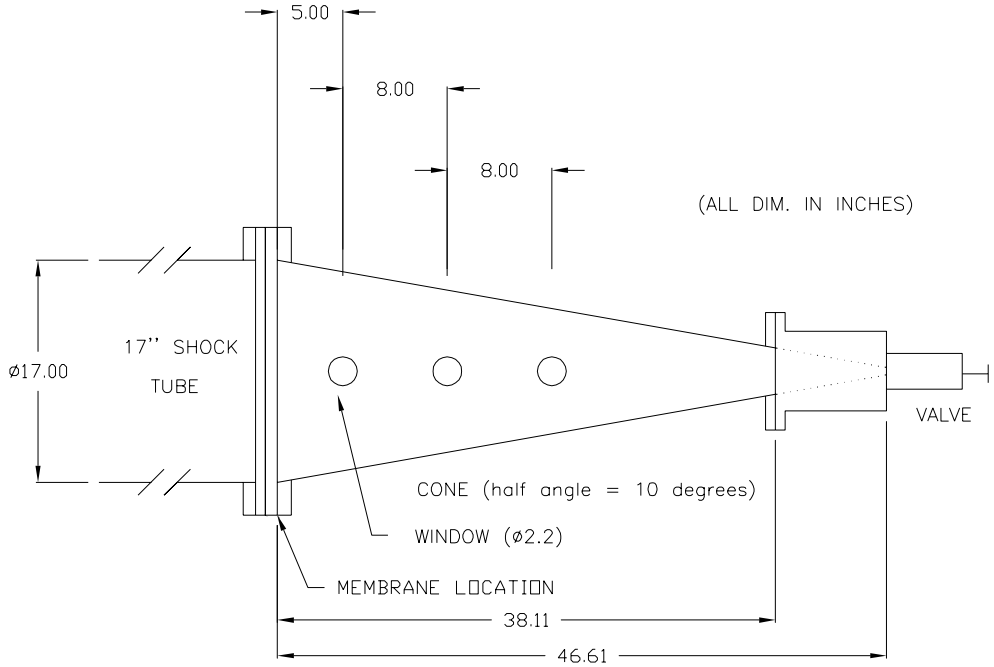

(a)

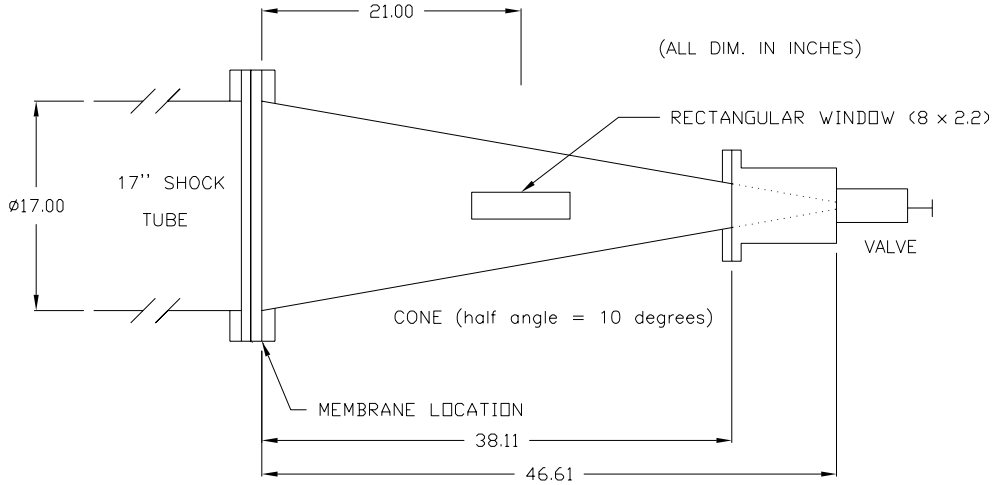

(b)

Figure 2.15: Schematic of the conical test section attached to shock tube. a) Test section showing the three circular windows. b) Test section showing the rectangular window at $x = 21$ in.

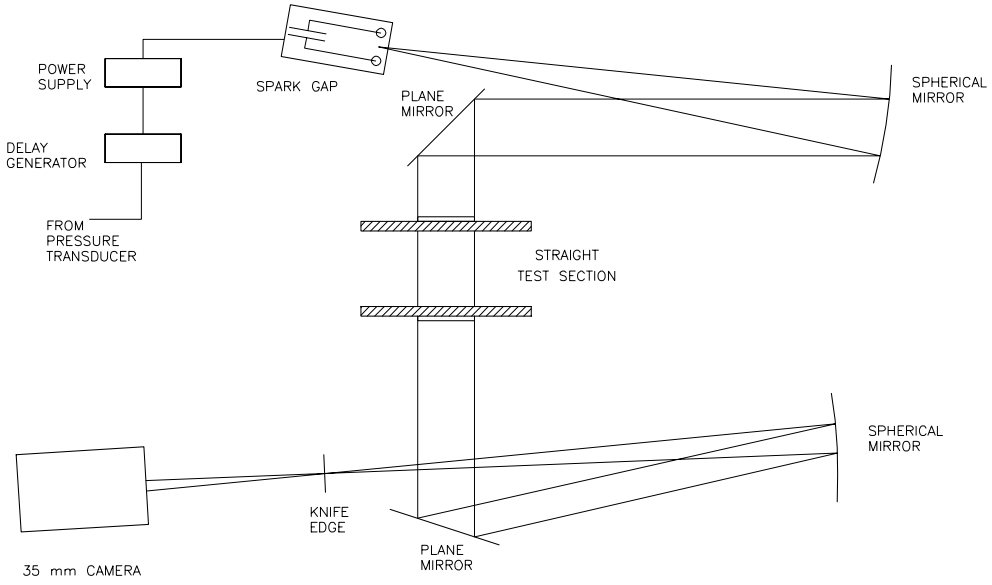

(a)

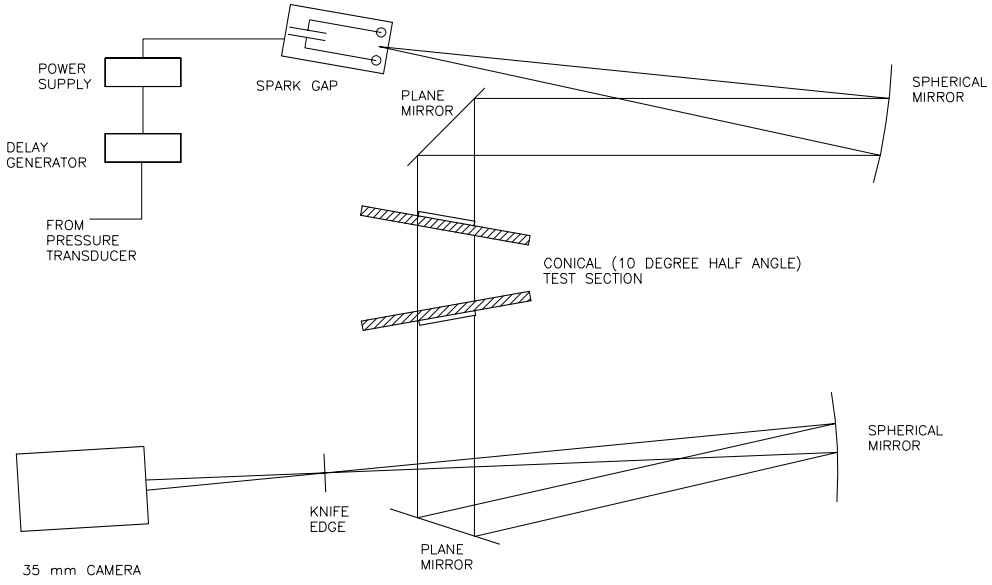

(b)

Figure 2.16: Schematic of the schlieren setup. a) Straight test section. b) Conical test section.

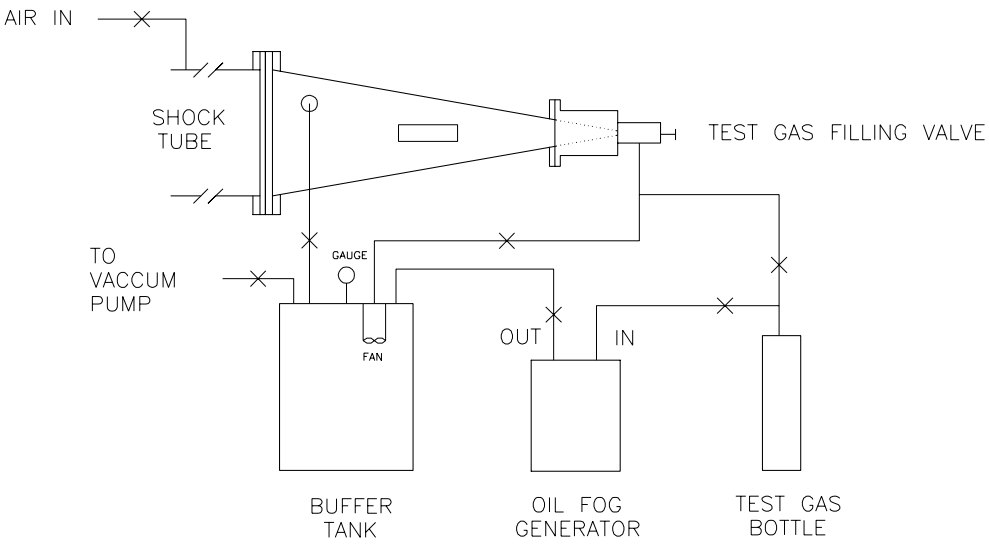

(a)

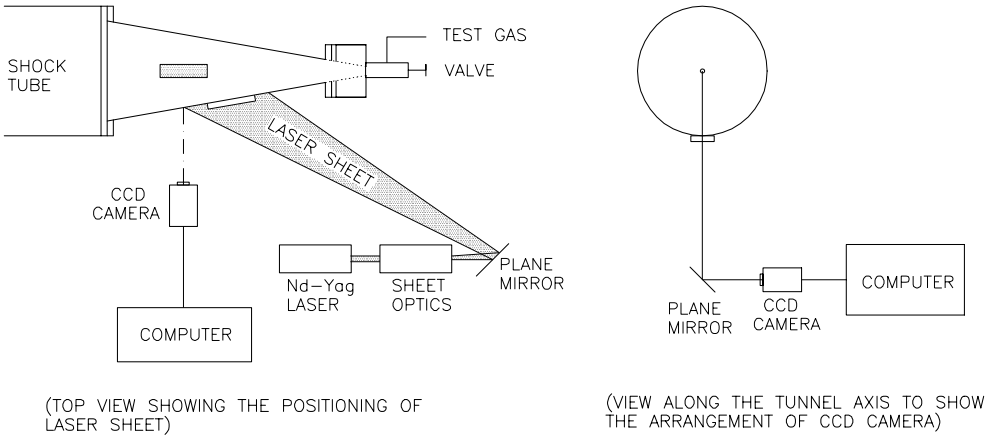

(b)

Figure 2.17: Schematic of the laser-induced scattering setup. a) Seeding technique. b) Laser sheet and camera locations.

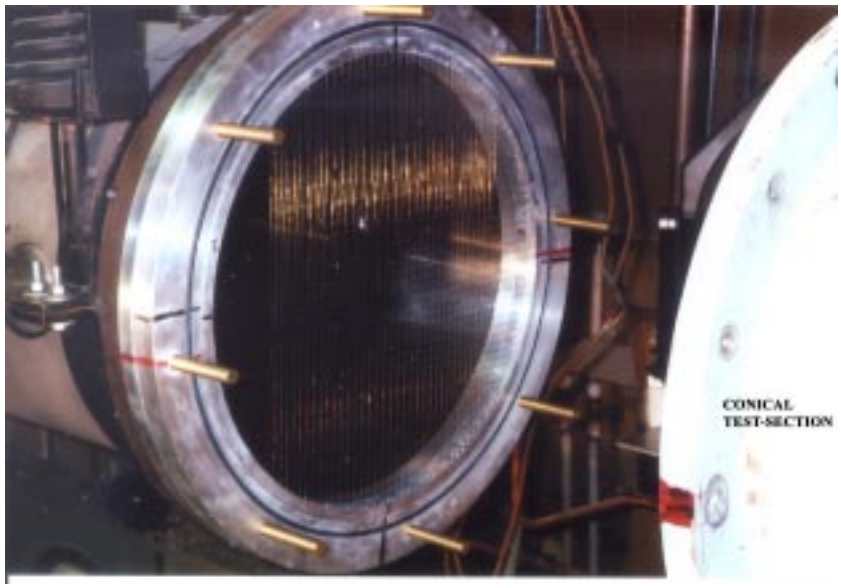

(a)

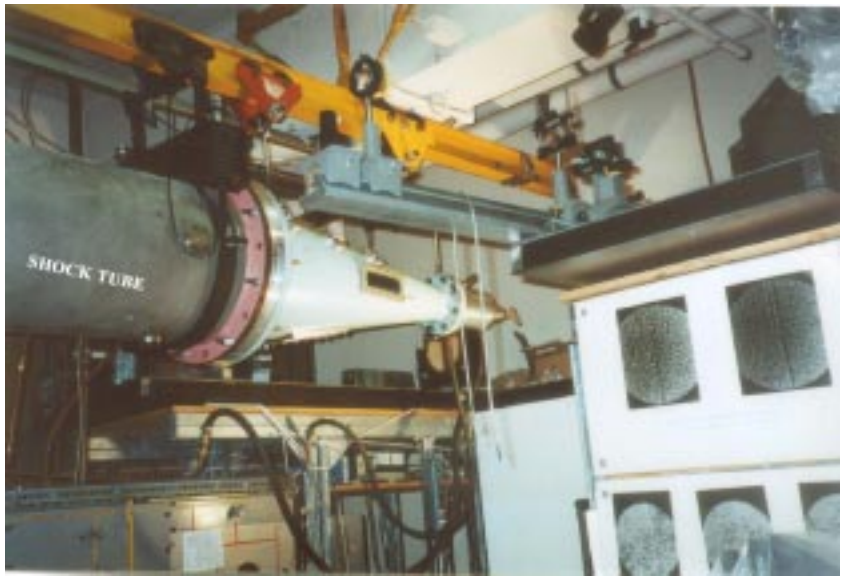

(b)

Figure 2.18: Photographs of the experimental setup of the conical test section. a) Wire-mesh frame on the shock tube. b) Test section with schlieren setup for third rectangular window location.

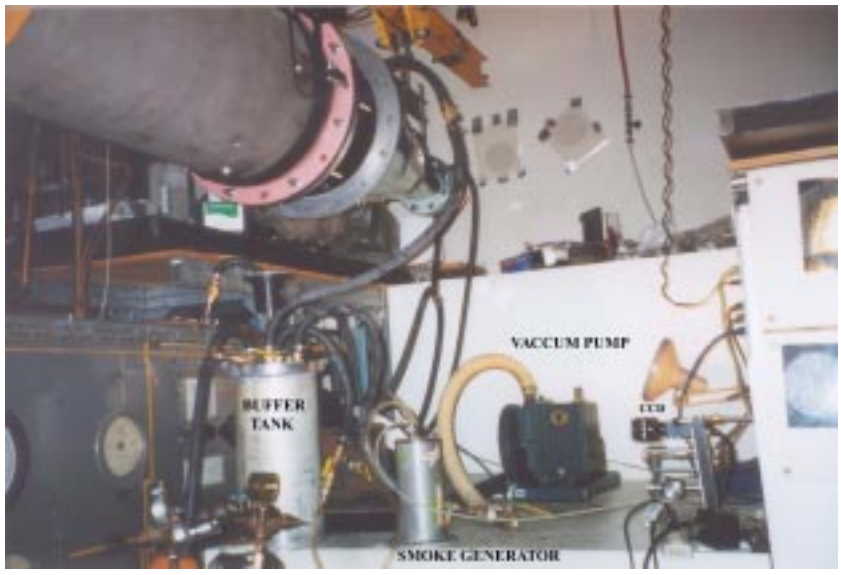

(a)

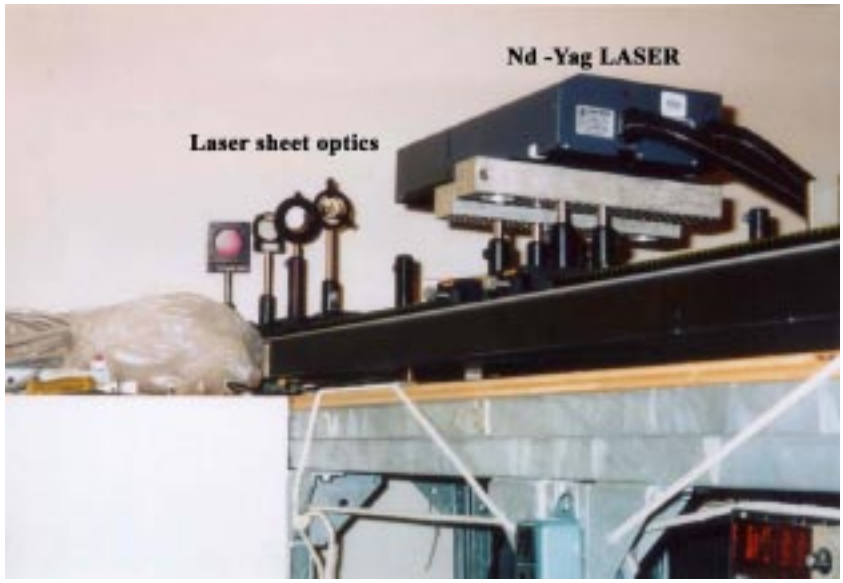

(b)

Figure 2.19: Photographs of the experimental setup of the conical test section. a) Setup showing the various components for olive oil mist injection, tubings and CCD camera. b) Laser head and the sheet optics.

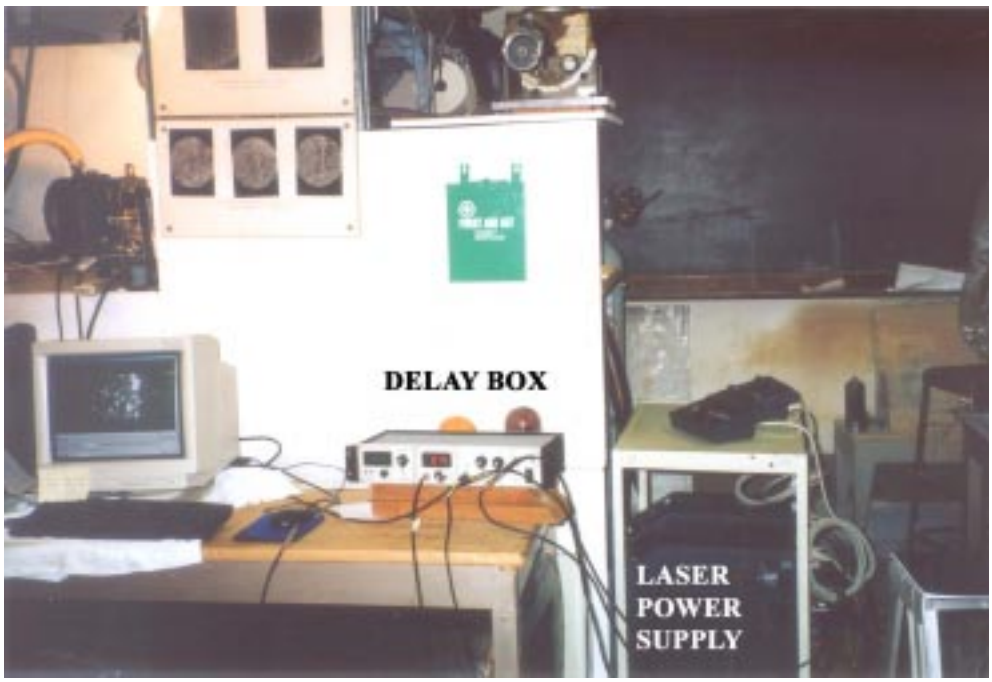

Figure 2.20: Photograph of the experimental setup of the conical test section showing the computer, the delay box, and the laser power supply.

Chapter 3 Single-Mode Perturbations

Experimental results on single-mode perturbation experiments in the straight test section are presented in this chapter. Only the light-heavy configuration was studied. The interface was formed with a polymeric membrane between air and SF_6, the latter being in the test section. The shock Mach number in the experiments was about 1.55. Helium was used as the driver gas and air as the driven gas in the shock tube. For the present run conditions, the expansion wave from the driver section overtook the incident shock in the test section, so behind the shock the pressure decreased at a measured rate of 1.5 kPa/ms. The impulsive acceleration by the shock was followed by a small constant deceleration, superimposing a small stabilizing RT effect on the RM growth. This effect was also present in Vetter's [74] experiments. In view of its small amplitude, it is ignored in the presentation of the results, but it could be accounted for, in numerical simulations. This work on single-mode perturbations was part of the study done by Prasad *et al.* [59]. In that study four different wavelength and amplitude combinations of interfaces were studied. The visualization was done by the schlieren technique. High-speed photography was also used. In the present study, only interface Frame 2 and Frame 3 (the description of these Frames is given in Chapter 2) were used to add spark schlieren visualization data to the previous data. *My only contribution in this part of the study was the addition of flow visualization data on Frames 2 and 3.* The following section describes the results on Frames 2 and 3 along with the relevant results from the study of Prasad *et al.* [59]. In this chapter, the interface thickness δ is *half* of the total interface thickness, which was defined earlier as the thickness from the front to the rear of the interface.

3.1 Results

Figures 3.1 and 3.2 show the spark schlieren photographs from experiments with Frame 2 and Frame 3. In theses pictures, the air is on the left and sulfur hexaflouride (SF_6) is on the right. Time zero is taken to be the instant when the shock wave reaches the interface. The photographs in Figures 3.1 and 3.2 show the status of the mixing zone at $t = 1.51$ ms and 1.52 ms for the two Frames.

The interface appears dark due to the combination of the schlieren effect and the scattering of light from the field of view by membrane fragments. The interface in both pictures is clearly in the nonlinear regime, with the appearance of bubbles and spikes. The bubbles of air are "rising" into the heavy SF_6 on the right and the spikes of heavy gas SF_6 are "falling" into the lighter gas air. At late times the bubbles are observed to flatten. The cause of this behavior is not known, but it may be due to the small stabilizing deceleration described above. In the study of Prasad *et al.* [59], two other interface geometries were studied whose details are given in Table 3.1 along with those of Frame 2 and Frame 3.

Frame	$\lambda_\circ$ (mm)	$k_\circ$ (mm^{-1})	$\eta_\circ$ (mm)	$k_\circ\eta_\circ$	Symbol used
1	59.3	0.106	2.97	0.31	$\triangle$
4	29.6	0.212	1.46	0.31	$\circ$
2	59.3	0.106	5.91	0.62	$\square$
3	106.7	0.059	5.33	0.31	$\Diamond$

Table 3.1: Experimental conditions. air/SF_6, $M_s = 1.55$, $U_i = 174$ m/s, $A = 0.67$, $A' = 0.74$.

A dimensional plot of the results of measurements of the *half* thickness $\delta = \eta - \eta_\circ$ at different interface positions x, for all of the experiments reported here and in Prasad *et al.* [59] is given in Figure 3.3, where x is proportional to the time t after shock excitation, $x = U_i t$, U_i being the velocity induced by the incident shock. The interface thickness was measured visually from the photographs as shown in Figure 3.1. The front of the interface in the pictures is well defined, but the rear of the interface is taken to be the place where the mixing, as visible from the photographs, has almost stopped. This way of measuring interface thickness is widely used by the researchers

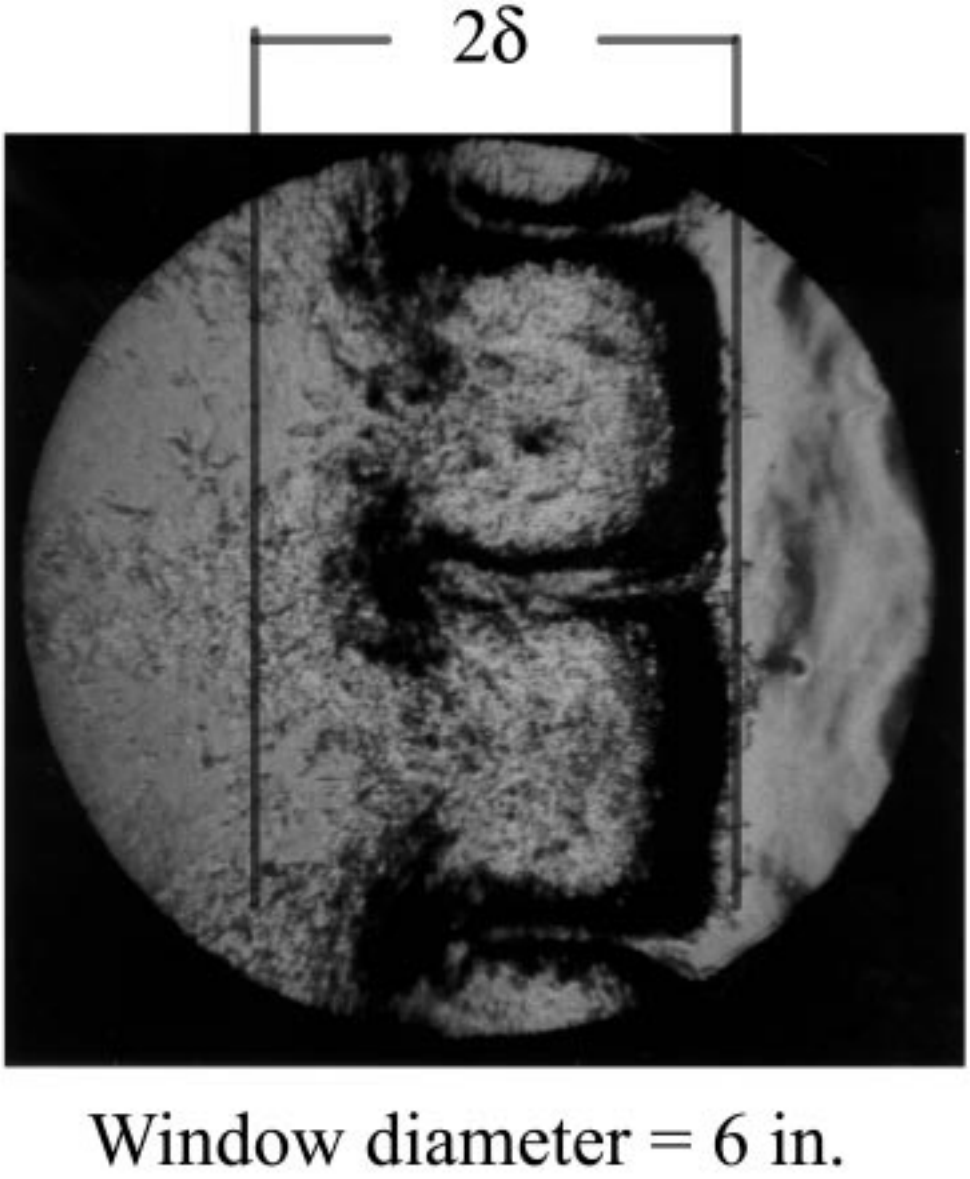

Figure 3.1: Schlieren image of Frame 2; $\lambda_\circ = 59.1$ mm, $\eta_\circ = 5.91$ mm, $k_\circ\eta_\circ = 0.62$, $x = 231$ mm ($t = 1.51$ ms), $M_s = 1.58$, Run SK23.

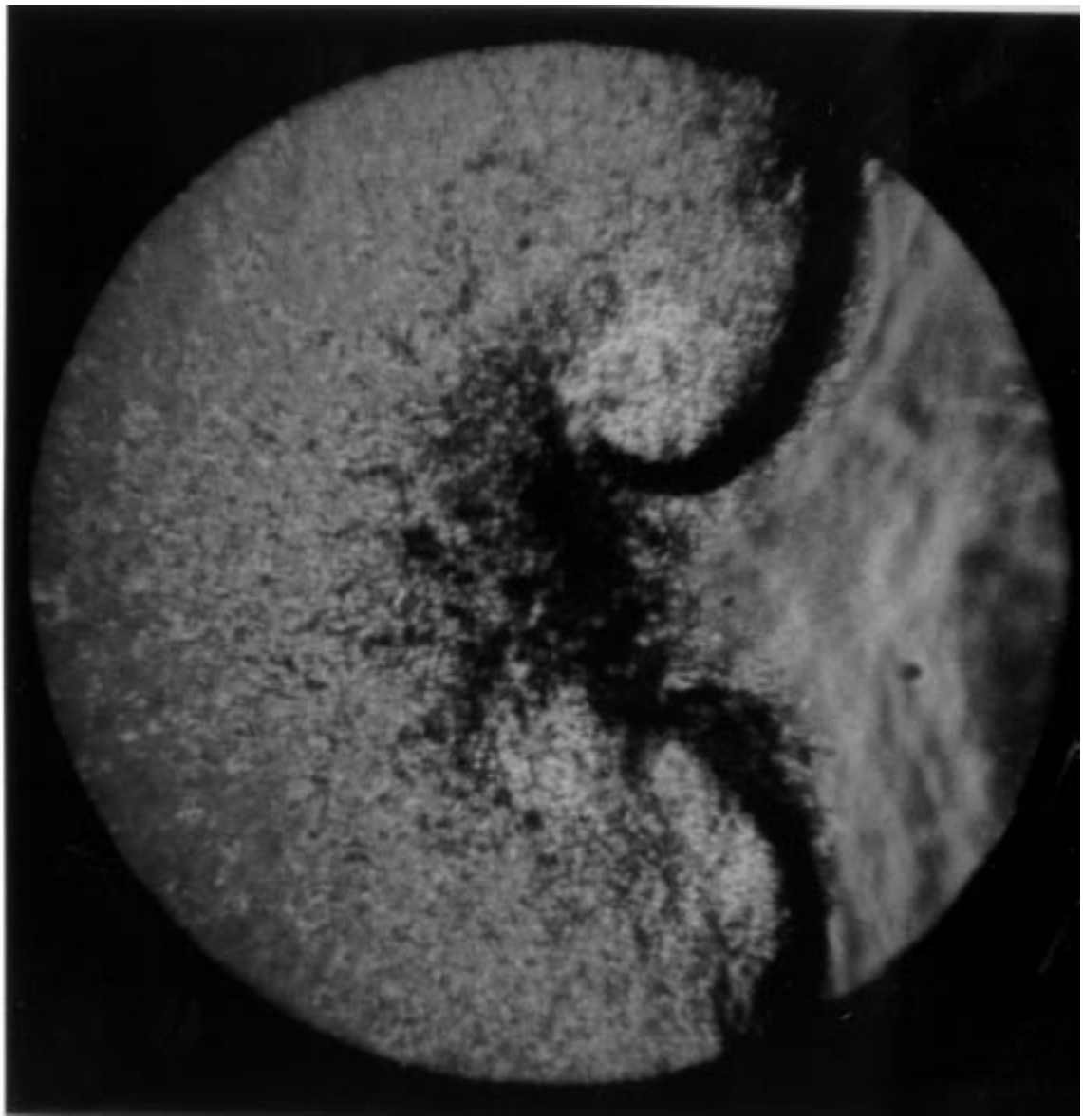

Figure 3.2: Schlieren image of Frame 3; $\lambda_\circ = 106.67$ mm, $\eta_\circ = 5.33$ mm, $k_\circ\eta_\circ = 0.31$, $x = 233$ mm ($t = 1.52$ ms), $M_s = 1.56$, Run SK24.

in this area [47, 61, 21, 22, 19, 23, 63, 74] and the measured thickness is called "visual-thickness" in the literature. A growth trend of the interface is evident in Figure 3.3; the smallest initial amplitudes have slightly smaller thickness, and the largest wavelength is the thickest.

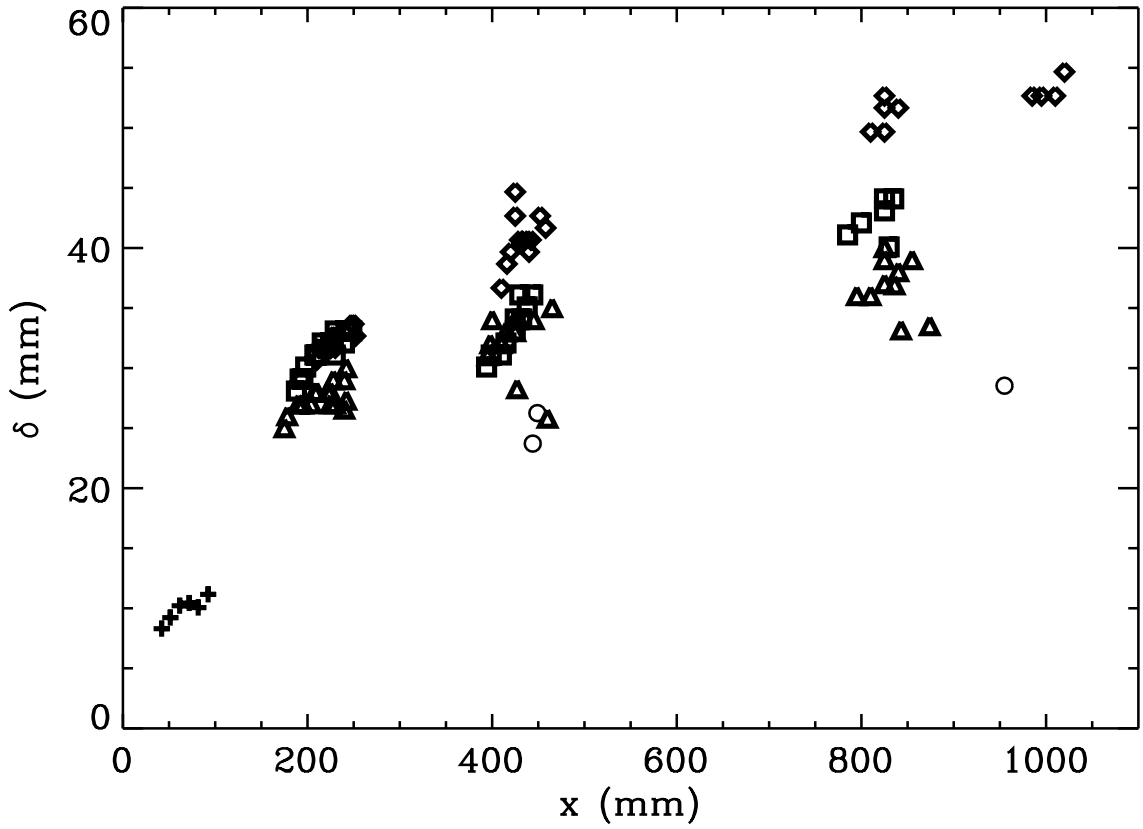

Figure 3.3: Plot of TMZ thickness vs. position of the interface for different wavelengths and initial amplitudes. Symbols defined in Table 3.1. Smallest initial amplitudes (∘ and △) show the smallest growth, while the largest wavelength (◇) grows the fastest. +, late time data of Sadot *et al.* [63] for $\lambda_\circ = 16$ mm.

A study was made to determine the power law and combination of parameters which optimally reduces the scatter of the data, and thereby minimizes the apparent dependence on initial conditions. It was found that the scatter in the data can be significantly reduced by dimensional scaling

$$\delta = 2.43\,(\lambda_\circ x)^{0.26}\,, \tag{3.1}$$

where all lengths are expressed in mm. The result is shown in Figure 3.4.

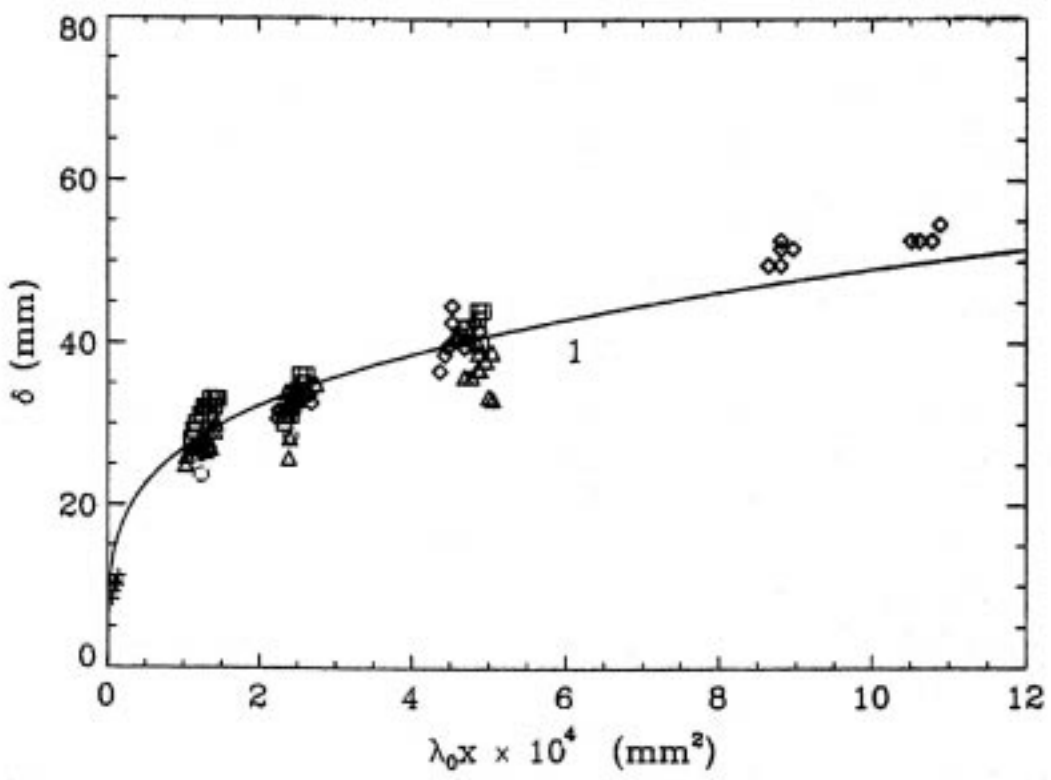

Figure 3.4: Correlation which yields minimum scatter of data about a power law fit. Symbols listed in Table 3.1. 1, $\delta = 2.43(\lambda_\circ x)^{0.26}$; δ, $\lambda_\circ$ and x in mm. +, late time data of Sadot *et al.* [63] for $\lambda_\circ = 16$ mm.

Prasad *et al.* [59] also did a curve fit to all the four interface data (which includes the present data) in non-dimensional coordinates, $k_\circ\delta$ and $k_\circ x$ to obtain a composite least squares fit to all of the data ($k_\circ = 2\pi/\lambda_\circ$),

$$k_\circ\delta = 0.96\,(k_\circ x)^{0.33}\,, \tag{3.2}$$

Measurements of the amplitude of single-scale perturbation on an interface between air and SF_6 accelerated by an $M_s = 1.55$ shock wave show that at late times the growth rate decreases rapidly with time,

$$d\delta/dt \propto t^{-p}, \tag{3.3}$$

where $0.67 \lesssim p \lesssim 0.74$. The scaling results do not give any information about the de-

pendence on shock strength and Atwood number, because only one value of each was used in these experiments. The observed decreasing growth rate with increasing time is accompanied by flattening of the bubbles on the non-linearly deformed interface.

Equation 3.1 agrees (to well within the experimental error) with the power law given by the Saffman invariant in the Huang-Leonard similarity law, Equation 1.22. This suggests that the invariance of the second moment of the velocity correlation proposed by Saffman [64] applies to late time RM mixing. At the latest time in the experiments the Reynold's number (Equation 1.20) based on the mean of the viscosities of air and SF_6 is about 15000, so the Reynold's number based on the Taylor microscale λ_t is about $\mathrm{Re}_{\lambda_t} \sim 100$–$300$ which is the range of validity of Huang-Leonard Equation 1.20.

In the present experiments, the late time growth rate, $d\delta/dt$, is probably less (*i.e.,* large p (Equation 3.3) or small m (Equation 1.15)) as compared to RM instability of an ideal, discontinuous membraneless sinusoidal interface because of the following: *i)* the small stabilizing RT deceleration that follows the impulsive RM acceleration in the shock tube, *ii)* damping effects of membrane fragments, and *iii)* possible enhanced growth at early times. Two possible mechanisms that can induce enhanced growth at early times are the small-scale turbulence initially deposited at the interface by the supporting wire mesh and the affect of small-scale perturbations on the interface due to membrane imperfections which grow more rapidly than large scales, according to Richtmyer's linear theory. Near the center of the shock tube, the membrane does not initially have a smooth sinusoidal shape, but is stretched in straight line segments across the wires resulting in sharp corners (Figure 2.6). These sharp corners can also induce small-scale motions. On the other hand, the sink effect of the unsteady boundary layers in shock tubes (which result in slower growth rate [22]) is avoided here due to the larger size of the shock tube. The conclusion that can be drawn from this study is that these experiments give a lower bound to the power m (Equation 1.15) with which the thickness of the RM interfaces grows at large times.

Chapter 4 Multimode Perturbations in a Conical Geometry

The present chapter reports the experimental results of the RM instability growth of multimode initial perturbations in a conical geometry. As explained in Chapter 1, the study of RM instability in a conical geometry is relevant to ICF experiments with piecewise planar shocks imploding in a sphere. The test section is a cone of 10^o half-angle with windows for flow visualization at three axial locations as described in Chapter 2. The investigation of the instability is done at late times when the mixing zone has become fully turbulent. The most important and obvious property of the TMZ is its thickness, which is measured in the present investigation with the spark schlieren technique. There are other interesting features of the TMZ such as scale sizes and their evolution with time, spectrum of turbulent energy, etc. These questions are not addressed in detail in the present investigation though an attempt is made to determine the dominant scale size by image processing of the schlieren photographs. The experiments are performed at an incident Mach number of 1.55 and 1.39 in light-heavy configuration with air as light gas and SF_6 as heavy gas in the test section. Some laser-induced scattering experiments are also performed in the heavy-light configuration with air/He as the gas combination.

Vetter [74] did experiments in the same shock tube and at about the same Mach number to study the evolution of TMZ with no area convergence. The primary aim of the present investigation is to see the affect of conical convergence on TMZ growth. The results are compared with Vetter's data for similar experimental conditions. Numerical simulations on AMRITA [60] are also performed to study the evolution of TMZ. Laser-induced scattering is also used to probe in detail the mixing zone in the air/He case. The large size of the shock tube and test section helps to minimize the shock-wave/boundary-layer interaction affects, as pointed out by Vetter [74].

4.1 Results

The flow physics of the present problem in a conical geometry, as compared to the one in the straight test section case, is further complicated by the diffraction of the shock wave as it enters the cone. The Mach number and cone angle of the present conditions ensure a Mach reflection at the cone wall. The reflected shock initially interacts strongly with the interface, producing a change in its overall geometry. The dynamics of the interface mixing is further complicated by the subsequent interaction with various reflected waves. Diffraction of the shock wave in the 10° half-angle cone was investigated in detail in the same shock tube by Setchell [66]. The shock wave evolution in the cone is shown schematically in Figure 4.1.

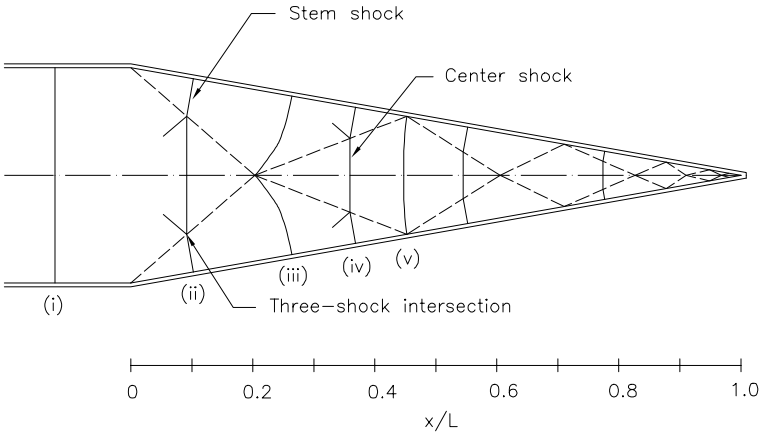

Figure 4.1: Diffraction of the incident shock wave: (i) plane initial shock; (ii) Mach reflection on the cone wall; (iii) stem-shock intersection on the cone axis; (iv) Mach reflection on the cone axis; (v) start of the second diffraction cycle. - - -, trajectory of the three-shock intersection (After Setchell [66]).

The run numbers and Mach number which are used in the TMZ growth determination are tabulated in Appendix A.4. A list of all the experiments done for this study is presented in Appendices A.1 and A.2 with comments for each experiment.

Figures 4.3 (a,b) show the spark schlieren pictures of TMZ in the first window location at two different times. The window locations and their design were discussed in detail in Chapter 2 but a figure showing schematically their locations is repeated here for convenience. The center of the windows is located at distances of 5, 13, and

21 in. from the entrance of the cone. These locations are also referred to as first, second and third window locations.

The interface is imaged dark due to the combination of schlieren effect and the scattering of light from the field of view by membrane fragments. The interface thickness is measured visually from the photograph (as shown in Figure 4.3). The interface thickness, defined as the thickness from the front to the back of the interface is represented here by δ. The x-location of the interface is defined to be the distance from the initial location of the interface to the middle of the TMZ. The time, $t = 0$, denotes the time when the incident shock wave interacts with the interface. The universal bubble and spike feature of this instability are not very evident here at late times because the bubbles tend to flatten out, possibly due to RT effect, and the spikes tend to break up due to the Kelvin-Helmholtz instability along their boundaries. It is also hard to see the 3-D disturbances with schlieren visualization. Figure 4.4, at window location 2, gives another clue that the interface is spread out near the wall, which possibly can corrupt the schlieren flow visualization since the technique uses line of sight integration.

To monitor the growth of the TMZ, it is photographed at the second ($x = 13$ in.) and the third window ($x = 21$ in.) locations. Figure 4.4 shows the TMZ in the second rectangular window location along with the numerically simulated result from AMRITA [60]. It should be kept in mind that the numerical calculations are Euler calculations and hence they give no idea of the mixing process in the TMZ. Hence the TMZ thickness cannot be inferred from these simulations. The reflected shock from the triple point interacts strongly with the interface during the initial stages, depositing vorticity of appropriate sign, which results in curving of the interface as is evident in Figure 4.4 (b). The main central shock, reflected shock and the Mach stem are clearly visible in this figure. Another measure of interface thickness, called the "geometric thickness", is defined in numerical simulations. This definition is motivated by the fact that in numerical simulations the interface curves into or away from the apex of the cone. It is defined to be the thickness of the interface on the cone centerline from the front of the interface to the projection of curved rear boundary

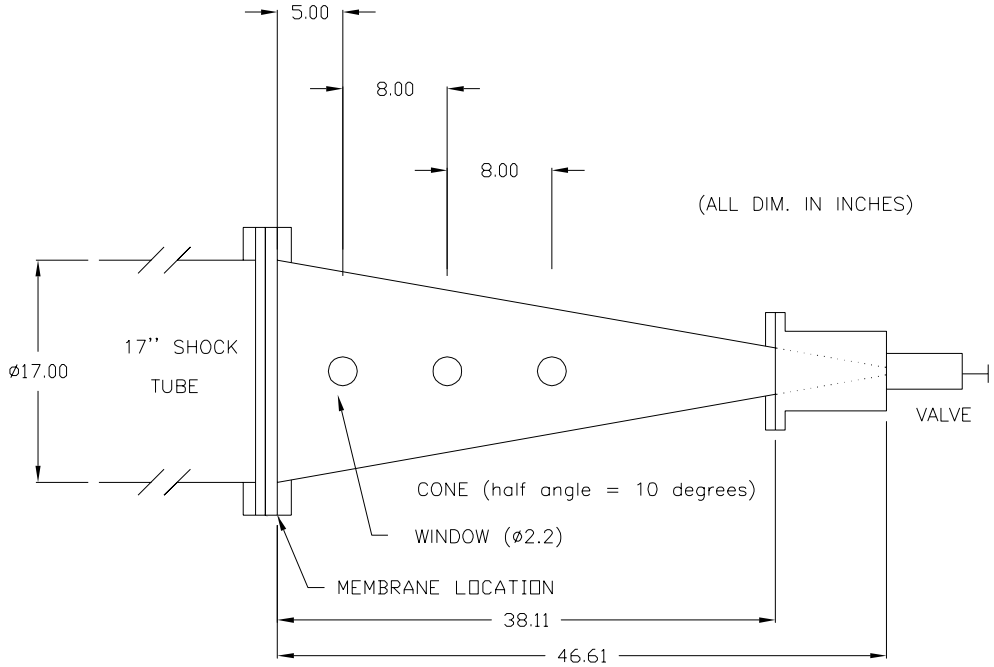

(a)

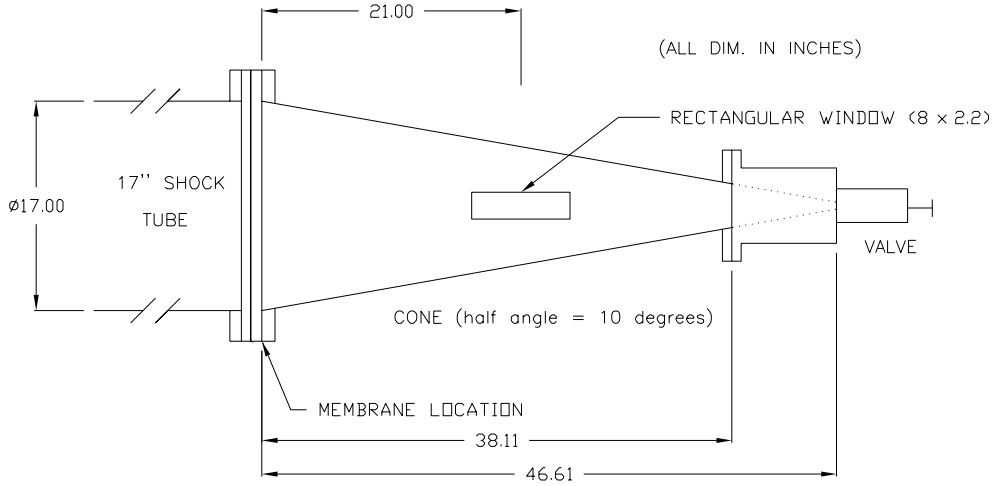

(b)

Figure 4.2: Schematic of the conical test section attached to shock tube. a) Test section showing the three circular windows. b) Test section showing the rectangular window at $x = 21$ in.

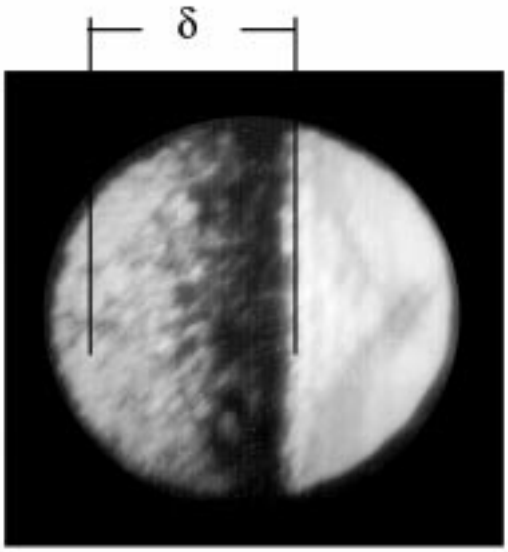

(a)

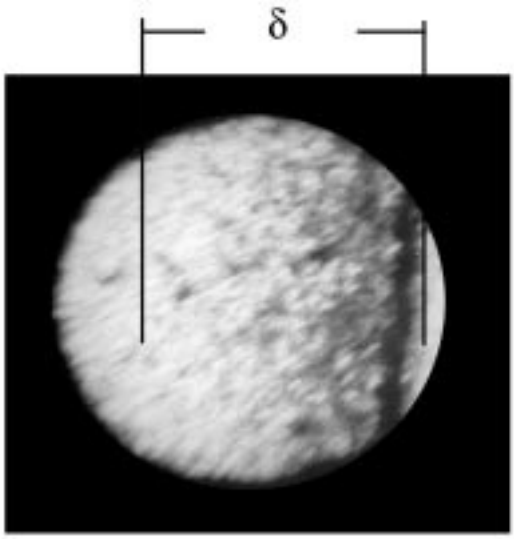

(b)

Figure 4.3: a) Schlieren image of TMZ at $x = 120$ mm and $t = 0.95$ ms. b) TMZ at $x = 135$ mm and $t = 1.04$ ms. Flow is from left to right with air/SF_6 (light-heavy) configuration.

near the wall on the cone centerline. This "geometric thickness" is illustrated for the numerical result of Figure 4.4 (b) in Figure 4.5.

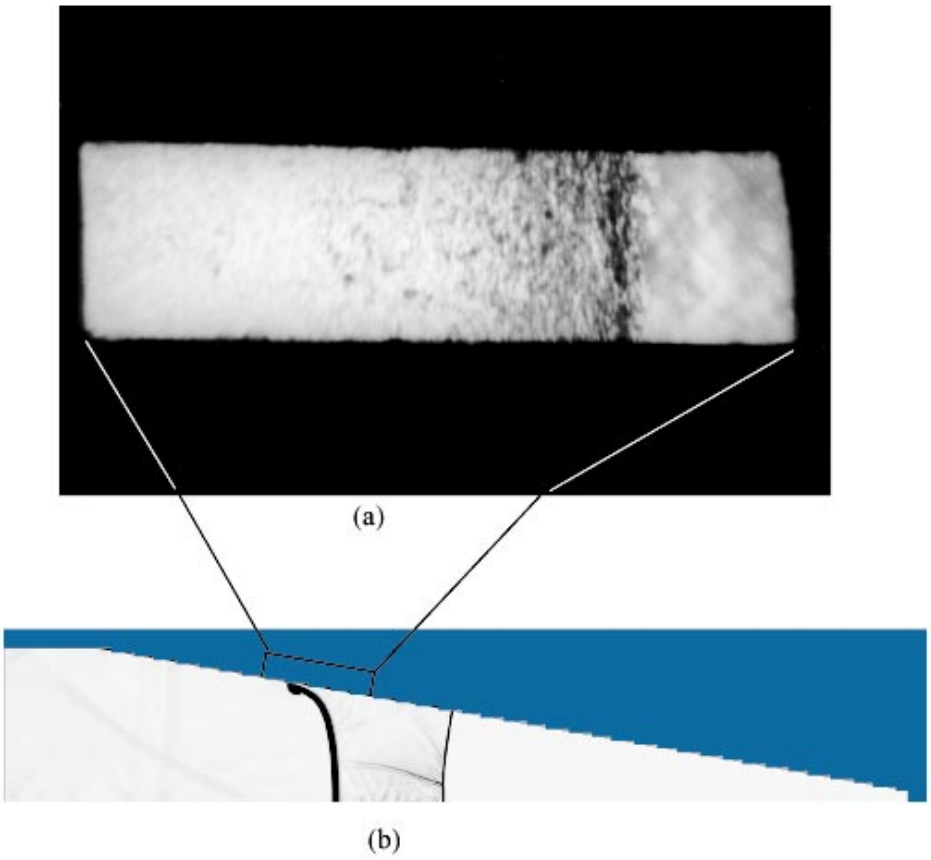

Figure 4.4: (a) Schlieren image of TMZ at $x = 336$ mm and $t = 2.42$ ms from run number Rshot67. (b) Numerical simulation result at about same x/L. Flow is from left to right with air/SF_6 (light-heavy) configuration, the window location is also shown on the numerical data.

In the experiments done by the researchers on RM instability, the interface thickness is measured "visually" from the photographs [47, 61, 21, 22, 19, 23, 63, 74] and is called the "visual thickness". In the present experimental conditions with conical geometry, the front of the interface advancing in the test section is very well demarcated, but the rear boundary is rather diffuse, as shown in Figure 4.4 (a). A technique was devised to analyze the interface using image processing. The visible image in the rectangular window (2164 $\times$ 526 pixels in size for Figure 4.4 a) was digitized and the average gray-scale intensity of each pixel column was computed. These average inten-

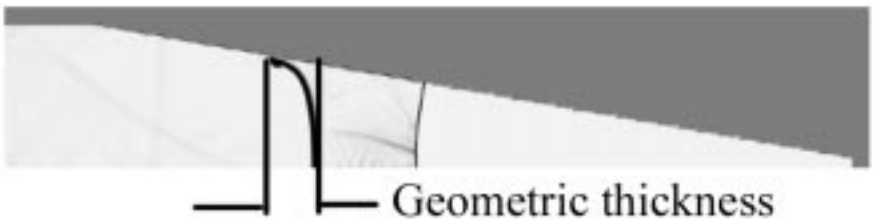

Figure 4.5: Geometric thickness defined

sities are plotted against the horizontal distance in pixels, Figure 4.6. An intensity of 0 is the darkest and 256 is the brightest. The average intensity shows a sharp gradient at the advancing front of the TMZ as expected. Inside the TMZ, the average intensity fluctuates due to the schlieren effect of the random density variation produced by the mixing blobs. At some distance behind the advancing front, the fluctuations in the intensity die down and the intensity varies smoothly. The rear end of the TMZ can be taken to be the location where these fluctuations in intensity seem to stop (with an uncertainty of 10–15%). This technique is illustrated in Figure 4.6 for the TMZ shown in Figure 4.4 (a). This technique was applied to the schlieren pictures of TMZ at the second window location because it was at this location that the TMZ had a long diffuse rear boundary. Section A.2 of Appendix A shows this for four other runs at $M_S = 1.55$. The "visual thickness" obtained by observing the photographs matches closely to the ones obtained by this image processing technique to within 10 to 15%. The "visual thickness" and the thickness determined from this technique are tabulated in Table 4.1.

Run number	**Mach number** ± 0.01	**Visual thickness (mm)**	**Thickness from image processing (mm)**
Rshot 67	1.56	91	81.2
Rshot 81	1.57	102	93.67
Rshot 82	1.56	107	107
Rshot 95	1.55	93.13	77.6
Rshot 97	1.57	115	100.1

Table 4.1: Visual thickness and thickness from image processing

This technique obviously works in cases where both the front and rear of the TMZ

are clear, as in Vetter's [74] pictures.

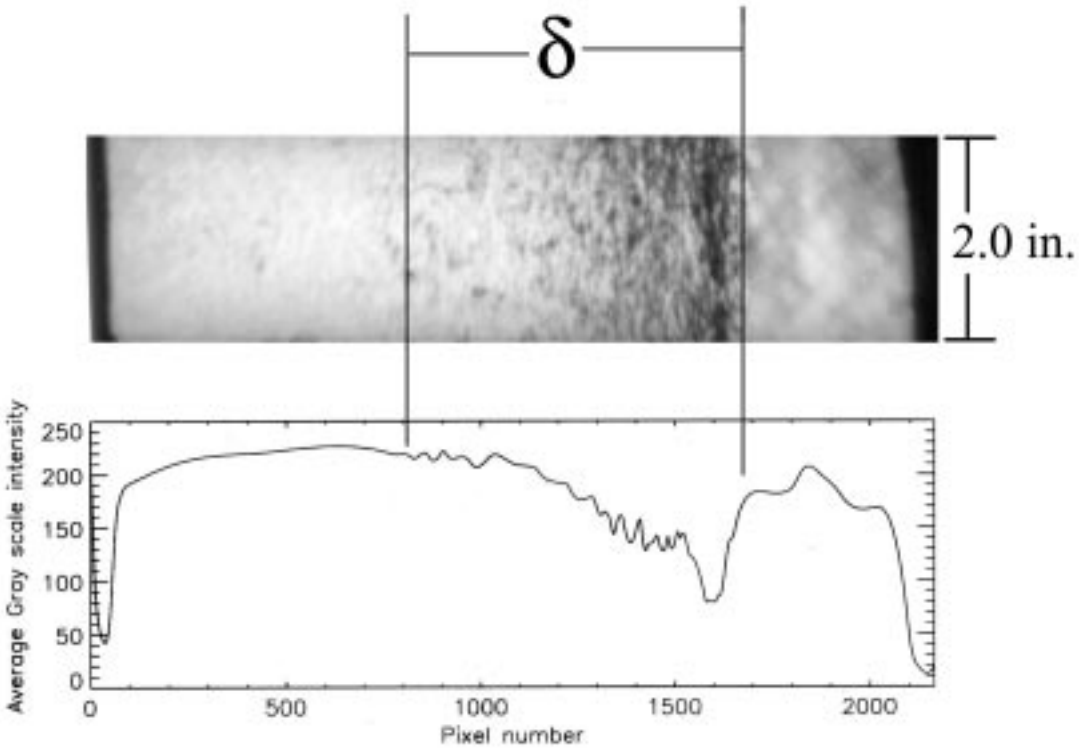

Figure 4.6: Illustration of image processing technique to fix the boundaries of TMZ for the TMZ shown in Figure 4.4 (a). The image size is 2164 $\times$ 526 pixels which corresponds to physical dimension of 8.2 $\times$ 2 in.

Figure 4.7 (a) shows the mixing zone at the third window location (see Figure 4.2 for window details). It is clear from the figure that the mixing zone completely fills the viewing window. In order to locate the other boundary of the TMZ, the experiment was repeated with same settings, except that the visualization was done in the second rectangular window. The second and the third rectangular windows are located side by side along the axial direction, though they are offset in the circumferential direction. The third rectangular window can be viewed as continuation of the second rectangular window. Figure 4.7 (b) shows the schlieren image of TMZ in the second rectangular window corresponding to the settings of Figure 4.7 (a). It is clear that there is no mixing visible in this image and hence the TMZ thickness can be taken as the mixing zone visible in Figure 4.7 (a), where the rear of the mixing zone is bounded

by the window wall. The two photographs in Figure 4.7 were taken on different runs and hence the absence of mixing in Figure 4.7 (b) does not mean there was absolutely no mixing going on behind the rear boundary of window in Figure 4.7 (a). The error in this mixing zone width is equal to the scatter in the front of the TMZs, visible in the repeatability demonstration Figure 4.9. Figure 4.7 (a) also shows clearly the intersection of reflected shocks at the centerline of the cone. The interface moves into the cone and comes to a stop at an axial location depending on the Mach number. This is clear from the $x - t$ diagram (see Figure 2.2) computed from the numerical computations for incident Mach number of 1.56 in light-heavy case. Figure 4.7 (a) also shows the TMZ before the central reflected shock interacts with it a second time. Similarly, the growth of TMZ was also observed at Mach number of 1.39 in the first and the third window. In order to see how the membrane appears in these schlieren pictures (with the same settings as the air/SF_6 interface pictures), experiments were conducted with air on both sides of the interface. Figure 4.8 shows the air/air interface. It is clear from the figure that the membrane fragments appear as dark in the front of the interface because they get clustered together there. When the same fragments are not clustered they appear as white. This clustering of the fragments is also evident in the laser-induced scattering image of Figure 4.15 (b).

The growth of the TMZ obtained in this fashion clearly depends on the repeatability of the experiments as each schlieren picture is obtained from a different experiment. The extent of repeatability in the present experimental conditions is shown in Figure 4.9. The maximum separation between interface advancing fronts in Figure 4.9 is about 15 mm, which is due to the variability in the Mach number.

Having obtained the interface location, thickness and timing at three locations, the $x-t$ diagram was plotted featuring the experimental data points for Mach number 1.55 and the numerical computations. Figure 4.10 shows such a plot. It is clear that data obtained from experiments occurs before the interface is rapidly decelerated to zero velocity. During the period of experimental observations the interface moves at a uniform velocity. This eliminates the possibility of strong RT effect which comes

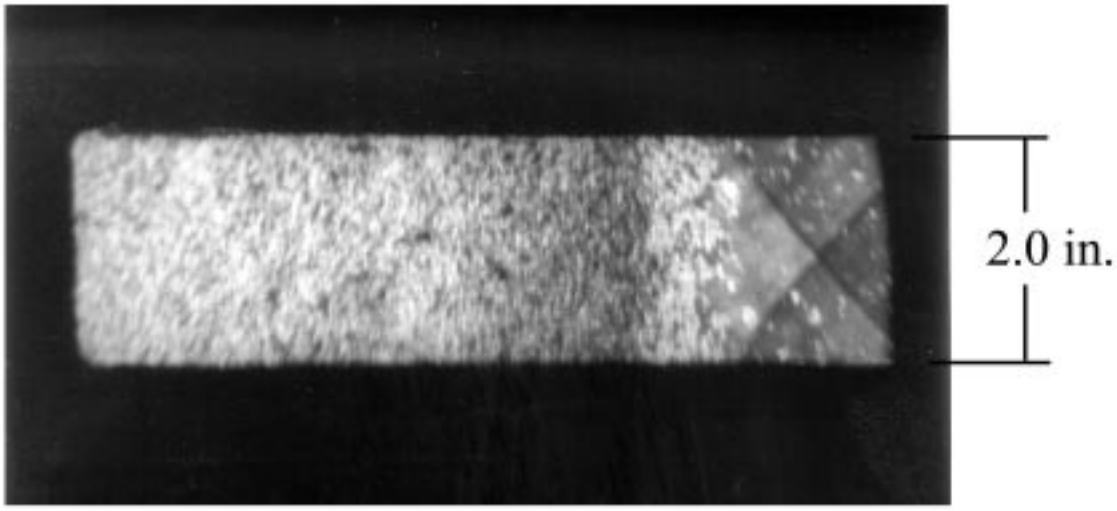

(a)

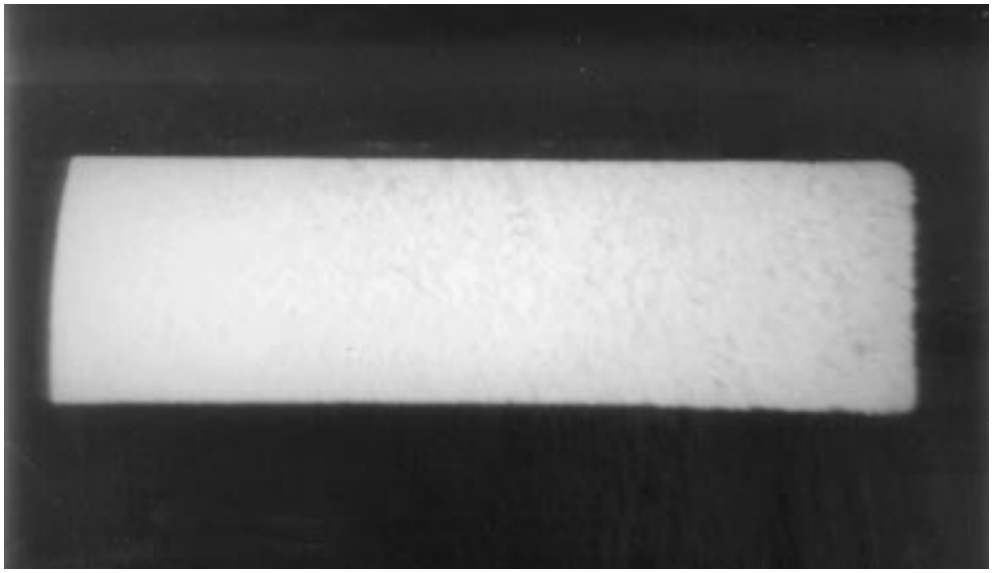

(b)

Figure 4.7: a) Schlieren image of TMZ at $x = 506$ mm and $t = 3.68$ ms, $M_S = 1.57$. b) Schlieren image of TMZ in second rectangular window at the same settings as in (a) (the flow is from left to right).

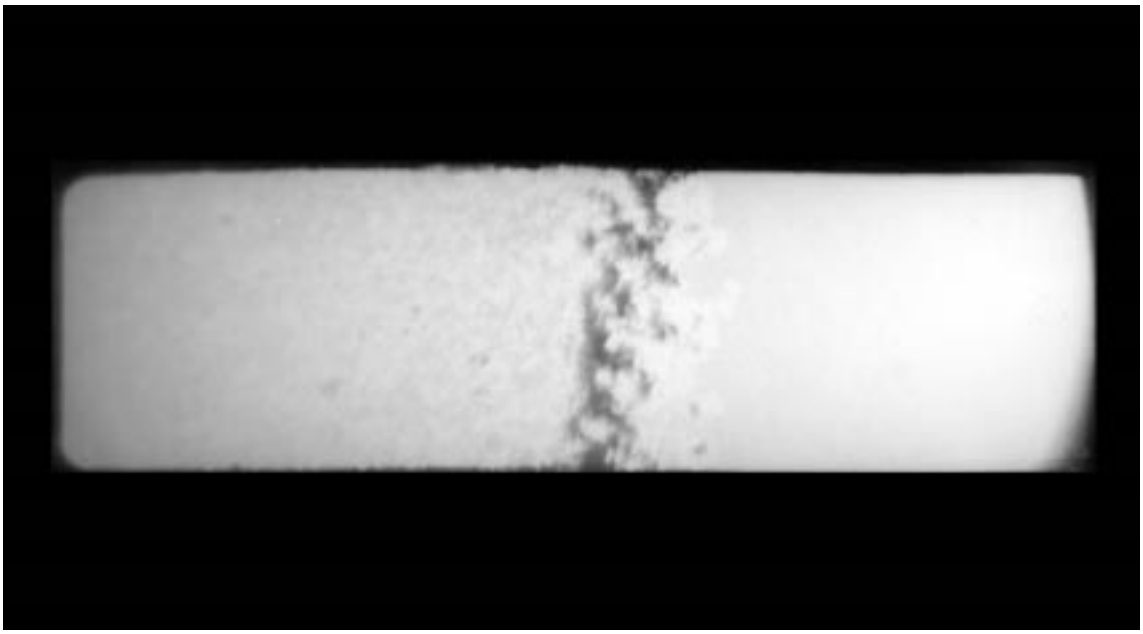

Figure 4.8: a) Schlieren image of air/air interface in the second window location at $x = 13$ in. and $t = 1.52$ ms, $M_S = 1.59$, showing the membrane fragments getting clustered in the front of the interface. The flow is from left to right.

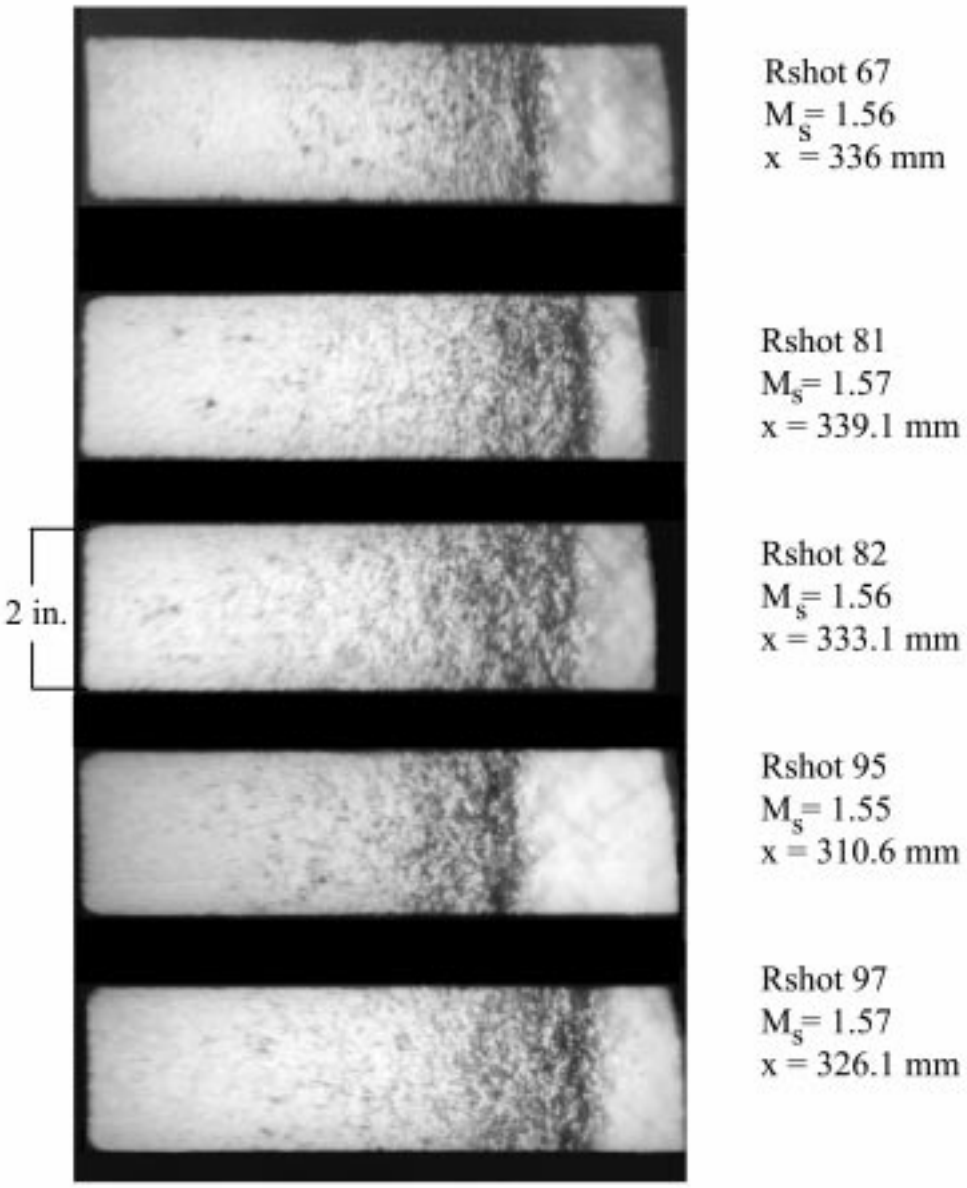

Figure 4.9: Demonstration of the extent of repeatability of the experiments in the second rectangular window location.

into play during the rapid deceleration phase of the interface.

4.1.1 Dominant scale size determination

The schlieren pictures show dark blobs which are created by the refraction of light through density gradients in the TMZ and appear as scattered dark spots on the pictures involving the air/SF_6 interface. The size of these blobs give an estimate of the dominant scale of eddies which are involved in the mixing process. It should be kept in mind that the schlieren effect results from the density gradients, due to mixing of the gases, and also, to a smaller extent, due to membrane fragments. To get an idea of this blob size, a 256×256 pixel image was sampled from the upper-right corner of mixing zone shown in Figure 4.4. It is again shown in Figure 4.12. The surface plot of its Fourier power spectrum density (psd) and its radial power density is shown in Figure 4.13. The wave number is normalized in a way that the wave number in the plots represents the number of wavelengths in the 256 pixel domain. To obtain the radial power spectral density plot from the surface plot of psd, power (in rings of two wave number unit width) was added at various radial locations and the value was assigned at the radius to the middle of the ring. This procedure is illustrated schematically in Figure 4.11.

The maximum power density occurs at a wave number of 3 (see Figure 4.13 b) implying that there are three waves of dominant wavelength in 256 pixels which translates to dominant blob size of around 4 mm in actual scale. This size is about half the spacing (8 mm) between the wires of the wire-mesh frame which holds the polymeric membrane forming the initial interface seperating the two gases. The same process was repeated by taking portions of image from various places of the same TMZ image and also at the various axial locations of the observation windows. The dominant size of these structures did not vary, *i.e.*, it was same 4 mm as found earlier. Figure 4.14 shows the image of Figure 4.12 (a) with markers indicating the dominant scale/eddy/blob size of 4 mm, thus obtained from the radial power spectral density plot.

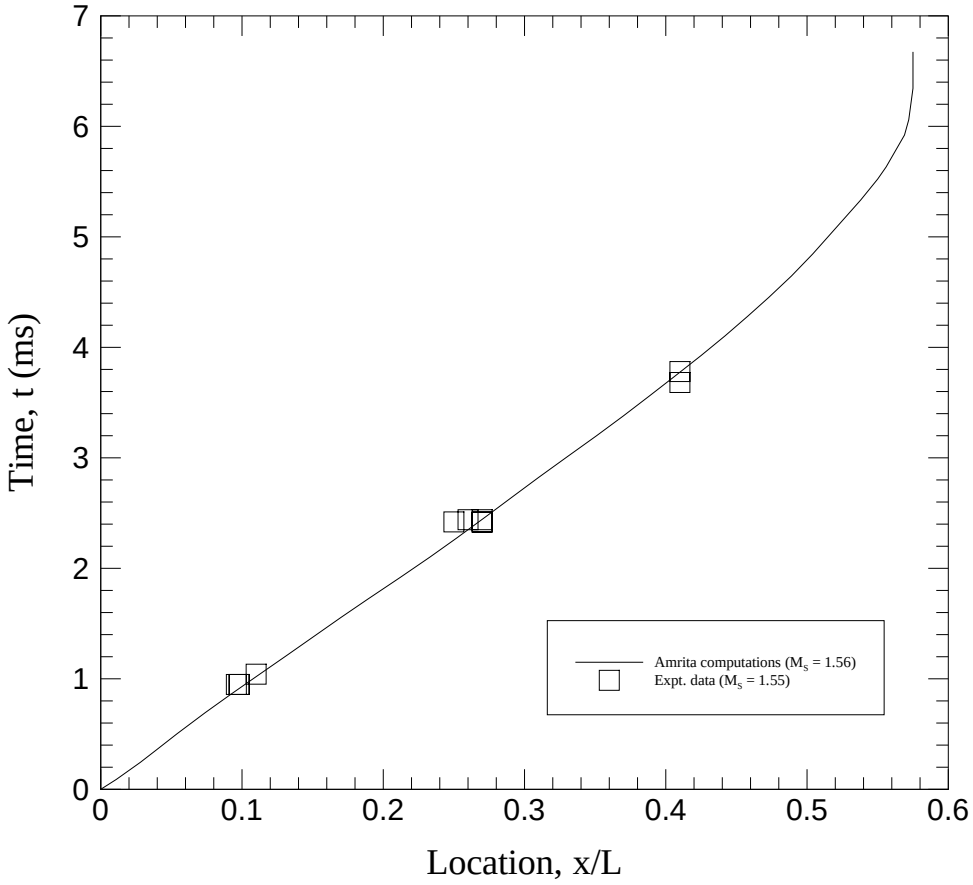

Figure 4.10: $x-t$ diagram from numerical computations along with the experimental data points at Mach number of 1.55.

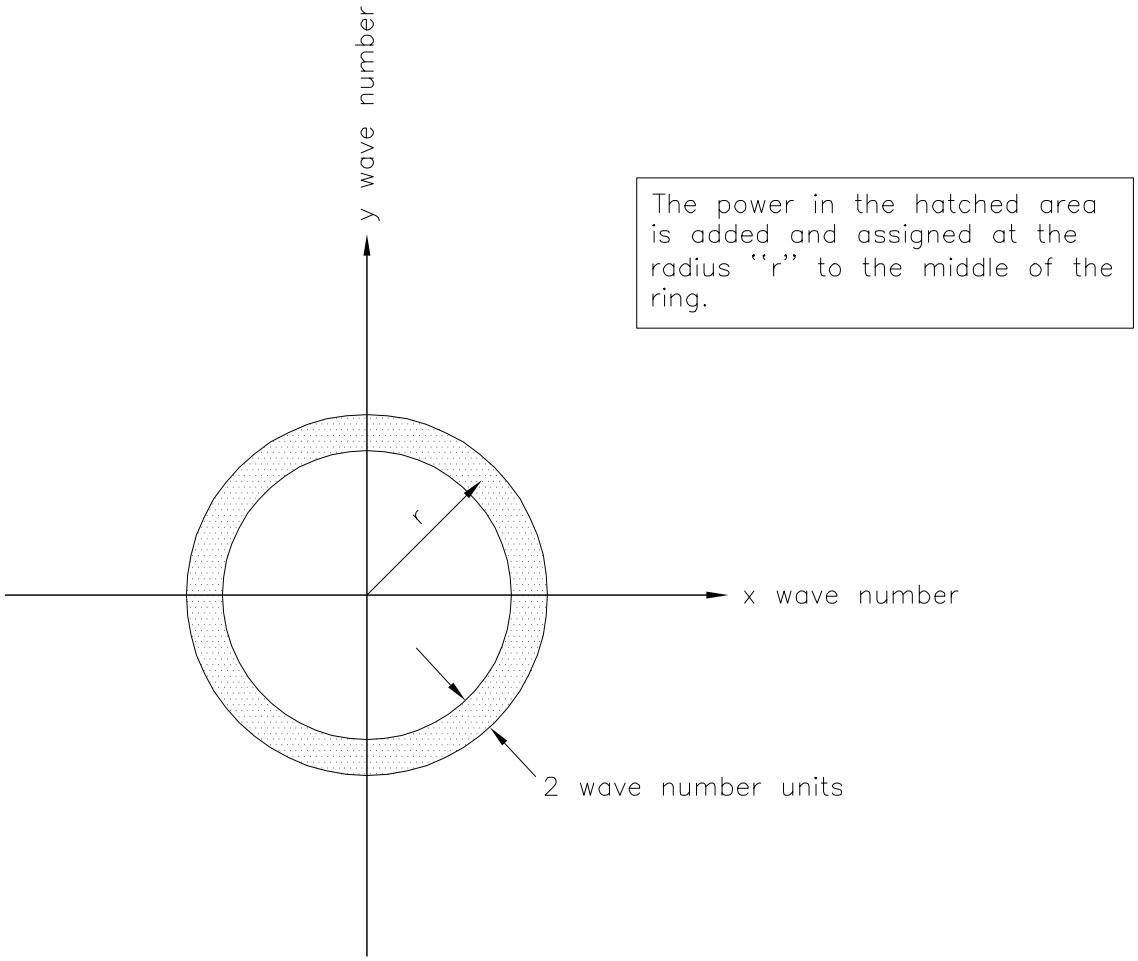

Figure 4.11: Schematic of the procedure to obtain radial power spectral density from surface psd plot.

4.1.2 Laser-induced scattering result

As is evident from the numerical simulation result in Figure 4.4 (b), the interface bends near the walls. Since the schlieren pictures give the line of sight integrated effect, it is possible that the TMZ visible in the pictures has the effect of this curvature. The only way to eliminate this effect is to study the TMZ with sheet optics techniques. To probe the TMZ in detail, laser-induced scattering from a laser sheet was attempted (see Section 2.9 for details of the setup and the difficulties encountered in doing this experiment). In this experiment, the test gas was helium in the heavy-light configuration. Since the absolute values (0.67 and 0.76) of Atwood numbers of air/SF_6 and air/He are similar, the mixing zone width is expected to be similar, at least before the arrival of the main central reflected shock. The helium in the test section is seeded with olive oil fog particles. Figure 4.15 (a) shows the image of the light sheet in the test section seeded with oil particles and helium, and Figure 4.15 (b) shows the TMZ as it appears in front of the observation window.

The membrane fragments clearly scatter lots of light and hence are a source of noise. But the fine bright particles at the rear of the TMZ represent the oil particles from the right. This at least gives an idea of the extent of mixing in TMZ (visual thickness is 87.3 mm in that picture) in that condition. The curving of the interface is not visible because the viewing area is too small. The extent of the mixing zone in this image, which shows the full rectangular window of size 8×2.2 in., is similar to the one in Figure 4.4 (a) where the visual thickness is 91 mm. The mixing zone in Figure 4.15 (b) shows that, in the center of the test section, the TMZ does not have a well-demarcated rear boundary, but is rather diffuse. The schlieren picture of the TMZ corresponding to the laser-induced scattering image of Figure 4.15 (b) is shown in Figure 4.16. The flow visualization picture in Figure 4.15 (b) also shows that the present technique of visualizing TMZ by light scattering is not the best method due to the noise generated by the membrane fragments. A more effective way of solving this problem is to use laser-induced fluorescence by mixing a fluorescent oil-soluble dye (for example, pyrromethene-597 or rhodamine-640 are easily excited by 532 nm

Nd-Yag laser in oil) with olive oil in the fog generator and using an appropriate filter in front of the CCD camera. This was attempted with the result that fluorescence was too weak to be detected by an ordinary CCD camera, thus requiring the use of an intensified CCD camera. As a result, further experiments with sheet optics were abandoned.

4.1.3 Effect of transverse reflected waves on the growth of small initial perturbations: an inviscid computational study

In this study on the conical geometry, a triple point is created on the shock wave as it enters the cone. As a result, the reflected shock wave originating at the triple point moves transversely across the cone, focusing and reflecting from the cone axis. In doing so, these transverse waves interact with the interface behind them. This interaction gradually becomes weaker as the triple point moves farther from the interface. It is these interactions at the early times which lead to the curving of the interface globally (as is clearly evident in Figure 4.4 b, where the interface curves towards the apex of the cone). A computational study was undertaken at Mach number of 1.56 in light-heavy configuration to study the affect of these transverse waves on small initial sinusoidal perturbations using AMRITA [60] (see Section 4.2 for some discussion on AMRITA) by comparing the growth under the same conditions as that in the straight cylindrical geometry. The growth of the perturbations in these calculations results solely from the vorticity deposited by the initial interaction of the shock with the perturbed interface. These calculations are inviscid and hence do not reflect the role of viscosity in the TMZ growth dynamics. Figure 4.17 compares these results on perturbation growth for cylindrical and conical geometries at about same x/L as the window locations in the experiments. The initial amplitude of the perturbations is 1.25% of the wavelength. The interface geometry in the Figure 4.17 at various locations indicates that the amplitude growth in both cylindrical and conical geometries is the same. The main affect in the conical geometry being the global curving of the

interface towards the apex of the cone. This suggests that the diffuse rear boundary of the interfaces observed in the experiments could be an artifact of this global curving of the interface and hence any enhanced growth could be attributed to it. But, as is evident from the laser-induced scattering results in Figure 4.15 b, the interface in the middle of the test section does not have a well-defined rear boundary either. Rather, small blobs of fluids on the right are scattered in the TMZ. This formation of the blobs of fluid, which is governed by other complex fluid-dynamical phenomenon such as development of secondary instabilities among others, is not captured by the computational results.

4.1.4 Growth rate results

The growth of the TMZ thus obtained by spark schlieren technique is plotted in Figure 4.18. Figure 4.18 (a) shows the TMZ growth in time. It is clear that the growth is significantly more than Vetter's data at late times. Vetter's [74] data corresponds to the same conditions but with no area convergence effect. His experiment was at a Mach number of 1.5. The data plotted is the "visual thickness" observed from the photographs obtained by schlieren technique. The data from Vetter's graph corresponds to his m-(v-h) configuration, which means, in the initial interface formation, the membrane (m) was followed downstream by vertical (v) and horizontal (h) wires. This is also the configuration used in the present experiments. This configuration results in maximum growth rate as compared to his other initial configurations of membrane (m), horizontal wires (h) and vertical wires (v), i.e., v-m-h and (v-h)-m configurations. The reason for this was pointed out by Vetter as being possibly due to the smaller damping effect produced by relatively smaller membrane fragments. The interface thickness in the second window location is about 40–50% more than Vetter's data at the same time. Again, this result is fully based on the TMZ thickness obtained from the pictures and it is possible that some of it is an artifact of global curving of the interface. A linear fit to the data shown in Figure 4.18 (a) gives a mean growth rate of 45 m/s which is about 5 m/s more than that obtained by Vetter [74]

after the reflected shock. Also plotted in Figure 4.18 (a) is Mikaelian's Equation 1.17 which is supposed to be valid at late time RM instability growth with no area convergence. The interface velocity used in this equation is 144 m/s, obtained from the x-t diagram in Figure 4.10, and the post-shock Atwood number used is 0.74, obtained from the conditions just after the interaction of incident shock. Figure 4.18 (a) also shows the evolution of "geometric thickness" from light-heavy configuration at Mach number of 1.56. The "geometric thickness" tends to reduce at later times due to the rapid RT stabilizing affect at those times. The plotted "visual thickness" in the figure is more than the "geometric thickness" at later times. The diffuse rear end of the interfaces in schlieren images thus could be the real nature of the interface in the cone center, or it could also be the artifact of the curved interface interacting with the wall boundary layer. The shock tube used in the present experiments is the same as that used by Vetter [74] where no boundary layer effects (due to the large test section size) were seen. In the present case, the interaction of the interface with the wall boundary layer is fairly complex due to its curved nature near the wall. Figure 4.18 (b) shows the axial locations of the TMZ plotted against x/L, L being the length of the cone assumed end at a point. Figure 4.19 shows the interface thickness with distance in millimeters along with Vetter's data [74] before the interaction with reflected shock.

4.2 Some computational studies

The computations were carried out on the software system AMRITA designed by James Quirk [60]. It is a system that automates and packages computational tasks in such a way that the packages can be combined (dynamically linked) according to instructions written in a high-level scripting language. The present application uses features of AMRITA that include the automatic construction of different Euler solvers, automatic documentation of the codes, automatic adaptive mesh refinement according to simply chosen criteria, archiving and post-processing of the results. The automation of the assembly and sequencing of the tasks dramatically reduces the possibility of hidden errors. More importantly, it makes computational investigations

transparent and testable by others. The ability to change one package at a time, without changing the rest of the scheme, permits easy detection of sources of errors. The scope of the software package far exceeds its use here.

Numerical computations using AMRITA were performed on various configurations in a cone with half-angle of 10 degrees to study the interface geometry changes, which it experiences as it focuses in a cone. Both light-heavy (LH) and heavy-light (HL) configurations, with air/SF_6 or air/He gas combinations respectively, were computed at the same Mach number as in the experiments. Plane or spherical shock (PS/SS) interacting with a plane or spherical interface (PI/SI) was studied. It should be noted that these calculations are Euler calculations and hence do not give TMZ growth rate, which is governed by the dynamics of turbulence taking place at the interface. Various cases studied computationally are tabulated in Table 4.2.

Case number	**Mach number**	**LH or HL configuration**	**Shock/Interface configuration**
1	1.56	LH	PS/PI
2	1.56	LH	SS/SI
3	1.56	LH	PS/SI
4	1.60	HL	PS/PI
5	1.60	HL	SS/SI
6	1.60	HL	PS/SI

Table 4.2: Various cases studied computationally

Figure 4.20 shows the geometry and location of the interface at various times as it implodes in the cone in Case 1. Time $t = 0$ always corresponds to the instant when the incident shock interacts with the interface. The curving of the interface towards the converging side of the cone is due to the vorticity being deposited on the interface due to its interaction with the reflected shock from the triple point. In the last snapshot the interface has almost stopped. Figure 4.21 shows the results of interaction of spherical shock with spherical interface in light-heavy configuration (Case 2). There is no Mach reflection on the boundaries of the cone. Due to the absence of interaction of reflected shock with the interface, there is no global change in its geometry. The rolled up sheet visible in the picture is *not* the interface, rather it is the contact surface

resulting from the initial generation of the shock. The rolling up occurs because of the grid noise, the interface being not aligned with the cartesian grid used in these computations. All the features near the left boundary of the domain in the cases of spherical shock or interface should be ignored, as they are artifacts of the grid noise. The interface in the last snapshot has not stopped but will move at later times. Figure 4.22 shows the results for interaction of plane shock with spherical interface in light-heavy configuration (Case 3). The vorticity deposited at the interface by the reflected shock originating from the triple point turns the interface in the same sense as in Case 1. The interface thus tends to become flat as time proceeds and in the last snapshot it has almost stopped.

Numerical simulations were also performed in heavy-light configuration (air/He). The various geometric configurations studied were the same as in Cases 1, 2 and 3 at Mach number of 1.60. Figure 4.23 shows snapshots of plane shock and plane interface interaction in heavy-light configuration (Case 4). In heavy-light configuration the density gradient is reversed from the light-heavy configurations resulting in the reversal of baroclinic torque, hence the vorticity deposited at the interface by the reflected shock from the triple point is of opposite sign from Case 1. The interface in Case 4 thus curves outwards in contrast to Case 1. Also, in Case 4 the main reflected wave at $t = 0$ is an expansion wave as expected. The interface comes to a stop much earlier at $x/L = 0.289$ as compared to $x/L = 0.575$ in Case 1 with light-heavy configuration. The laser-induced scattering image from the experiments in Figure 4.15 (b) is at about $x/L = 0.274$, which is close to the last snapshot of numerical results in Figure 4.23. Figure 4.24 shows the case of spherical shock and spherical interface interaction in heavy-light configuration (Case 5). Again as in Case 2 there is no Mach reflection and the main reflected wave formed at time $t = 0$ is an expansion. The interface in the last snapshot shown here has not yet stopped. Here no global change in interface geometry takes place. Figure 4.25 shows the case of interaction of plane shock with a spherical interface in heavy-light configuration (Case 6). Here the interface near the axis initially gets compressed by the shock and tends to flatten out yet at later times it tends to bow outwards in contrast to Case 3.

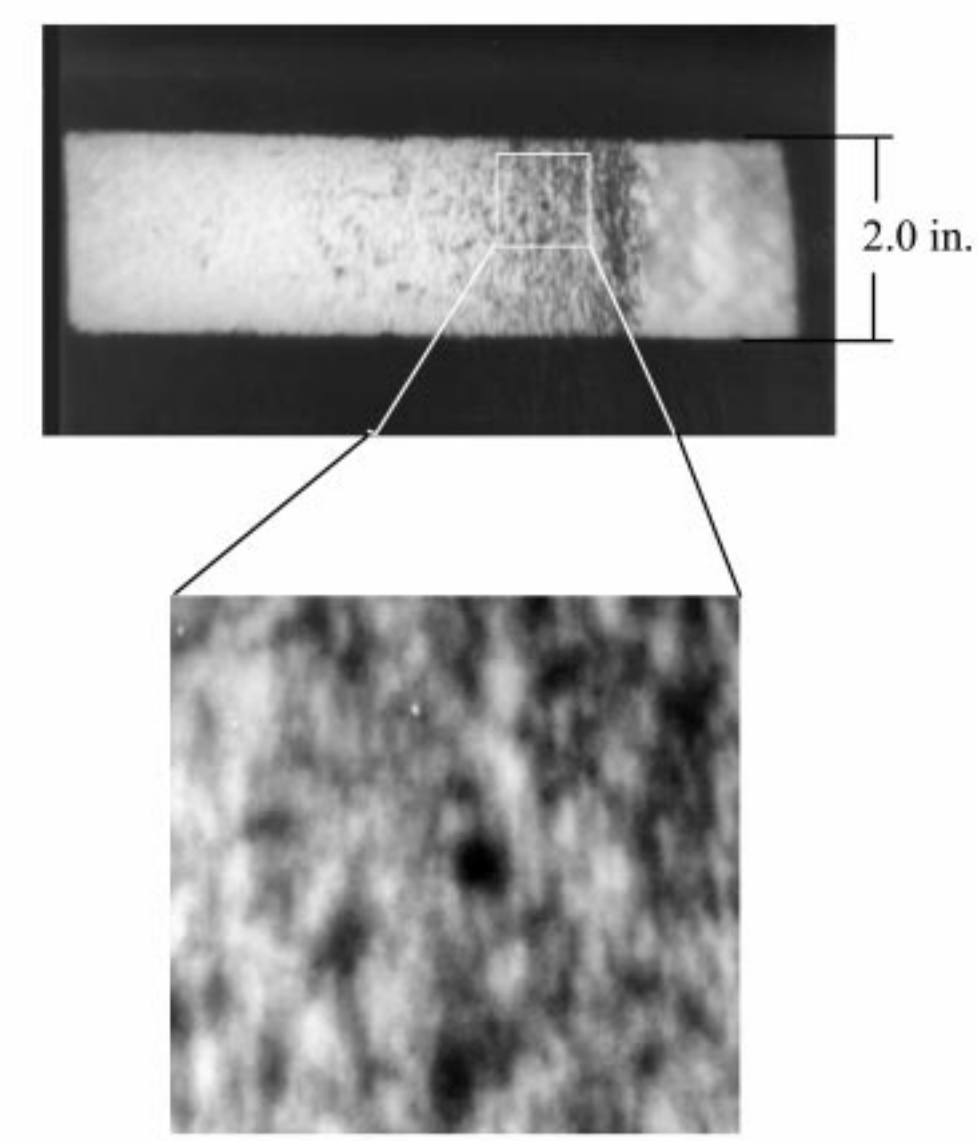

Figure 4.12: A 256×256 pixel image sampled from the TMZ of Figure 4.4 (a) for dominant scale size determination by image processing.

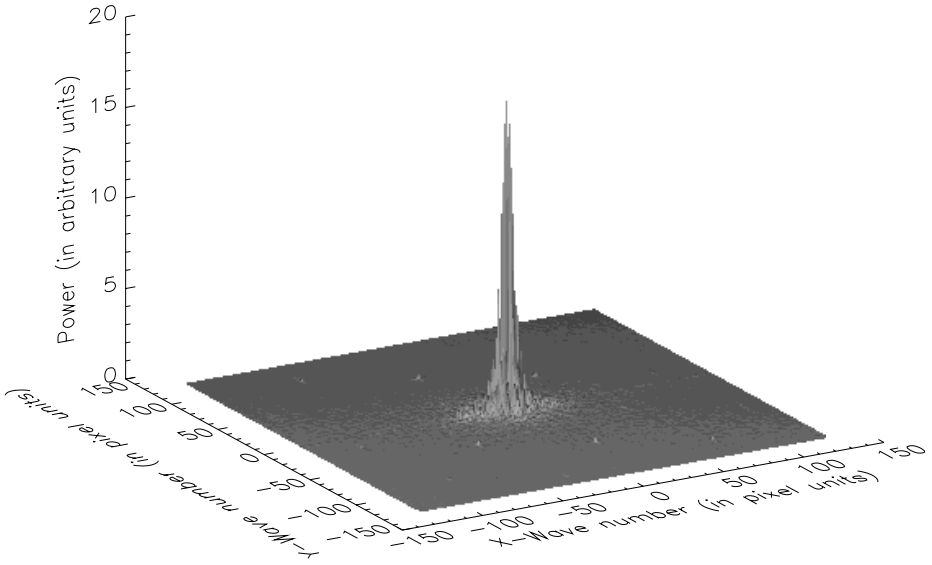

(a)

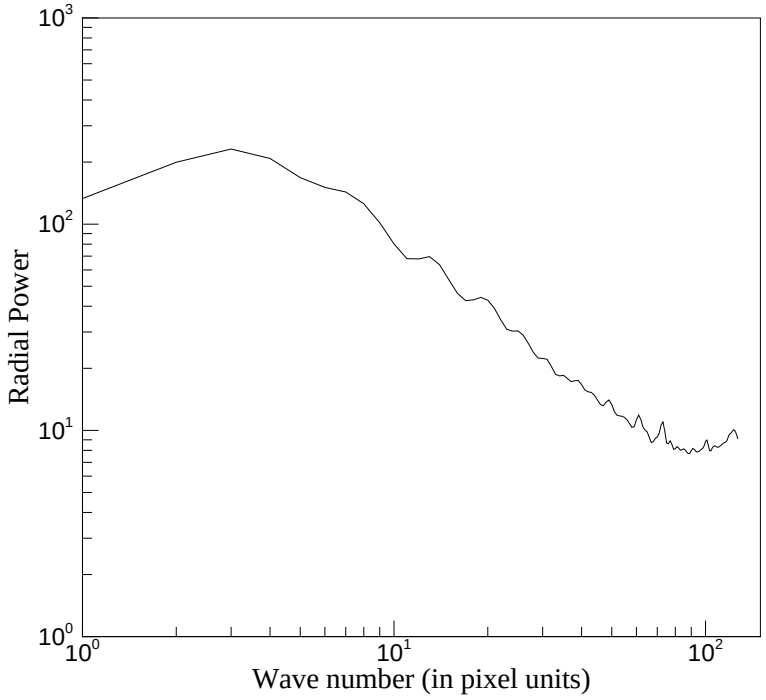

(b)

Figure 4.13: a) Surface plot of power spectral density for sampled image of Figure 4.12. b) Radial power spectral density.

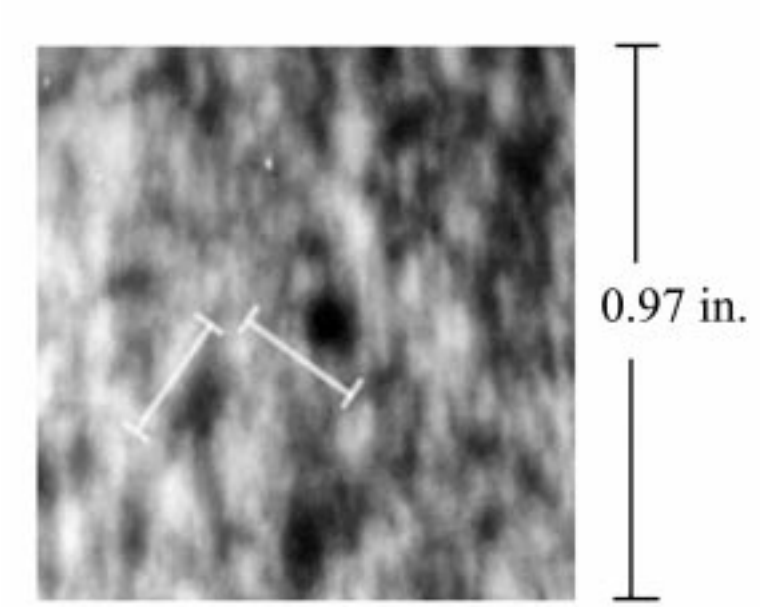

Figure 4.14: Picture of the sampled image in Figure 4.12 with markers indicating the dominant size of scales obtained from the maxima in radial power spectral density plot of Figure 4.13 b.

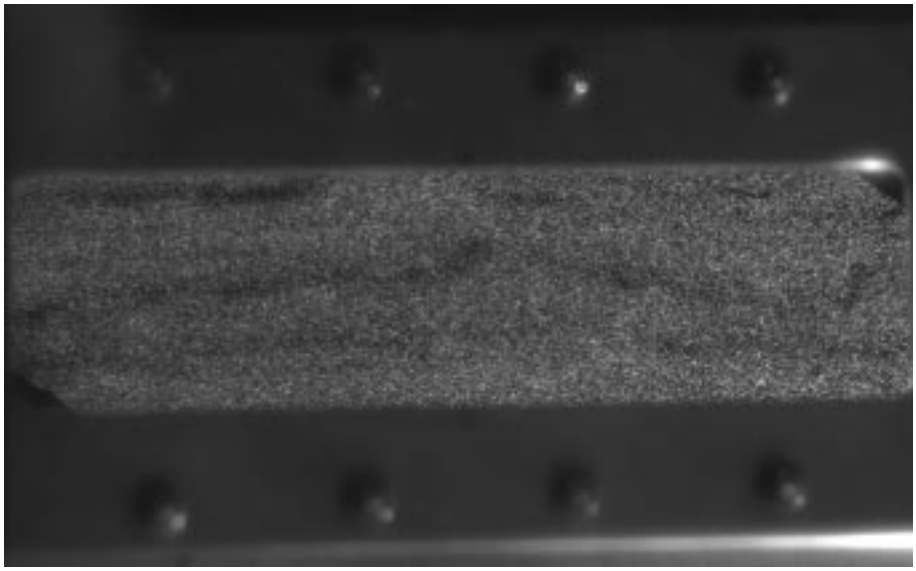

(a)

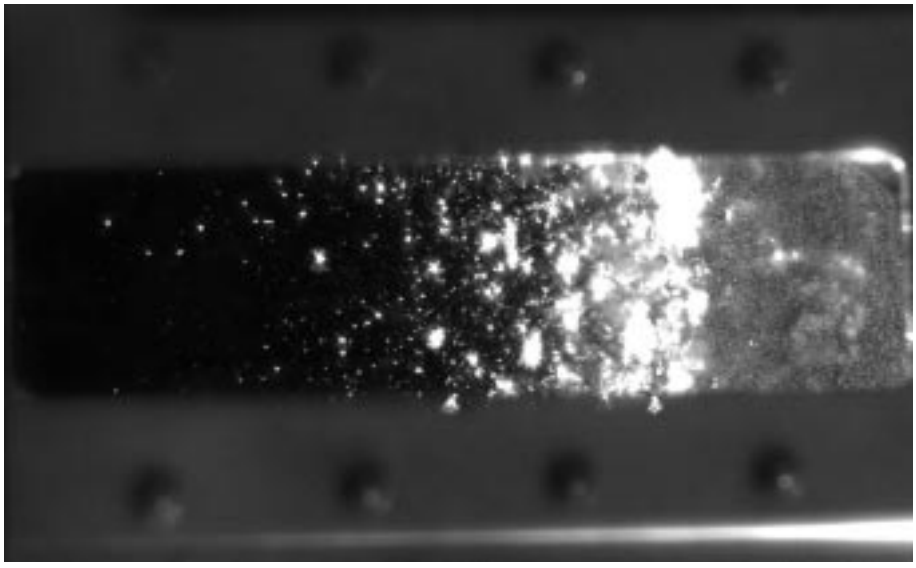

(b)

Figure 4.15: Laser-induced scattering experiment (heavy-light configuration) in second window location at $x = 13$ in. a) Laser sheet in the test section with helium and olive oil fog particles. b) The TMZ with membrane fragments visible as relatively big bright scattering spots and very fine bright dots representing the seeded oil particles from the right, $t = 1.25$ ms, $M_S = 1.60$.

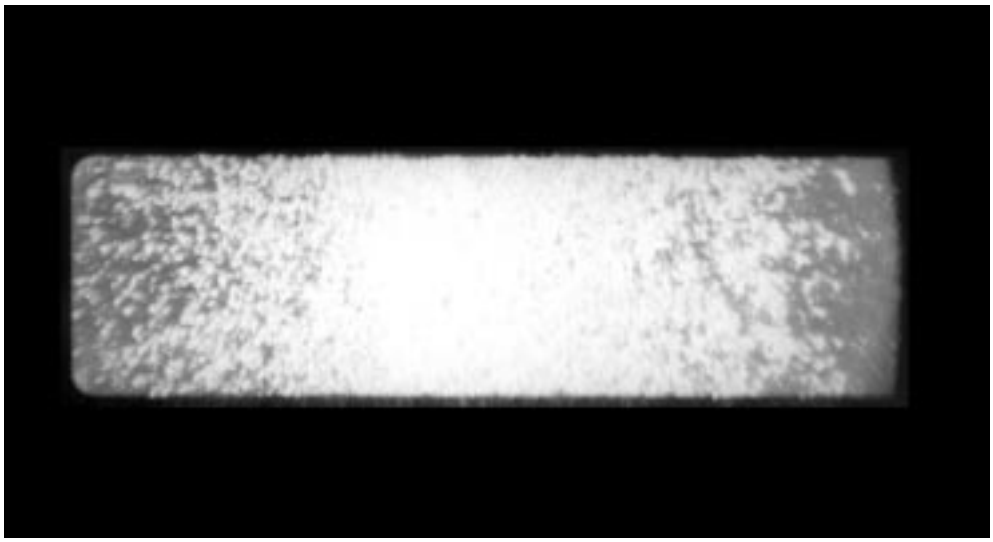

Figure 4.16: Schlieren image of air/He interface in second window location at $x = 13$ in., $t = 1.25$ ms, $M_S = 1.60$ (flow is from left to right).

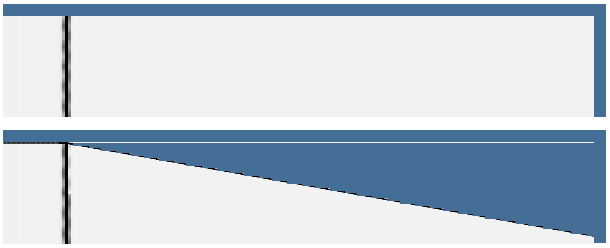

$x/L = 0$

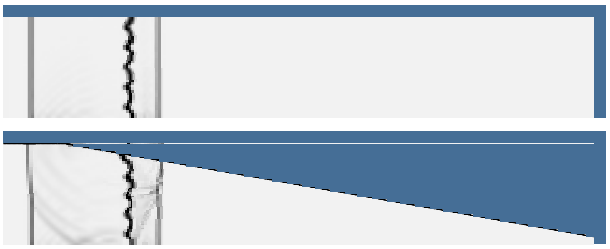

$x/L = 0.103$

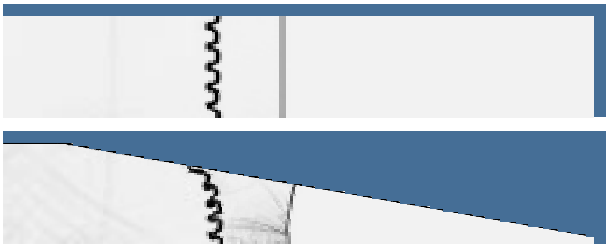

$x/L = 0.268$

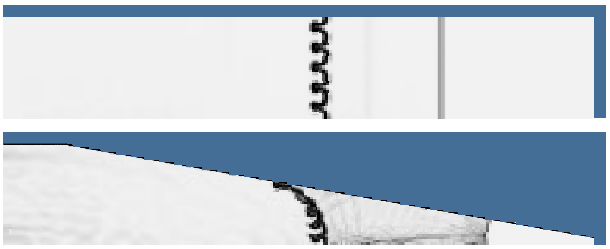

$x/L = 0.432$

Figure 4.17: Numerical simulation: Comparison of the growth of small sinusoidal perturbations in a cylindrical and conical geometry at three locations, x/L. Light-heavy configuration, $M_S = 1.56$, L is the cone length extrapolating to the apex.

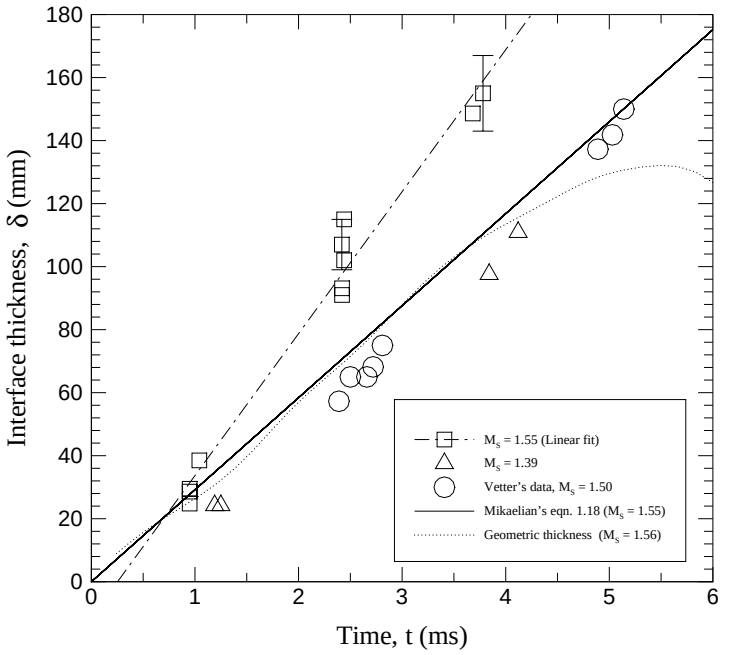

(a)

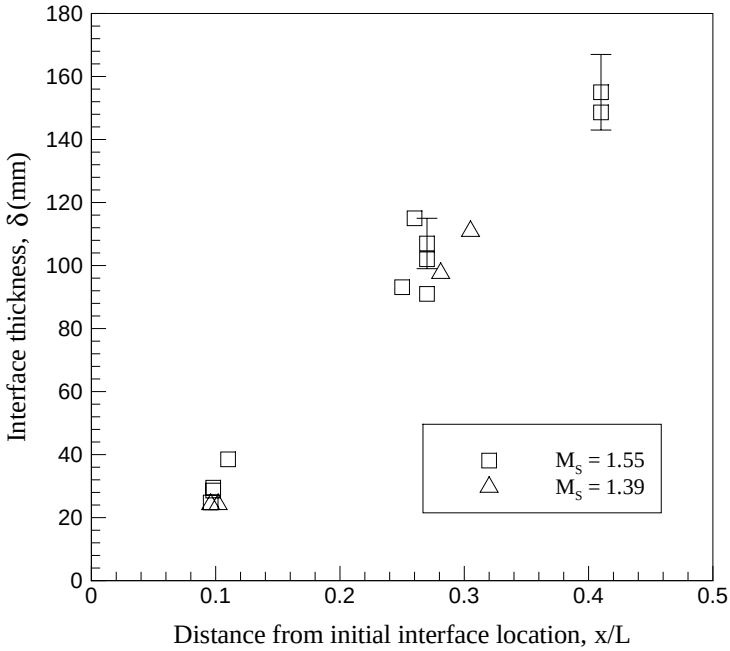

(b)

Figure 4.18: a) Growth rate of TMZ in conical geometry along with Vetter's [74] data with no convergence. b) Interface growth plotted with distance, x/L, $L = 1233.5$ mm is the cone length extrapolating to the apex.

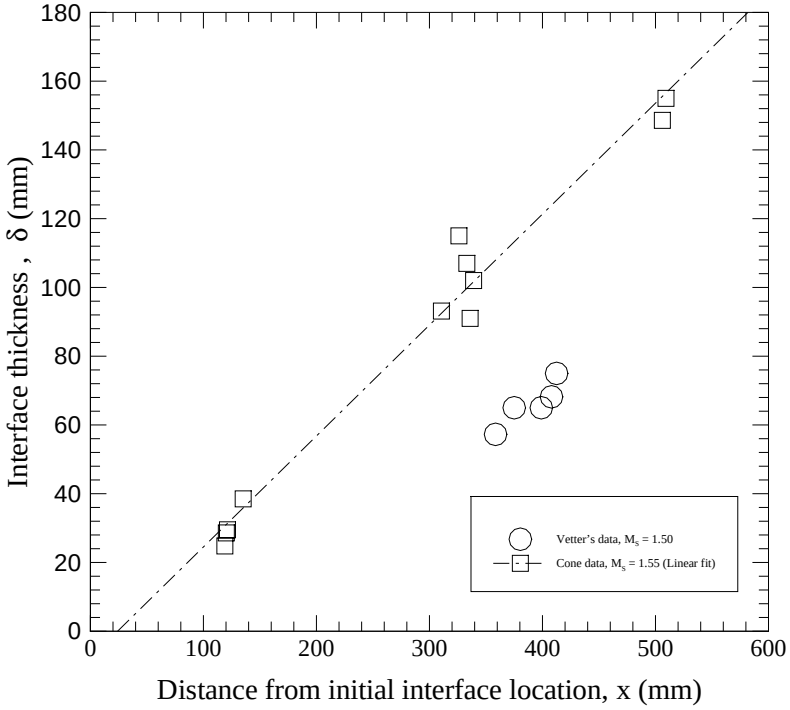

Figure 4.19: TMZ growth vs distance from the initial location in mm. Vetter's data [74] before interaction with reflected shock is also shown.

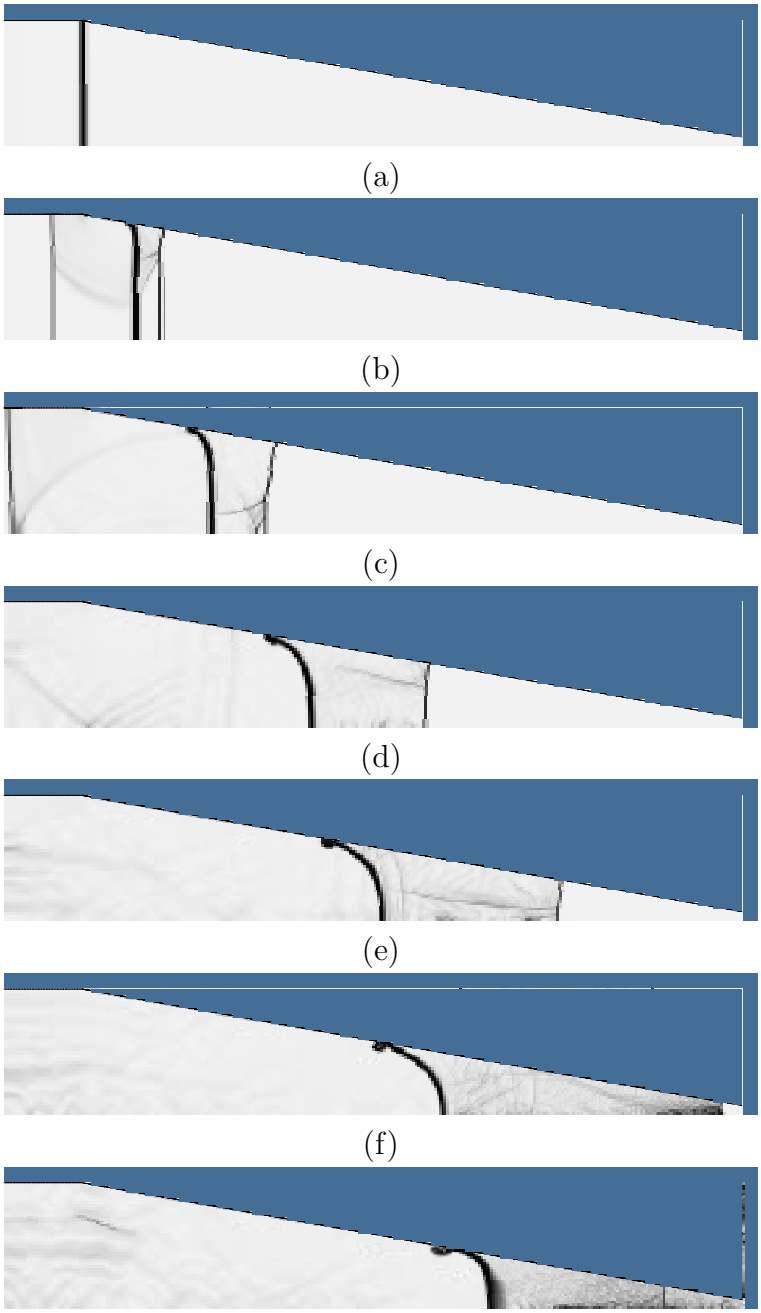

Figure 4.20: Numerical simulation: $M_S = 1.56$, light-heavy (air/SF_6), plane shock and plane interface. (a) $t = 0$ (b) $t = 28.505$ (c) $t = 71.275$ (d) $t = 124.025$ (e) $t = 161.403$ (f) $t = 204.572$ (g) $t = 270.397$. (Case 1)

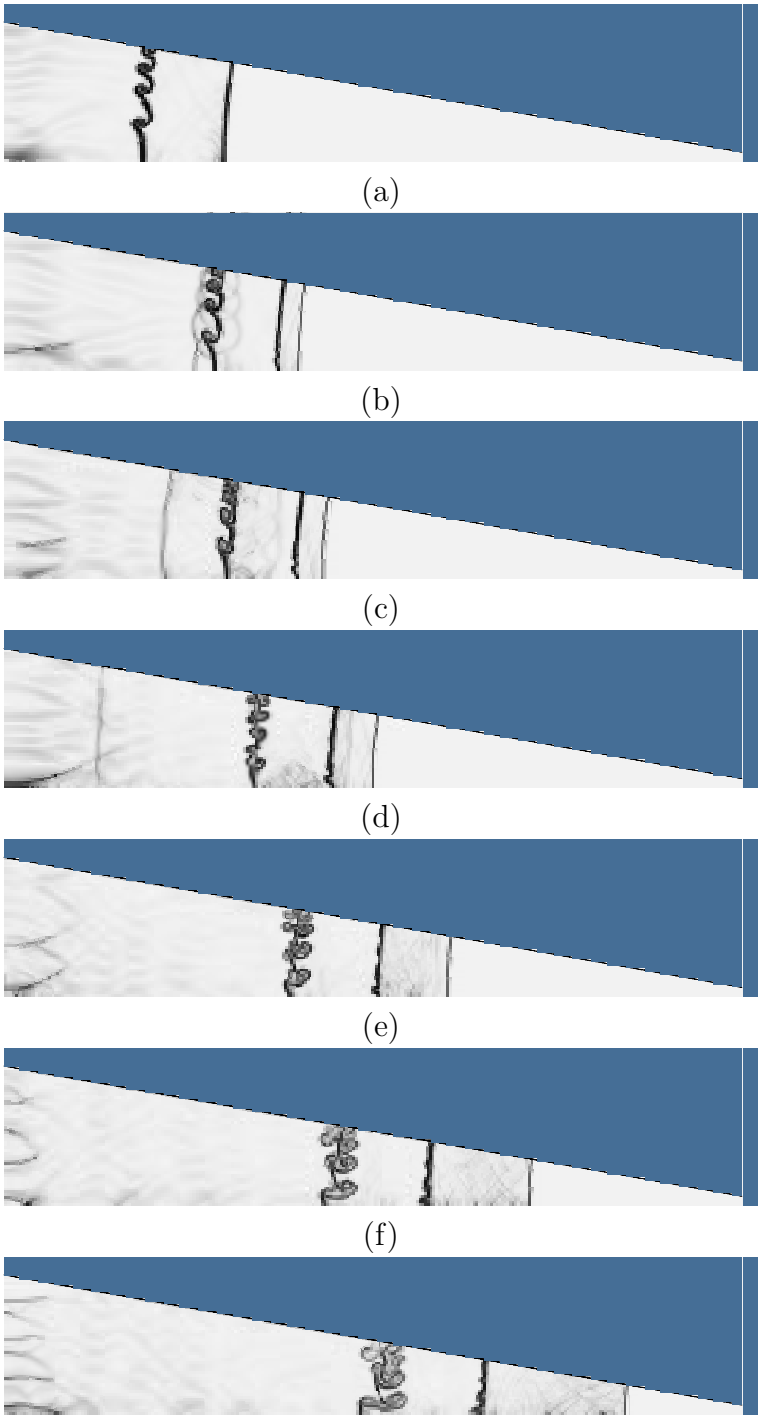

(a)

(b)

(c)

(d)

(e)

(f)

(g)

Figure 4.21: Numerical simulation: $M_S = 1.56$, light-heavy (air/SF_6), spherical shock and spherical interface. (a) $t = 0$ (b) $t = 24.359$ (c) $t = 32.313$ (d) $t = 48.115$ (e) $t = 70.776$ (f) $t = 94.013$ (g) $t = 119.779$. (Case 2)

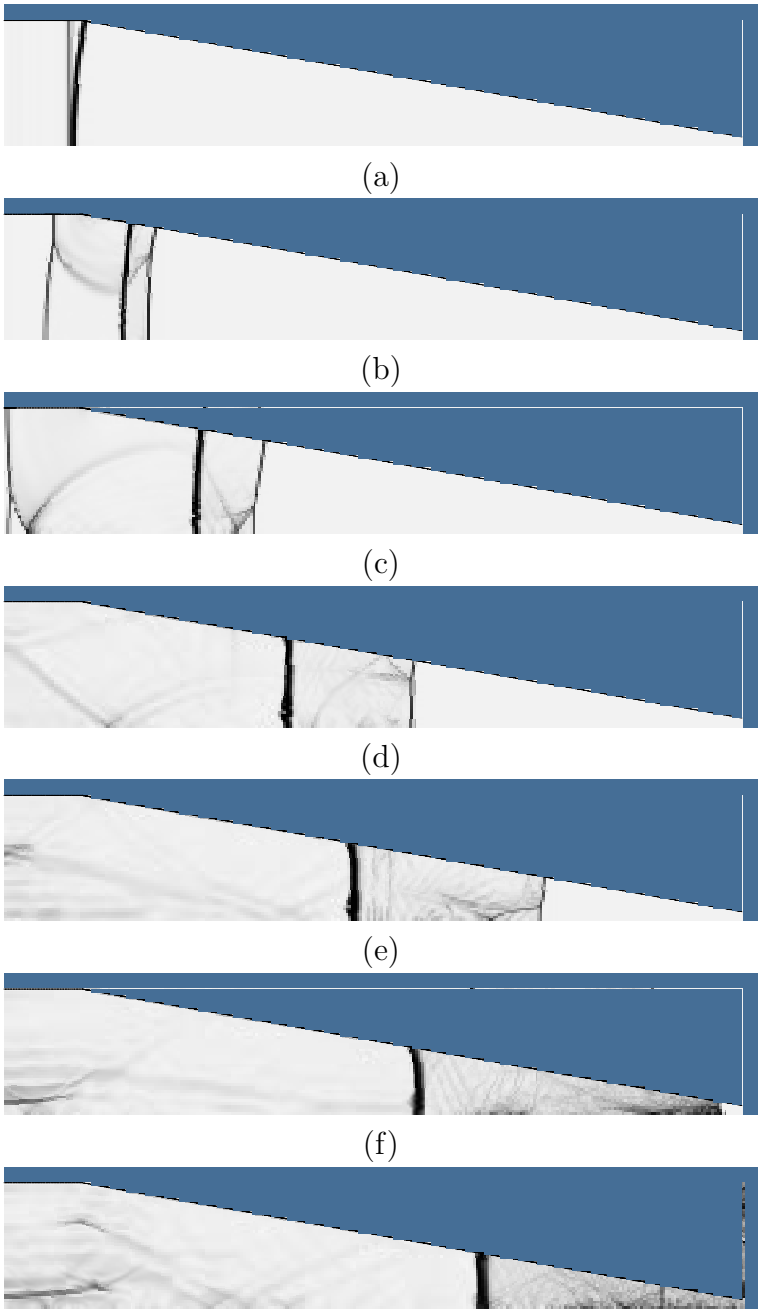

Figure 4.22: Numerical simulation: $M_S = 1.56$, light-heavy (air/SF_6), plane shock and spherical interface. (a) $t = 0$ (b) $t = 28.502$ (c) $t = 68.420$ (d) $t = 120.038$ (e) $t = 160.538$ (f) $t = 205.697$ (g) $t = 272.137$. (Case 3)

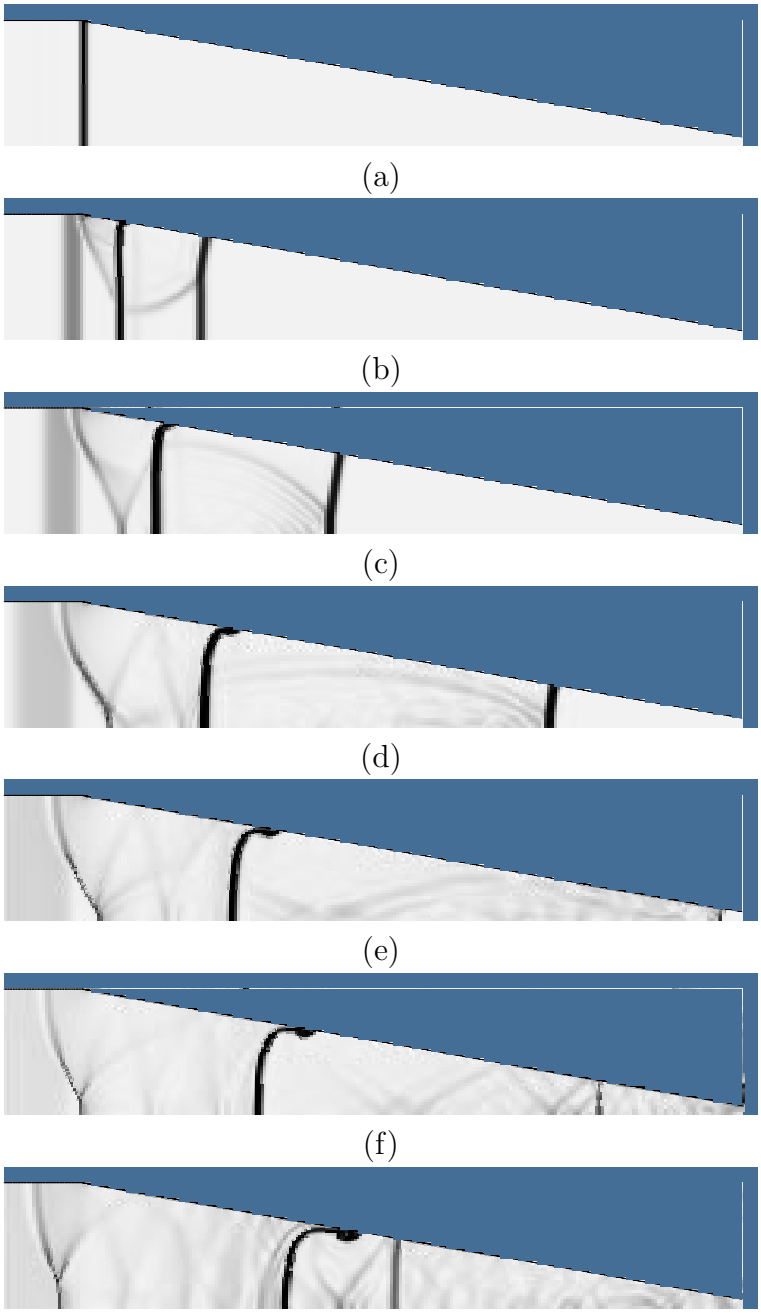

Figure 4.23: Numerical simulation: $M_S = 1.6$, heavy-light (air/Helium), plane shock and plane interface. (a) $t = 0$ (b) $t = 8.173$ (c) $t = 17.105$ (d) $t = 30.116$ (e) $t = 38.16$ (f) $t = 46.191$ (g) $t = 57.363$. (Case 4)

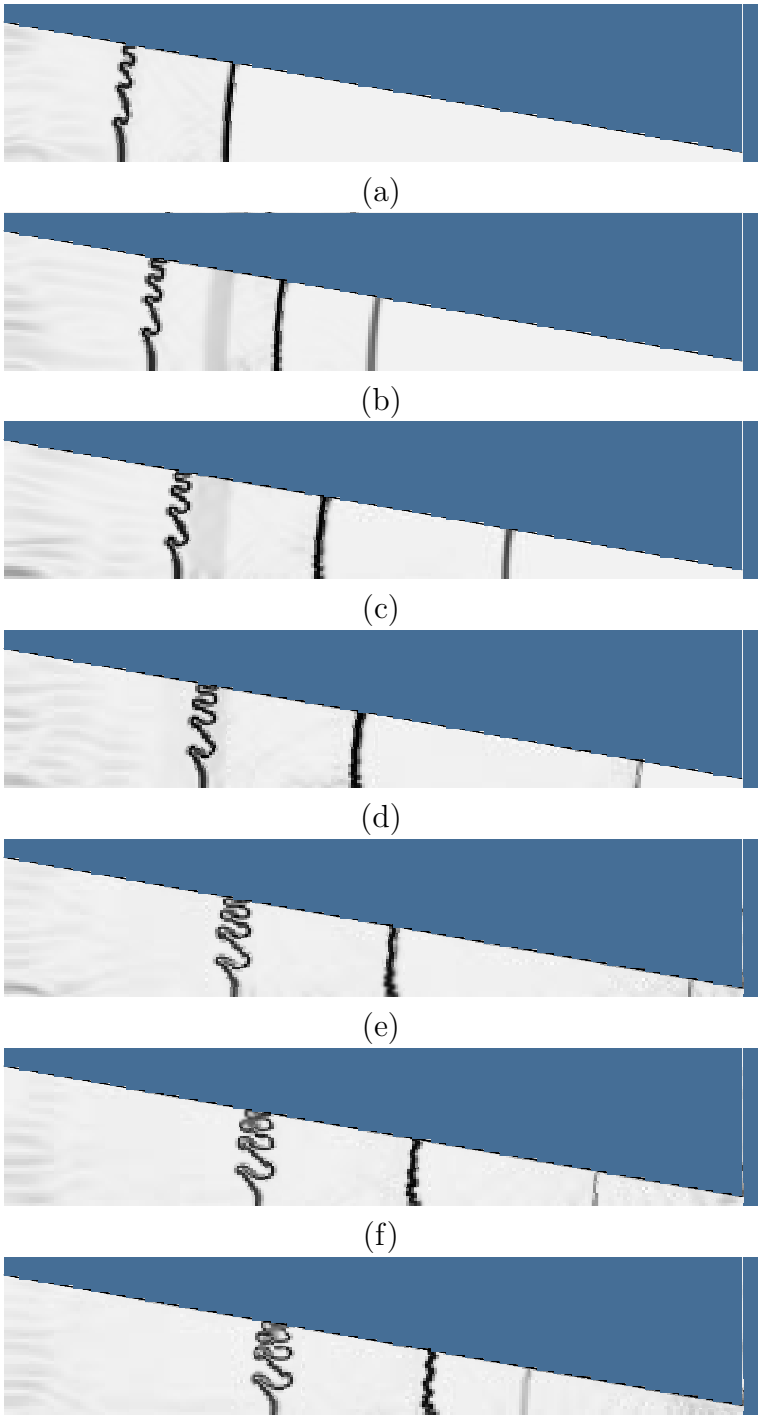

(a)

(b)

(c)

(d)

(e)

(f)

(g)

Figure 4.24: Numerical simulation: $M_S = 1.6$, heavy-light (air/Helium), spherical shock and spherical interface. (a) $t = 0$ (b) $t = 9.279$ (c) $t = 17.237$ (d) $t = 24.126$ (e) $t = 30.934$ (f) $t = 35.732$ (g) $t = 39.428$. (Case 5)

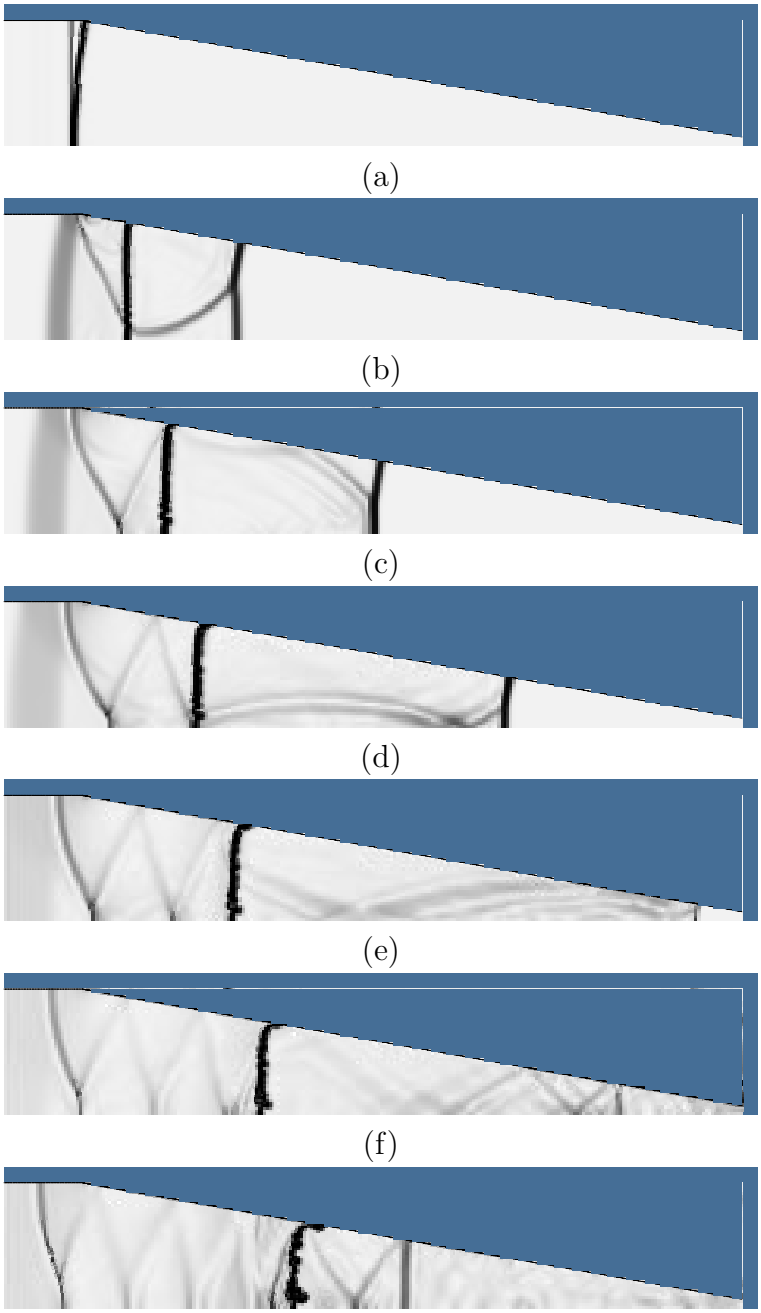

Figure 4.25: Numerical simulation: $M_S = 1.6$, heavy-light (air/Helium), plane shock and spherical interface. (a) $t = 0$ (b) $t = 12.102$ (c) $t = 21.410$ (d) $t = 29.255$ (e) $t = 38.896$ (f) $t = 46.832$ (g) $t = 58.398$. (Case 6)

Chapter 5 Conclusions

The interaction of shock waves with an interface between two gases of different densities has been studied experimentally at late times. The main focus of this study was to understand the growth of TMZ with time in a cylindrical geometry with square cross section and, for the the first time, to study the affect of area convergence in a conical geometry on TMZ growth rate. This research was motivated by the fact that little is known about the late-time development of RM instability. The affect of area convergence on this instability has been simulated by studying this instability in a conical geometry. The experiments were done in GALCIT 17 in. shock tube facility which, due to its relatively large size, minimizes the effects of boundary layers. The initial interface between two gases was formed by a very thin polymeric membrane ($\sim$ 1.5 μm thick) stretched between two wire-mesh frames. The experiments were performed with both single-mode and multimode initial perturbations. In the single-mode perturbation case, the initial perturbation was sinusoidal with two wavelength and amplitude combinations (these were part of four single-mode perturbations studied by Prasad *et al.* [59]). The single-mode initial perturbation growth was studied in a straight test section with a square cross section of 10.5×10.5 in. at late times, when a large range of scales had developed and the mixing zone was fully turbulent. Only the light-heavy configuration, with air as light and SF_6 as heavy gas, was studied for this investigation at one Mach number of 1.55. Data were obtained for interface thickness, δ, at times considerably larger than previously reported in the literature and tested for self-similarity, including independence of initial conditions. It is found that the growth rate decreases rapidly with time, and a small dependence on initial wavelength persists to large times.

The multimode initial perturbation growth at late times was studied in a conical geometry. The test section was a cone of 10 degree half-angle. The interface, on its

way into the cone, interacts with the reflected shock from the triple point resulting from the Mach reflection at the wall. The most important and obvious property of the TMZ, its thickness, is measured at three axial locations in the light-heavy configuration (air/SF_6) at Mach number of 1.55 from schlieren visualization pictures. A few experiments are also done at Mach number of 1.39. The interface moves into the cone and comes to a stop at an axial location that depends on the Mach number. The interface, in all cases, was diagnosed before the interface rapidly decelerated to a stop and the main reflected shock from the cone end hit the interface. It was found from the pictures, that the rear of the interface was very diffuse, so image processing of the picture, based on plotting the average gray-scale value of each pixel column, gave a criterion for thickness determination in situations when it was not clear. The schlieren picture of the air/air interface shows that the membrane fragments tend to cluster together in front of the interface and then they appear as dark spots. They appear as relatively bright spots when not clustered together. The clustering of the fragments on the front of the interface is also visible in laser-induced scattering images. Lots of mixing blobs were visible in the schlieren pictures. Fourier transform of a part of the image gave an idea of the dominant eddy/blob size. In the present experiments, it was about 4 mm, which was about half the spacing between the wires forming the initial interface. The size of these dominant eddies did not seem to vary at various locations in the picture or at a different window location. Planar laser-induced scattering (PLIS) experiments, using olive oil fog as seeding in the test section, were also performed in the heavy-light configuration (air/He) near Mach number of 1.55. It was thought that the physics of the mixing process depended on the absolute magnitude of Atwood number, at least before the arrival of the main reflected shock. The absolute value of the Atwood numbers of air/SF_6 and air/He differ only slightly (see Table 2.3). As expected, the membrane fragments were a source of noise as they appeared as bright scattering spots. The very fine oil droplets visible in the mixing zone gave an idea of the mixing zone thickness. The PLIS image also showed that the rear boundary of the mixing zone is diffuse. Comparison with Vetter's [74] experiments, with no area convergence at about the same Mach number,

showed that the interface thickness was about 40 to 50% greater. This result is based on "visual thickness" determination from schlieren pictures. The mean growth rate at $M_S = 1.55$ was observed to be 45 m/s.

Finally, some computational studies on AMRITA, at the same Mach numbers as in the experiments, revealed the global geometry change of the interface. The interface bends into the cone in the light-heavy configuration and out of the cone in heavy-light case. This is due to the vorticity that is deposited during the initial interaction of the interface with the reflected shock from the triple point. The reversal of the geometry change is due to the reversal in the density gradient vector. This also had the effect of making a spherical interface become planar when hit by a plane shock in the light-heavy configuration. Computational study on sinusoidally perturbed initial interface in both the conical and straight geometries, under the same conditions, revealed that the contribution of reflected transverse waves to vortex dominated growth was negligible. This computational study also suggested that the global curving of the interface could have a role in the diffusive nature of the rear end of the interface, and hence, might affect the TMZ thickness measurements from schlieren pictures. But, as is evident from the laser-induced scattering results in Figure 4.15 (b), the interface in the middle of the test section does not have a well-defined rear boundary either. Rather, small blobs of fluids on the right are scattered in the TMZ. This formation of blobs of fluid, which is governed by complex fluid-dynamical phenomenon (such as development of secondary instabilities, among others), is not captured by the computational results.

5.1 Scope for future work

The present research of studying RM instability in a conical geometry is just the beginning of a very complicated problem involving the area convergence affect on RM instability. In addition to the work presented in this thesis, there are several important aspects of the problem which need to be addressed. More ranges of Atwood numbers and Mach numbers need to be investigated. Planar laser-induced

fluorescence (PLIF) technique will give the detailed structure of the TMZ with the noise from the membrane fragments being eliminated. Also, it will be nice to see the complete TMZ in order to look at the global bending of the interface, as is seen in the numerical computations. PLIF flow visualization would answer most decisively the question of the precise contribution of global curving to interface thickness determination from the schlieren technique. The next step in this research should be to introduce well-defined sinusoidal perturbations at the cone inlet. This will give the growth rate information for each mode separately, thereby giving information about the affect of initial amplitude and wavelength at late times with area convergence. An experimental technique of introducing a spherically imploding shock of appropriate radius at the cone inlet would be very useful, as it would help in avoiding Mach reflection from the cone walls. The evolution of the turbulence spectra in TMZ, at various axial locations along the cone centerline, and within the TMZ, can give information about the degree of isotropy of the turbulence in TMZ.

Bibliography

[1] Abakumov, A.I., Fadeev, V.Yu, Kholkin, S.I., Meshkov, E.E., Nikiforov, V.V., et al. Studies of film effects on the turbulent mixing zone evolution in shock tube experiments. In *Proc. Intl. Work. Compressible Turbl. Mix., 5th, pp. 118-123*, 1996. Singapore: World Scientific.

[2] Afanas'ev, Yu.F., Bosov, N.G., Gamalii, E.G., Krokhin, O.N. and Rozanov, V.B. Two dimensional simulation of fluid instability in laser fusion pellets. *JETP Lett.*, 23:566, 1976.

[3] Aleshin, A.N., Gamalii, E.G., Zaitsev, S.G., Lazareva, E.V., Lebo, I.G. and Rozanov, V.B. Nonlinear and transitional stages in the onset of the Richtmyer-Meshkov instability. *Sov. Tech. Phys. Lett.*, 14:466, 1988.

[4] Alon, U., Hecht, J., Mukamel, D., and Shvarts, D. Scale invariant mixing rates of hydrodynamically unstable interfaces. *Phys. Rev. Lett.*, 72:2867, 1994.

[5] Alon, U., Hecht, J., Ofer, D., and Shvarts, D. Power laws and similarity of Rayleigh-Taylor and Richtmyer-Meshkov mixing fronts at all density ratios. *Phys. Rev. Lett.*, 74:534, 1995.

[6] Andronov, V.A., Bakhrakh, S.M., Meshkov, E.E., Mokhov, V.N. , Nikiforov, V.V., Pevnitskii, A.V. and Tolshmyakov A.I. Turbulent mixing at contact surfaces accelerated by shock wave. *Sov. Phys, JETP*, 44:424, 1976.

[7] Arnett, D. The role of mixing in astrophysics. *Astrophysical J. Suppl. Ser.*, 127(2):213, 2000.

[8] Barenblatt, G.I. *Self similar turbulence propagation from an instantaneous point source.* In Nonlinear Dynamics and Turbulence, Pitman, Boston, 1983. edited by G.I. Barenblatt, G. Iooss and D.D. Joseph.

[9] Batchelor, G.K. *An introduction to fluid dynamics*. Cambridge University Press, 1967. pp. 515-516.

[10] Bell G.I. Taylor instability on cylinders and spheres in the small amplitude approximation. Technical Report LA-1321, Los Alamos National Laboratory, 1951.

[11] Bellman, R. and Pennington, R.H. Effects of surface tension and viscosity on Taylor instability. *Quart. Appl. Math.*, 12:151, 1954.

[12] Bender, C.M. and Orszag, S.A. *Advanced mathematical methods for scientists and engineers*. McGraw-Hill, New York, 1978.

[13] Benjamin, R.F. *Experimental observation of shock stability and shock induced turbulence*. In Advances in compressible turbulent mixing, edited by W.P. Dannevik, A.C Buckingham and C.E. Leith, Conf-8810234, 341-348(Nat. Tech. Inf. Service, Virginia, 1992), 1992.

[14] Benjamin, R.F. and Fritz, J.N. Shock loading a rippled interface between liquids of different densities. *Phys. Fluids*, 30:331, 1987.

[15] Benjamin, R.F., Besnard, D., and Haas, J. Shock and reshock of an unstable interface. LANL report LA-UR 92-1185, 1993.

[16] Benjamin, R.F., Trease, H.E. and Shaner, J.W. Coherent density gradients in water compressed by a modulated shock wave. *Phys. Fluids*, 27:2390, 1984.

[17] Birkhoff, G. *Quart. Appl. Math.*, 12:306, 1954.

[18] Birkhoff, G. *Quart. Appl. Math.*, 13:451, 1956.

[19] Brouillette, M. *On the interaction of shock waves with contact surfaces between gases of different densities.* Ph.D. Thesis, California Institute of Technology, 1989.

[20] Brouillette, M. The Richtmyer-Meshkov instability. *Ann. Rev. Fluid Mech.*, 34:445, 2002.

[21] Brouillette, M. and Sturtevant, B. Growth induced by multiple shock waves normally incident on plane gaseous interfaces. *Physica D*, 37:248, 1989.

[22] Brouillette, M. and Sturtevant, B. Experiments on Richtmyer-Meshkov instability: Small-scale perturbations on a plane interface. *Phys. Fluids*, 5:916, 1993.

[23] Brouillette, M. and Sturtevant, B. Experiments on Richtmyer-Meshkov instability: Small-scale perturbations on a continuous interface. *J. Fluid Mech.*, 263:271, 1994.

[24] Canuto, V.M., Goldman, I. Analytical model for large-scale turbulence. *Phys. Rev. Lett.*, 54:430, 1985.

[25] Chandrasekhar, S. *Hydrodynamic and Hydromagnetic stability.* Dover.

[26] Chasiotis, I. and Knauss, W.G. Mechanical properties of thin polysilicone films by means of probe microsopy. In *Proceedings of the Intl. Soc. for Optical Engineering (SPIE) 3512 pp. 66-75, Santa Clara, CA*, 1998.

[27] Duff, R.E., Harlow, F.H., and Hirt, C.W. Effects of diffusion on interface instability between gases. *Phys. Fluids*, 5:417–425, 1962.

[28] Erez, L., Sadot, O., Oron, D., Erez, G., Levin, L.A., et al. Study of membrane effect on turbulent mixing measurements in shock tubes. *Shock Waves*, 10:241, 2000.

[29] Fermi, E. *The Collected Papers of Enrico Fermi, vol.2.* Univ. of Chicago, Press, Chicago edition, 1965.

[30] Fraley, G. Rayleigh-Taylor stability for a normal shock wave-density discontinuity interaction. *Phys. Fluids*, 29:376, 1986.

[31] Haan, S.W. Onset of nonlinear saturation for Rayleigh-Taylor growth in the presence of full spectrum of modes. *Phys. Rev. A*, 39:5812, 1989.

[32] Hornung, H.G. Regular and Mach reflection of shock waves. *Ann. Rev. Fluid Mech.*, 18:33, 1986.

[33] Houas, L. and Chemouni, I. Experimental investigation of the Richtmyer-Meshkov instability in shock tube. *Phys. Fluids*, 8:614, 1996.

[34] Huang, M.J. and Leonard, A. Power-law decay of homogeneous turbulence at low Reynolds numbers. *Phys. Fluids*, 6:3765, 1994.

[35] Jones, M.A. and Jacobs, J.W. A membrane-less experiment for the study of Richtmyer-Meshkov instability of a shock accelerated gas interface. *Phys. Fluids*, 9:3078, 1997.

[36] Khokhlov, A.M., Oran, E.S., Thomas, G.O. Numerical simulation of deflagration to detonation transition: the role of shock flame interactions in turbulent flames. *Combust. Flames*, 117:323, 1999.

[37] Kiang, R.L. Nonlinear theory of inviscid Taylor instability near the cut-off wave number. *Phys. Fluids*, 12:1333, 1969.

[38] Landau, L.D. and Lifshitz, E.M. *Fluid Mechanics*. Butterworth Heineman, second edition, reprint 1998. p. 486.

[39] Lelevier, R., Lasher, G.J. and Bjorklund, F. Effect of a density gradient on Taylor instability. Technical Report UCRL-4459, University of California Radiation Laboratory, 1955.

[40] Lewis, D.J. The instability of liquid surfaces when accelerated in a direction perpendicular to their planes. II. *Proc. Roy. Soc. A*, 202:81, 1950.

[41] Liepmann, H.W., Roshko, A., Coles, D. and Sturtevant, B. A 17 in. diameter shock tube for studies in rarefied gas dynamics. *Rev. Sci. Instrum.*, 33:625, 1962.

[42] Lindl, J.D. *Inertial Confinement Fusion*. AIP Press, 1998. Springer-Verlag New York Inc.

[43] Lindl, J.D. and Mead, W.C. Two dimensional simulation of fluid instability in laser fusion pellets. *Phys. Rev. Lett.*, 34:1273, 1975.

[44] Lindl, J.D., McCorry, R.L. and Campbell, E.M. Progress towards inertial confinement fusion. *Physics Today*, 45:32, 1992.

[45] Marble, F.E., Hendricks, G.J. and Zukoski, E.E. Progress towards shock enhancement of supersonic combustion process. *AIAA paper*, (87-1880), 1987.

[46] Markstein, G.H. Flow disturbances induced near a slightly wavy contact surface, or flame front, traversed by a shock wave. *J. Aero. Sci.*, 24:238, 1957.

[47] Meshkov, E.E. Instability of the interface of two gases accelerated by a shock wave. *Sov. Fluid Dyn.*, 4:101, 1969.

[48] Meyer, K.A. and Blewett, P.J. Numerical investigation of the stability of a shock accelerated interface between two fluids. *Phys. Fluids*, 15:753, 1972.

[49] Mikaelian, K.O. Turbulent mixing generated by Rayleigh-Taylor and Richtmyer-Meshkov instabilities. *Physica D*, 12:45, 1984.

[50] Mikaelian, K.O. Richtmyer-Meshkov instabilities in stratified fluids. *Phys. Rev. A*, 31(1):410, 1985.

[51] Mikaelian, K.O. Approximate treatment of density gradients in Rayleigh-Taylor instabilities. *Phys. Rev. A*, 33(2):1216, 1986.

[52] Mikaelian, K.O. Explicit growth rates for the Rayleigh-Taylor instability in exponential density profiles. *Phys. Rev. A*, 40:4801, 1989.

[53] Mikaelian, K.O. Rayleigh-Taylor and Richtmyer-Meshkov instabilities and mixing in stratified spherical shells. *Phys. Rev. A*, 42:3400, 1990.

[54] Mikaelian, K.O. Rayleigh-Taylor instabilities in stratified fluids. *Phys. Rev. A*, 26(4):2140, 1990.

[55] Mikaelian, K.O. Turbulent energy at accelerating and shocked interfaces. *Phys. of Fluids A*, 2(4):592, 1990.

[56] Pham, T., and Meiron, D.I. A numerical study of Richtmyer-Meshkov instability in continuously stratified fluids. *Phys. Fluids*, 5:344, 1993.

[57] Plesset, M.S. On the stability of fluid flows with spherical symmetry. *J. Appl. Phys.*, 25:96, 1954.

[58] Plesset, M.S. and Mitchell, T.P. *Quart. Appl. Math.*, 13:419, 1956.

[59] Prasad J.K., Rasheed A., Kumar S. and Sturtevant B. The late time development of Richtmyer-Meshkov instability. *Phys. Fluids*, 12(8):2108, 2000.

[60] Quirk, J.J. AMRITA - a computational facility (for cfd modelling). In *VKI 29th CFD Lecture Series.*, 1998. ISSN 0377-8312.

[61] Read, K.I. Experimental investigation of turbulent mixing in Rayleigh-Taylor instability. *Physica D*, 12:45, 1984.

[62] Richtmyer, R.D. Taylor instability in shock acceleration of compressible fluids. *Commun. on Pure and Appl. Math.*, 8:297, 1960.

[63] Sadot, O., Erez, L., Alon, D., Oron, L., Levin, L.A., Erez, G., Ben-Dor, G. and Shvarts, D. Study of nonlinear evolution of single-mode and two bubble interaction under Richtmyer-Meshkov instability. *Phys. Rev. Lett.*, 80:1654, 1998.

[64] Saffman, P.G. The large-scale structure of homogeneous turbulence. *J. Fluid Mech.*, 27:381, 1967.

[65] Saffman, P.G., Meiron, D.I. Kinetic energy generated by the incompressible Richtmyer-Meshkov instability in a continuously stratified fluid. *Phys. of Fluids*, 1(11):1767, 1989.

[66] Setchell, R.E., Storm, E. and Sturtevant, B. An investigation of shock strengthening in a conical convergent channel. *J. Fluid Mech.*, 56:505, 1972.

[67] Sharp, D.H. An overview of Rayleigh-Taylor instability. *Physica D*, 12:3, 1984.

[68] Smarr, L., Wilson, J.R., Barton, R.T. and Bowers, R.L. Rayleigh-Taylor overturn in supernova core collapse. *Astrophys. J.*, 246:515, 1975.

[69] Strutt, J.W. (Lord Rayleigh). *Scientific Papers, 2.* New York: Dover. PP. 200-207.

[70] Sturtevant, B. Rayleigh-Taylor instability in compressible fluids. *In Shock Tubes and Waves, edited by H. Gronig, VCH, Wendheim, Federal Republic of Germany*, page 89, 1988.

[71] Sunhara, A., Takeuchi, H., Takabe, H. and Mima, K. Shock wave driven instability at material interface in laser driven implosion. *Jpn. J. Appl. Phys.*, 35(10):5501, 1996.

[72] Taylor, G.I. The instability of liquid surfaces when accelerated in a direction perpendicular to their planes, II. *Proc. Royal Soc. Lond.*, A(201):192, 1950.

[73] Vandenboomgaerde, M., Mugler, C. and Gauthier, S. Impulsive model for the Richtmyer-Meshkov instability. *Phys. Rev. E*, 58:1874, 1998.

[74] Vetter, M. and Sturtevant, B. Experiments on the Richtmyer-Meshkov instability of an air/SF6 interface. *Shock Waves*, 4:247, 1995.

[75] Waitz, I.A., Marble, F.E., and Zukoski, E.E. An investigation of a contoured wall injector for hypervelocity mixing augmentation. *AIAA paper*, (91-2265), 1991.

[76] Wouchuck, J.G. and Nishihara, K. Linear perturbation growth at a shocked interface. *Phys. Plasmas*, 3:3761, 1996.

[77] Yang, V., Kubota, T. and Zukoski, E.E. Applications of shock induced mixing to supersonic combustion. *AIAA Journal*, 31:854, 1993.

[78] Youngs, D.L. Numerical simulation of turbulent mixing by Rayleigh-Taylor instability. *Physica D*, 12:32, 1984.

[79] Zaytsev, S.G., Lazareva, E.V., Chernuka, V.V. and Belyaev, V.M. Experiments on the Richtmyer-Meshkov instability of an air/SF6 interface. *Sov. Phys. Dokl.*, 30:579, 1985.

[80] Zhang, Q. and Sohn, S. Nonlinear theory of unstable fluid mixing driven by shock waves. *Phys. Fluids*, 9:1106, 1997.

Appendix A Record of all the runs in the shock tube

This appendix gives a record of all the runs performed for this study. In the comments section of these tables, the term "successful run" means that the experiment went well but unfortunately the image capture was not successful. The "unsuccessful run" means that the experiment went well, but the mixing zone was not in the right position to draw any conclusions about its thickness. The term "bad run" means that the experiment did not go well, possibly because the membrane was broken or the electronics did not work. The runs used for analysis are in bold face.

A.1 Table of runs for the straight test section

Run number	**Interface nature**	**Mach number** (± 0.01)	**Comments**
Rshot1	Frame 4	1.28	learning operation (bad run)
Rshot2	Frame 1	1.46	successful run
Rshot3	Frame 1	1.28	bad run
Rshot4	Frame 1	1.27	bad run
Rshot5	Frame 3	1.48	bad run
Rshot6	Frame 3	1.50	bad run
Rshot7	Frame 2	1.46	bad run
Rshot8	-	-	no membrane
Rshot9	Frame 3	-	bad run
Rshot10	Frame 4	1.55	successful run
Rshot12	Frame 1	1.50	bad run
Rshot13	Frame 1	1.49	bad run
Rshot14	Frame 4	1.49	successful run
Rshot15	Frame 4	1.50	bad pressure traces
Rshot16	Frame 4	1.54	succesful run
Rshot17	Frame 1	1.52	bad pressure traces

Run number	**Interface nature**	**Mach number** (± 0.01)	**Comments**
Rshot18	Frame 1	1.52	bad pressure traces
Rshot19	multimode(planar)	1.57	successful run
Rshot20	Frame 1	1.57	successful run
Rshot21	Frame 3	1.57	successful run
Rshot22	Frame 2	1.57	successful run
Rshot23 (SK23)	**Frame 2**	**1.58**	**successful run**
Rshot24 (SK24)	**Frame 3**	**1.57**	**successful run**

A.2 Table of runs for the conical test section

Run number	**Interface nature**	**Mach number** (± 0.01)	**Comments**
Rshot30	multimode	1.50	successful run
Rshot31		1.47	unsuccessful run
Rshot32		1.56	unsuccessful run
Rshot33		1.54	unsuccessful run
Rshot34		**1.56**	**successful run**
Rshot35		**1.55**	**successful run**
Rshot36		1.53	unsuccessful run
Rshot37		1.56	successful run
Rshot38		1.57	successful run
Rshot39		1.56	unsuccessful run
Rshot40		1.55	unsuccessful run
Rshot41		1.57	unsuccessful run
Rshot42		1.57	unsuccessful run
Rshot43		1.56	successful run
Rshot44		1.56	unsuccessful run
Rshot45		1.57	unsuccessful run
Rshot46		1.57	unsuccessful run
Rshot47		1.57	unsuccessful run
Rshot48		1.57	unsuccessful run
Rshot49		1.57	unsuccessful run
Rshot50		1.57	unsuccessful run
Rshot51		1.57	unsuccessful run
Rshot52		1.57	unsuccessful run

Run number	**Interface nature**	**Mach number** (± 0.01)	**Comments**
Rshot53	multimode	1.56	unsuccessful run
Rshot54		1.57	unsuccessful run
Rshot55		1.58	unsuccessful run
Rshot56		1.57	unsuccessful run
Rshot57		1.58	unsuccessful run
Rshot58		1.56	unsuccessful run
Rshot59		1.57	unsuccessful run
Rshot60		1.57	unsuccessful run
Rshot61		**1.58**	**successful run**
Rshot62		1.43	bad run
Rshot63		1.58	unsuccessful run
Rshot64		**1.58**	**successful run**
Rshot65		1.58	unsuccessful run
Rshot66		1.56	successful run
Rshot67		**1.56**	**successful run**
Rshot68		1.56	successful run
Rshot69		1.57	unsuccessful run
Rshot70		**1.58**	**successful run**
Rshot71		1.39	unsuccessful run
Rshot72		1.37	unsuccessful run
Rshot73		1.33	unsuccessful run
Rshot74		1.37	unsuccessful run
Rshot75		1.39	successful run
Rshot76		1.41	successful run
Rshot77		1.39	successful run
Rshot78		1.39	unsuccessful run
Rshot79		1.34	unsuccessful run
Rshot80		1.39	unsuccessful run
Rshot81		**1.57**	**successful run**
Rshot82		**1.56**	**successful run**
Rshot83		**1.58**	**successful run**
Rshot84		1.60	bad run
Rshot85		**1.56**	**successful run**
Rshot86		1.33	unsuccessful run
Rshot87		1.37	unsuccessful run
Rshot88		**1.40**	**successful run**

Run number	**Interface nature**	**Mach number** (± 0.01)	**Comments**
Rshot89	multimode	**1.39**	**successful run**
Rshot90		1.33	successful run
Rshot91		1.38	unsuccessful run
Rshot92		1.37	unsuccessful run
Rshot93		1.38	successful run
Rshot94		1.39	successful run
Rshot95		**1.55**	**successful run**
Rshot96		1.56	successful run
Rshot97		**1.57**	**successful run**
Rshot98		**1.39**	**successful run**
Rshot99		**1.39**	**successful run**
Rshot100		1.40	unsuccessful run
Rshot101		1.56	unsuccessful run
Rshot102		1.39	unsuccessful run
Rshot103		1.35	unsuccessful run
Rshot104		1.38	unsuccessful run
Rshot105		1.57	successful run
Rshot106		1.59	successful run
Rshot107		1.61	successful run
Rshot108		1.58	successful run
			Laser sheet:
Rshot109		1.20	unsuccessful run
			He/N_2
Rshot110		1.23	unsuccessful run
Rshot111		1.57	unsuccessful run
			air/He
Rshot112		1.58	unsuccessful run
Rshot113		1.53	unsuccessful run
Rshot114	-	-	bad run
Rshot115		1.60	unsuccessful run
Rshot116		1.60	unsuccessful run
Rshot117		1.60	unsuccessful run
Rshot118		1.59	unsuccessful run
Rshot119		1.60	successful run
Rshot120		1.59	successful run
Rshot121		1.60	successful run

Run number	**Interface nature**	**Mach number** (± 0.01)	**Comments**
Rshot122	multimode	1.59	successful run
Rshot123		1.59	successful run
Rshot124		1.60	bad run
Rshot125		1.60	unsuccessful run
Rshot126		1.59	successful run
Rshot127		1.58	successful run
Rshot128		1.60	unsuccessful run
Rshot129		**1.60**	**successful run**
			Schlieren runs:
Rshot135		1.56	unsuccessful run
Rshot136		1.55	unsuccessful run
Rshot137		1.58	unsuccessful run
Rshot138		1.59	unsuccessful run
Rshot139		1.69	bad run
Rshot140		1.57	unsuccessful run
Rshot141		1.57	unsuccessful run
Rshot142		1.59	unsuccessful run
Rshot143		1.58	successful run
Rshot144		1.56	successful run
Rshot145		1.56	successful run
Rshot146		1.57	successful run
			air/air
Rshot147		1.59	successful run
Rshot148		**1.59**	**successful run**
Rshot149		1.56	successful run
			air/Helium
Rshot150		**1.60**	**successful run**
Rshot151		1.59	successful run

A.3 TMZ thickness determination in second window location at $M_S = 1.55$

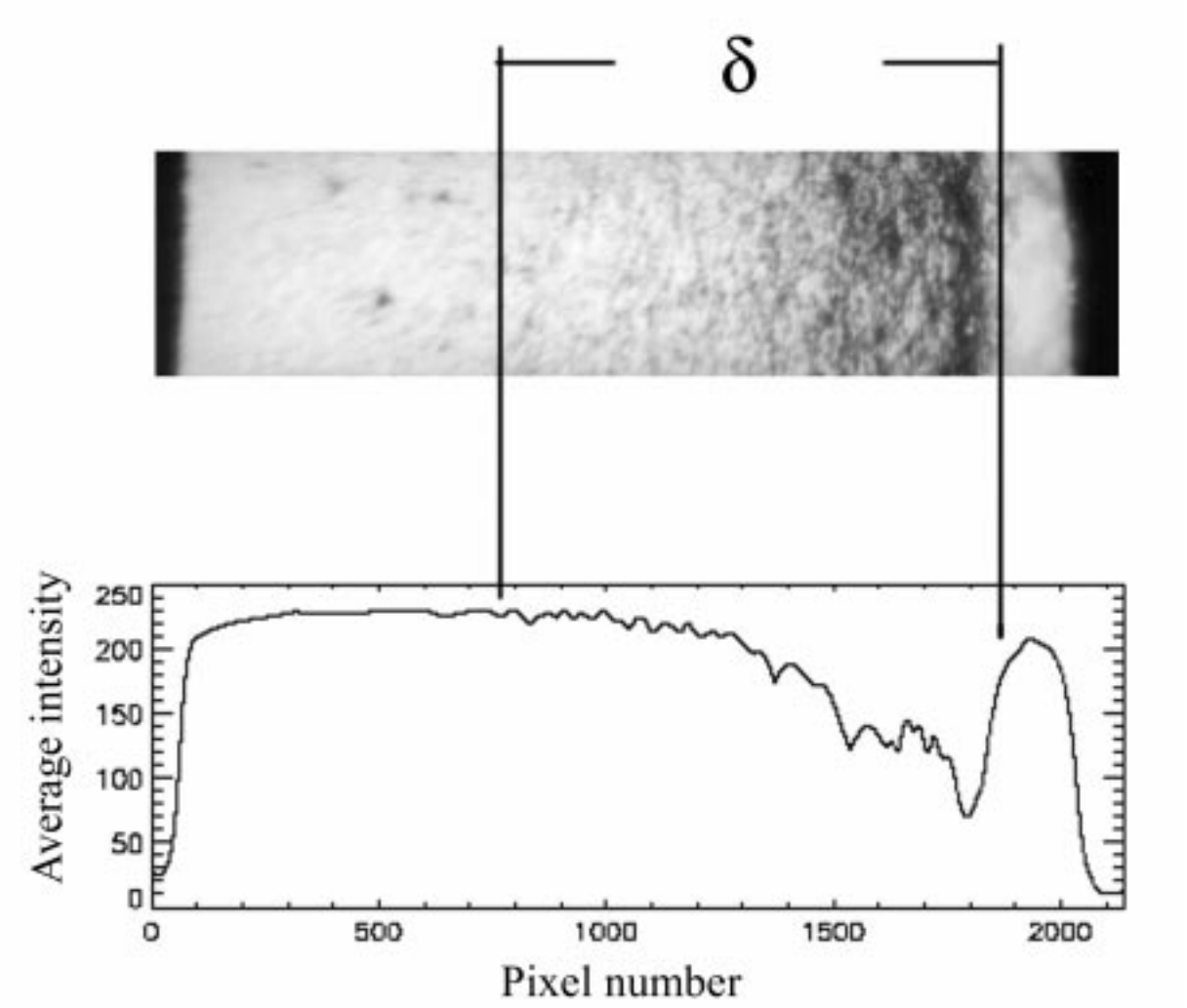

Rshot81 ($M_S = 1.57$, $\delta = 93.76$ mm)

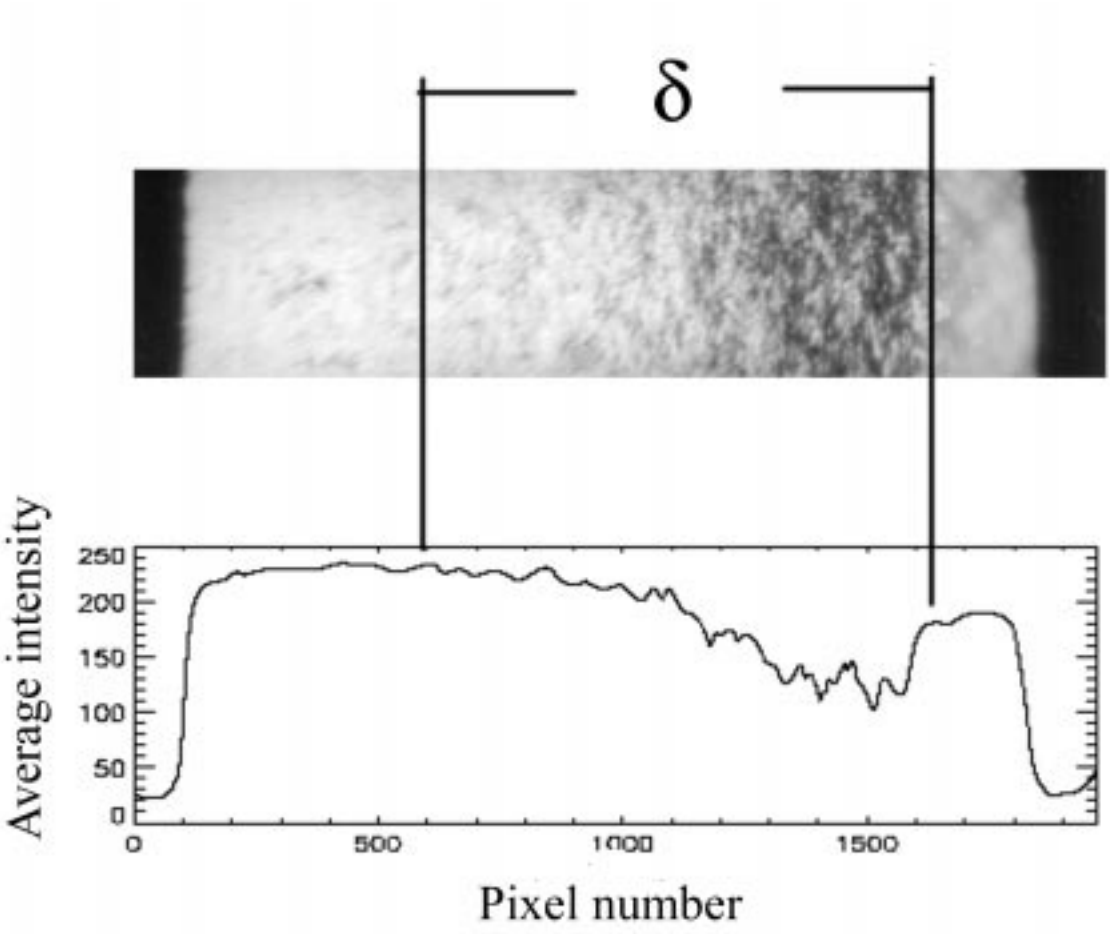

Rshot82 ($M_S = 1.56,\ \delta = 107$ mm)

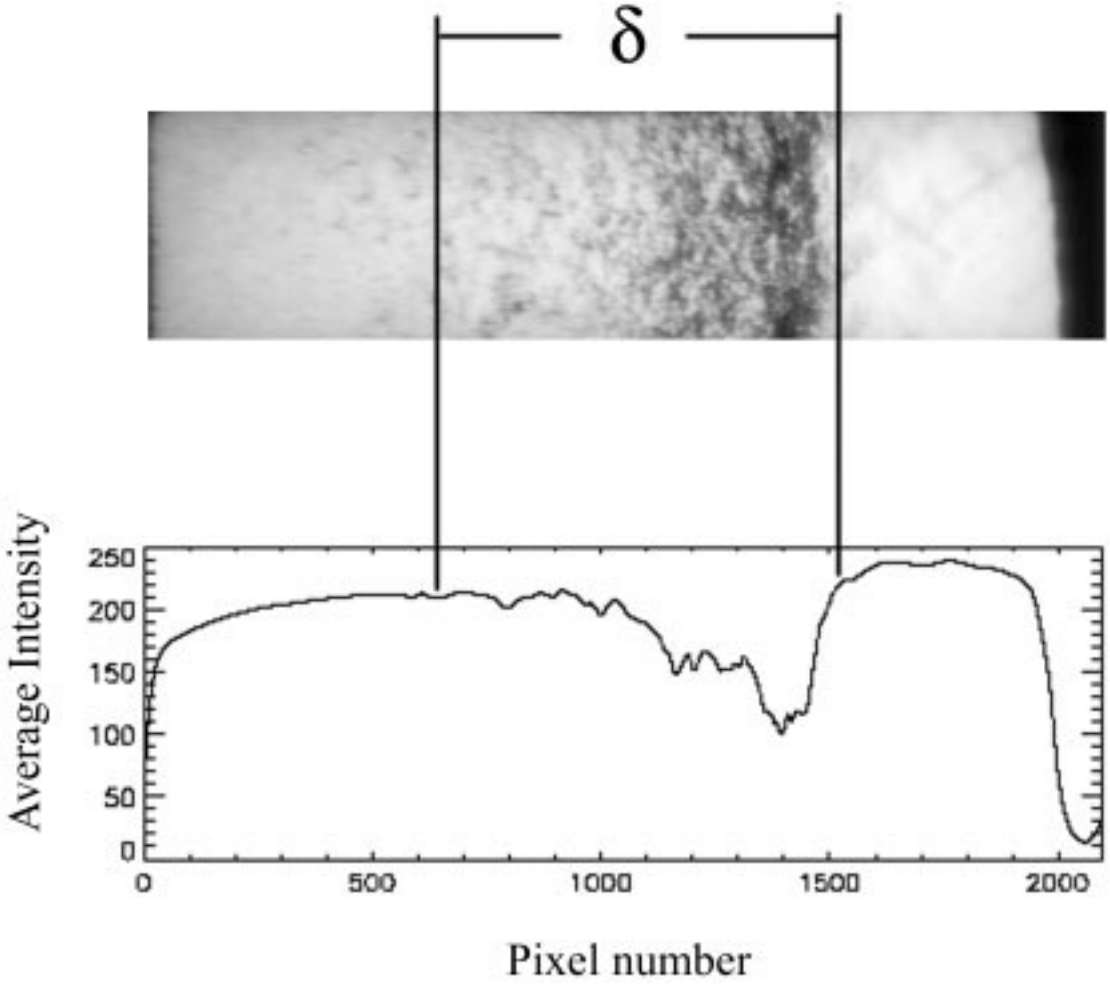

Rshot95 ($M_S = 1.55,\ \delta = 77.6$ mm)

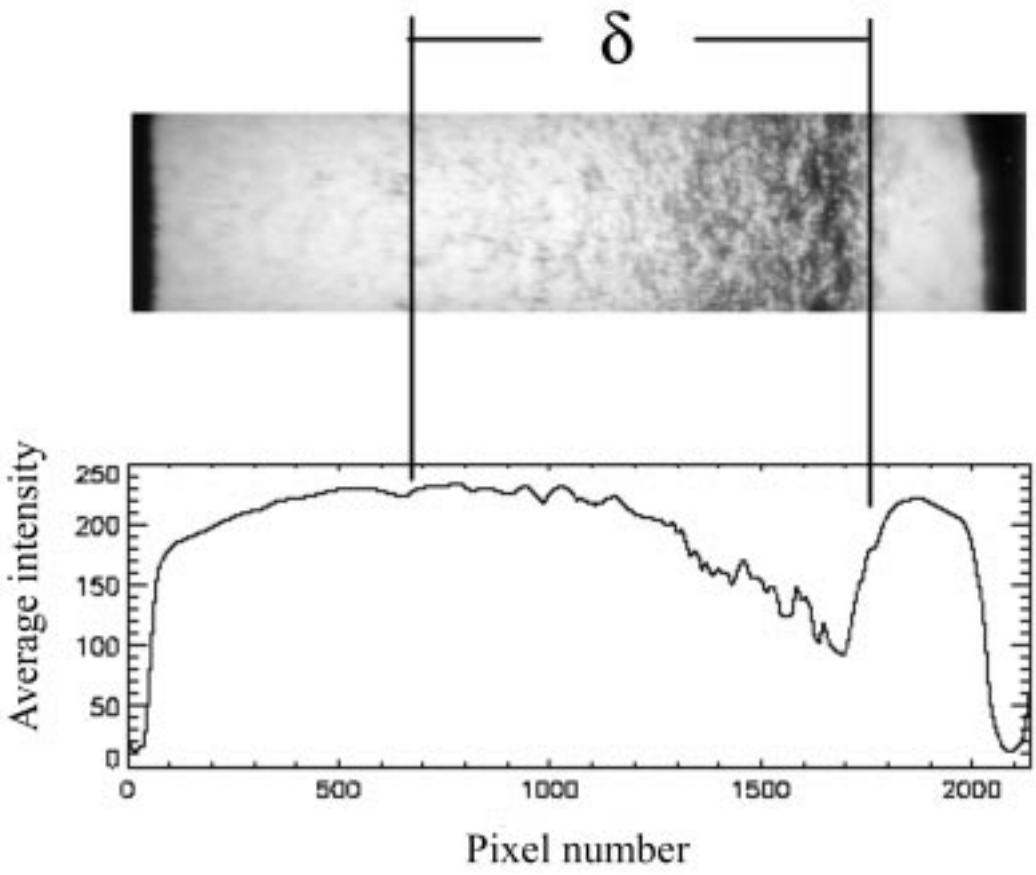

Rshot97 ($M_S = 1.57,\ \delta = 100.1$ mm)

A.4 Details of the runs used from the experiments in the conical test section

Run number	**Mach number** (± 0.01)	**x-location (mm)**	**Time (ms)**	**TMZ thickness (mm)**
Rshot34	1.56	119	0.949	24.8
Rshot35	1.55	29.5	0.949	29.5
Rshot61	1.57	506.1	3.682	148.6
Rshot64	1.57	509.3	3.781	155
Rshot67	1.56	336	2.42	91
Rshot81	1.57	339.1	2.44	102
Rshot82	1.56	333.1	2.418	107
Rshot83	1.58	135.2	1.042	38.5
Rshot85	1.56	120.3	0.949	28.6
Rshot88	1.40	118.1	1.19	24.2
Rshot89	1.39	125.8	1.25	24.2
Rshot95	1.55	310.6	2.42	93.13
Rshot97	1.57	326.1	2.44	115
Rshot98	1.39	347	3.84	97.56
Rshpt99	1.39	376.7	4.12	110.9